

INFORMATION TO USERS

This manuscript has been reproduced from the microfilm master. UMI films the text directly from the original or copy submitted. Thus, some thesis and dissertation copies are in typewriter face, while others may be from any type of computer printer.

The quality of this reproduction is dependent upon the quality of the copy submitted. Broken or indistinct print, colored or poor quality illustrations and photographs, print bleedthrough, substandard margins, and improper alignment can adversely affect reproduction.

In the unlikely event that the author did not send UMI a complete manuscript and there are missing pages, these will be noted. Also, if unauthorized copyright material had to be removed, a note will indicate the deletion.

Oversize materials (e.g., maps, drawings, charts) are reproduced by sectioning the original, beginning at the upper left-hand corner and continuing from left to right in equal sections with small overlaps. Each original is also photographed in one exposure and is included in reduced form at the back of the book.

Photographs included in the original manuscript have been reproduced xerographically in this copy. Higher quality 6" x 9" black and white photographic prints are available for any photographs or illustrations appearing in this copy for an additional charge. Contact UMI directly to order.

UMI

A Bell & Howell Information Company
300 North Zeeb Road, Ann Arbor MI 48106-1346 USA
313/761-4700 800/521-0600

The Application of Wavelet Transform-based Heart Rate
Variability Analysis to the Prediction of Nonsustained
Ventricular Tachycardia

DISSERTATION

Presented in Partial Fulfillment of the Requirements for
the Degree Doctor of Philosophy in the
Graduate School of The Ohio State University

By

Szi-Wen Chen, B.S.E.E., M.S.E.E.

* * * * *

The Ohio State University

1997

Dissertation Committee:

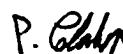
Peter M. Clarkson, Adviser

Robert L. Hamlin

Jogikal M. Jagadeesh

Steven D. Nelson

Approved by



Adviser

Biomedical Engineering
Center

UMI Number: 9801664

UMI Microform 9801664
Copyright 1997, by UMI Company. All rights reserved.

**This microform edition is protected against unauthorized
copying under Title 17, United States Code.**

UMI
300 North Zeeb Road
Ann Arbor, MI 48103

© Copyright by

Szi-Wen Chen

1997

ABSTRACT

Nonsustained ventricular tachycardia (NSVT) is usually asymptomatic, even in patients with cardiac diseases. In fact, the presence of NSVT is usually associated with an increased incidence of subsequent sustained VT and has been considered as a risk factor and a harbinger of *sudden cardiac death* (SCD). The detection of NSVT thus becomes of great concern for clinicians. Previous studies have reported that decreased long-term *heart rate variability* (HRV) may be associated with a propensity to ventricular tachyarrhythmias. It is still disputed, however, whether there is any alteration/derangement in instantaneous HRV or *autonomic balance status* (ABS) immediately before the onset of these arrhythmias. If so, we can then effectively mark and predict the occurrence of NSVT. The aim of this study is to investigate this important clinical subject. Knowing that the ABS (or sympathovagal balance status) can be quantified by *heart rate* (HR) via the *low frequency* (LF) to *high frequency* (HF) spectral power ratio, we investigated the relationship between *autonomic nervous system* (ANS) and NSVT by assessing short-term ABS prior to the onset of NSVT. A novel *wavelet transform* (WT) based scheme for HRV assessment is introduced to facilitate the analysis. Due to its characteristic of varying frequency resolutions, the WT can optimize the use of time-frequency information so that the instantaneous ABS may be measured over a very short time frame (8-second period) far more accurately than via the traditional *short-time Fourier transform* (STFT) based analysis

which employs a fixed frequency resolution. A morphological information marker α is then employed to characterize the behavior of the ABS waveform. This marker is defined as the ratio of the mean value of the entries in an ABS vector greater than a pre-determined threshold to that of the entries in the ABS vector less than the threshold. In general, a large α may imply a trend of more peaks, or unusual large peaks relative to the entire ABS waveform. Experiments were conducted using a database consisting of 87 NSVT, 61 ischemic and 5 normal episodes. Analysis of this data produced distributions for α as for NSVT, ischemic and normal episodes that overlapped, but had significantly different means. Optimally setting the threshold for α produced correct classification results as follows: 68/87 \approx 78% NSVT, 45/61 \approx 74% ischemia and 4/5=80% normal. Numerical results obtained from the WT-based scheme indicated that while there were no significant differences in the ABS waveforms observed for ischemic and normal episodes (both with smaller α), the ABS evolution underwent an abrupt increase over a period several minutes (8–20 minutes) preceding the onset of NSVT (with larger α), suggesting that a significantly accelerated short-term sympathovagal imbalance might predict the occurrence of NSVT.

To God

ACKNOWLEDGMENTS

At first I would like to express my deepest gratitude to my adviser, professor Peter M. Clarkson, for his thoughtful guidance and help in everything during my doctoral career. Our relationship started when I was in a miserable and difficult situation in 1993–1994. It gave me very much pleasure to work with him. I also sincerely appreciate professors Robert L. Hamlin and Jogikal M. Jagadeesh for their serving on my candidacy and dissertation committees. Special thanks go to professor Ashok K. Krishnamurthy for his encouragement and help to me in my study career and also, for his serving on my candidacy committee. In particular, I would like to thank Dr. Steven D. Nelson for providing the patient data and heart rate recordings requested by this research and many constructive discussions.

I would like to thank my family for what they have done for me. Also, I appreciate my girlfriend for her constant patience on me. Because of their endless love, all my efforts become more worthwhile. Feelings in my heart are always more than I can express in words. Finally, I would love to thank and praise God for His lead on me in my life. The whole achievement is dedicated to Him, with all my heart, all my mind and all my strength.

VITA

November 2, 1966 Born—Taipei, Taiwan

June 1989 B.S. Electrical Engineering
National Taiwan University
Taipei, Taiwan

July 1989 – May 1991 Communication Officer: Lieutenant
Taiwanese Army
Taipei, Taiwan

April 1993 – June 1993 Graduate Research Associate
The Ohio State University
Columbus, Ohio, U.S.A.

June 1993 M.S. Electrical Engineering
The Ohio State University
Columbus, Ohio, U.S.A.

April 1994 – present Graduate Research Associate
The Ohio State University
Columbus, Ohio, U.S.A.

PUBLICATIONS

Research Publications

S.-W. Chen, P. M. Clarkson and Q. Fan, "A robust sequential detection algorithm for cardiac arrhythmia classification," *IEEE Transactions on Biomedical Engineering*, vol. 43, no. 11, pp. 1120–1125, November, 1996.

S.-W. Chen and P. M. Clarkson, "Detection of cardiac arrhythmias using a damped exponential modeling algorithm," in *IEEE Proceedings of the 1996 International Conference on Acoustics, Speech, and Signal Processing (ICASSP 96)*, vol. 3, pp. 1776–1779, Atlanta, GA, May 7–10, 1996.

S.-W. Chen and P. M. Clarkson, "Identification of cardiac arrhythmias using a damped exponential predominant frequency algorithm," in *IEEE Proceedings of the 17th Annual International Conference of the Engineering in Medicine and Biology Society (EMBS 95)*, pp. 181–182, Montreal, Canada, September 20–23, 1995.

P. M. Clarkson, S.-W. Chen and Q. Fan, "A robust sequential detection algorithm for cardiac arrhythmia classification," in *IEEE Proceedings of the 1995 International Conference on Acoustics, Speech, and Signal Processing (ICASSP 95)*, vol. 2, pp. 1181–1184, Detroit, MI, May 9–12, 1995.

S.-W. Chen and P. M. Clarkson, "Prony residual analysis for the identification of cardiac arrhythmias," in *IEEE Proceedings of the 1995 International Conference on Acoustics, Speech, and Signal Processing (ICASSP 95)*, vol. 2, pp. 1177–1180, Detroit, MI, May 9–12, 1995.

S.-W. Chen, P. M. Clarkson and Q. Fan, "A sequential technique for cardiac arrhythmia discrimination," in *Proceedings of International Society for Computerized Electrocardiology (ISCE)*, Orlando, FL, April 1995.

B. D. Jaffe, S.-W. Chen, S. D. Nelson and L. C. Potter, "Prony frequency analysis of prolonged QRS signal-averaged electrocardiograms," *Circulation Research*, vol. 41, no. 3, p. 659A, 1993.

S.-W. Chen, B. D. Jaffe, S. D. Nelson and L. C. Potter, "Prony residual as ventricular tachycardia marker," *Circulation*, vol. 88, no. 4, part 2, p. I-644, 1993.

FIELDS OF STUDY

Major Field: Biomedical Engineering

Studies in:

Signal Processing	Prof. Peter M. Clarkson
	Prof. Ashok K. Krishnamurthy
Cardiology	Prof. Robert L. Hamlin

TABLE OF CONTENTS

	Page
Abstract	ii
Dedication	iv
Acknowledgments	v
Vita	vi
List of Tables	xi
List of Figures	xiii
Chapters:	
1. Introduction	1
1.1 Background	4
1.1.1 Regulation of the Heartbeat	4
1.1.2 HRV Analysis	11
1.1.3 The Clinical Significance of Nonsustained Ventricular Tachycardia (NSVT)	16
1.2 Contribution of this Research Work	19
1.3 Overview	19
2. Review of Wavelet Transform-based Techniques	21
2.1 Continuous Wavelet Transform (CWT)	22
2.2 Multiresolution Analysis	24
2.3 Filter Banks and Fast Wavelet Transform	26

3.	Design and Method Validation of WT-based Analysis Schemes for HRV Investigations	36
3.1	Rationale	36
3.2	HR Data Measurement and Preprocessing	38
3.3	Design of WT-based Analysis Schemes	41
3.3.1	Analysis Scheme 1	46
3.3.2	Analysis Scheme 2	51
3.4	Validation Experiments	58
3.4.1	STFT Analysis	58
3.4.2	Method Validation for Analysis Scheme 1	61
3.4.3	Method Validation for Analysis Scheme 2	66
3.5	Frequency Responses of the Dyadic Wavelet Functions	68
4.	The Application of WT-based HRV Analysis to the Prediction of NSVT	77
4.1	A Postulate	77
4.2	Database	78
4.2.1	Data Selection Criteria	79
4.3	Approach	83
4.3.1	Design Motivation	83
4.3.2	Analysis Unit (AU) Based Scheme	84
4.3.3	Morphological Information Indication	96
4.4	Numerical Experimental Results	104
4.4.1	Performance: Distributions of α	104
4.4.2	Performance: Receiver Operating Characteristic	106
5.	Performance Evaluation and Clinical Implications	115
5.1	Underlying Pathophysiological Significance	115
5.1.1	Factors of Sympathetic Predominance in NSVT	115
5.1.2	Relation between Clinical Variables and α in NSVT	123
5.2	An Examination of Long-Term HRV Behavior	129
6.	Conclusion	135
6.1	A Summary of this Research Work	135
6.2	Potential Limitations	137
6.3	An Extension for Future Explorations	140
6.3.1	NSVT Risk Stratification	140
6.3.2	NSVT versus Nonischemic Heart Disease	143

Bibliography 145

LIST OF TABLES

Table	Page
1.1	Definitions for time domain measures of HRV. 15
1.2	A list of the existing tests and their associated risk factors (VT- ventricular tachycardia; CAD- coronary artery disease; VPB- ventricular premature beat; LVEF- left ventricular ejection fraction; LAD- left anterior descending coronary artery; LCX- left circumflex coronary artery; RCA- right coronary artery). 17
3.1	$r_1^{(FWT1)}$ obtained from the eight subjects during tilt and supine. . . 62
3.2	$r_1^{(FFT)}$ obtained from the eight subjects during tilt and supine. . . . 62
3.3	Passbands of the 5 filters in Fig. 3.15. Here, the theoretical and the estimated frequency bands (<i>i.e.</i> , 3 dB cut-off frequency) are both provided. 71
4.1	Numerical power ratio estimates obtained from 5 AU's for the RR signal in Fig. 4.1; here, each row represents the power ratio vector obtained from an AU. 89
4.2	Part of ROC in NSVT versus ischemia: column 1- threshold η ; column 2- percentage of overall accuracy; column 3- percentage of specified ischemia; column 4- percentage of specified NSVT; column 5- number of false NSVT; column 6- number of false ischemia. 113
4.3	Part of ROC in NSVT versus normal: column 1- threshold η ; column 2- percentage of overall accuracy; column 3- percentage of specified normal; column 4- percentage of specified NSVT; column 5- number of false NSVT; column 6- number of false normal. 114

5.1	Demographic data including the gender, age and LVEF for a subset of the NSVT patients in our database; the subset contained 8 patients since only their demographic data were available. Note that all these NSVT patients had CAD.	124
5.2	Distributions of long-term sympathovagal balance r_{sv} for the NSVT, ischemic and normal.	132
5.3	Optimal classification results given by the threshold for long-term LF/HF ranged from 0.387 to 0.414.	133

LIST OF FIGURES

Figure	Page
1.1 A simulant control diagram of the cardiovascular system.	3
1.2 Factors contributed to RSA. Respiration influences a wide range physiological parameters through its mechanical effects and through direct links in the central nervous system.	10
1.3 The RR-interval signal, HR signal and RR power spectrum obtained from a normal individual: (a) RR signal; (b) HR signal; (c) power spectrum of the RR signal as given in (a).	13
2.1 (a) Implementation of FWT using a filter bank structure (analysis decomposition scheme); (b) implementation of IFWT using a filter bank structure (synthesis reconstruction scheme).	30
2.2 Dyadic blocks in frequency domain	34
3.1 HR Measurement and preprocessing procedure.	39
3.2 Illustrations of RR and HR signals: (a) an RR interval tachogram; (b) an HR tachogram; (c) the corresponding resampled RR signal; (d) the corresponding resampled HR signal.	42
3.3 WT-based multiresolution representation of the RR signal for a subject at supine position. Top panel– normalized RR signal; the second to the sixth panels (from the top)– composite detail signals with corresponding scaling levels: 2^{-1} to 2^{-5} (<i>i.e.</i> , in subspaces W_{-1} to W_{-5}), respectively; bottom panel– composite coarse signal at level 2^{-5} (V_{-5}).	44

3.4	WT-based multiresolution representation of the RR signal for a subject at tilt position. Top panel– normalized RR signal; the second to the sixth panels (from the top)– composite detail signals with corresponding scaling levels: 2^{-1} to 2^{-5} (i.e., in subspaces W_{-1} to W_{-5}), respectively; bottom panel– composite coarse signal at level 2^{-5} (V_{-5}).	45
3.5	(a) scaling function $\phi(t)$; (b) wavelet function $\psi(t)$. Both are estimated by Daubechies wavelet system filters $h(n)$ and $g(n)$ with 8 filter coefficients (successive approximation).	46
3.6	Time-frequency tiles and coverage of the time-frequency plane for wavelet analysis (thick-line blocks represent windowed regions that occupy the same real time interval T ; also, each thin-line block has the same number of WT coefficients).	47
3.7	Time-frequency tiles and coverage of the time-frequency plane for wavelet analysis (thick-line blocks represent the windowed regions that have the same number of WT coefficients).	51
3.8	An illustration for the demonstrative example in Section 3.3.2. Note that each tile (or window) contains M WT coefficients ($M = 4$); power calculation is then performed on each one of these windows. In addition, the enumerative numbers (in italic style) for the windows at the levels of interest ($j = -2, -3, -5$) are also included. To describe the window movement, a sequential representation of (i, l, m) is thus expressed as: $(1, 1, 1) \rightarrow (1, 1, 2) \rightarrow (1, 2, 3) \rightarrow (1, 2, 4) \rightarrow (1, 3, 5) \rightarrow (1, 3, 6) \rightarrow (1, 4, 7) \rightarrow (1, 4, 8)$.	54
3.9	The instantaneous autonomic balance states during supine (dash line) and tilt (solid line) maneuvers obtained by the proposed WT-based scheme 2.	56
3.10	The instantaneous autonomic balance states during supine (dash line) and tilt (solid line) maneuvers obtained by the traditional STFT method.	57
3.11	Short-time autonomic balance states during supine/tilt positions obtained by FWT analysis for all eight subjects (dash line: supine; solid line: tilt).	64

3.12	Short-time autonomic balance states during supine/tilt positions obtained by FFT analysis for all eight subjects (dash line: supine; solid line: tilt).	65
3.13	The WT-based autonomic balance state estimates (from analysis scheme 2) during supine (dash line) and tilt (solid line) maneuvers for all the eight subjects (#1-#8) in the database for method validation.	69
3.14	The traditional STFT-based autonomic balance state estimates during supine (dash line) and tilt (solid line) maneuvers for all the eight subjects (#1-#8) in the database for method validation.	70
3.15	Realization of the filtering structure involved in WT computation. $x(t)$ represents the input signal to be analyzed and $d_{-1}(t), \dots, d_{-5}(t)$ represent the output signals of the 5 filters $w_{-1}(t), \dots, w_{-5}(t)$, respectively. Note that the output signals $d_{-1}(t), \dots, d_{-5}(t)$ can be equivalently visualized as the detail signals at level $2^{-1}, \dots, 2^{-5}$, respectively, in WT computation.	72
3.16	Frequency responses of the Daubechies wavelet system filters with 8 coefficients: (a) scaling filter $h(k)$; (b) wavelet filter $g(k)$	73
3.17	Plots of the impulse responses (left column) and their corresponding frequency responses (right column) for all the 5 filters in Fig. 3.15. Note that for each plot in right column, dash line represents the theoretical frequency response (<i>i.e.</i> , a ideal bandpass filter) and solid line represent the actual frequency response of the filter $w_j(t)$	74
3.18	Frequency responses of the smooth bandpass filters employed in this research. Here, we adopted the dyadic bands $j = -2, -3$ as HF and $j = -5$ as LF.	76
4.1	A typical observation of RR-interval (or NN-interval) signals for an NSVT episode selected to be analyzed. Note that here the time located at 0 minute represents the onset of NSVT.	80
4.2	A typical observation of RR-interval (or NN-interval) signals for an ischemic episode selected to be analyzed.	81
4.3	A typical observation of RR-interval (or NN-interval) signals for a normal episode selected to be analyzed.	82

4.4	The structural plot of an <i>analysis unit</i> (AU). It can be seen that varying real-time intervals occupied by the tiles at different levels. Note that here an AU contains 8 windows at the lowest level (level 2^{-5}). Each tile (or window) contains 4 WT coefficients. In addition, the enumerative numbers (in italic style) for the windows at the levels of interest ($j = -2, -3, -5$) are used to describe the window movement, expressed as: $(1, 1, 1) \rightarrow (1, 1, 2) \rightarrow (1, 2, 3) \rightarrow \dots \rightarrow (8, 31, 61) \rightarrow (8, 31, 62) \rightarrow (8, 32, 63) \rightarrow (8, 32, 64)$	85
4.5	The schematic diagram for the AU-based approach. In this diagram, it includes illustrations of both the shift-and-computation and ABS padding processes.	88
4.6	The ABS evolutions $([\mathbf{r}_1^{(q)T} \ \mathbf{r}_2^{(q)T} \ \dots \ \mathbf{r}_8^{(q)T}]^T$, for $q = 1, 2, 3, 4, 5$) obtained from all the AU's extracted from an RR signal prior to the occurrence of NSVT (the abscissa represents the time before the onset of NSVT).	91
4.7	Seven equivalent paths (from (a) to (g)) to achieve the estimate of \mathbf{r}_{evol} . Note that in each chart, a row represents the power ratio vector corresponding to an AU.	92
4.8	The resultant instantaneous ABS evolution for the entire RR signal obtained from Fig. 4.6 (an NSVT episode).	93
4.9	The instantaneous ABS evolution obtained from an ischemic episode.	94
4.10	The instantaneous ABS evolution obtained from a normal episode.	95
4.11	Morphological information obtained from the ABS waveform of an NSVT episode: left panel- ABS waveform with the threshold $\delta \cdot \max(\mathbf{r}_{evol})$; right panel- modeled probability density functions resulted from the probability distributions of both groups separated by the threshold; note that dash lines indicate their mean locations.	98
4.12	Morphological information obtained from the ABS waveform of an ischemic episode: left panel- ABS waveform with the threshold $\delta \cdot \max(\mathbf{r}_{evol})$; right panel- modeled probability density functions resulted from the probability distributions of both groups separated by the threshold; note that dash lines indicate their mean locations.	99

4.13	Morphological information obtained from the ABS waveform of a normal episode: left panel– ABS waveform with the threshold $\delta\text{-max}(\mathbf{r}_{evol})$; right panel– modeled probability density functions resulted from the probability distributions of both groups separated by the threshold; note that dash lines indicate their mean locations.	100
4.14	Examples of ABS evolutions for NSVT episodes: (a) $\alpha = 21.7873$; (b) $\alpha = 16.4842$; (c) $\alpha = 8.0943$	101
4.15	Examples of ABS evolutions for ischemic episodes: (a) $\alpha = 3.4921$; (b) $\alpha = 4.4373$; (c) $\alpha = 5.1239$	102
4.16	Examples of ABS evolutions for normal episodes: (a) $\alpha = 5.2610$; (b) $\alpha = 5.9559$; (c) $\alpha = 5.0755$	103
4.17	Distributions of α obtained from NSVT, ischemic and normal episodes; note that the bars are mean values \pm standard deviations.	110
4.18	Plots of ROC curve for NSVT versus ischemia (upper left panel), percentage of specified NSVT $100 \cdot P_{c1}$ versus threshold η (upper right panel), and percentage of specified ischemia $100 \cdot P_{c2}$ versus threshold η (lower left panel); note that the operating point $100 \cdot (P_{c2}, P_{c1})$ in this ROC curve is (74%, 78%) and the corresponding threshold value is $\eta = 6.31$	111
4.19	Plots of ROC curve for NSVT versus normal (upper left panel), percentage of specified NSVT $100 \cdot P_{c1}$ versus threshold η (upper right panel), and percentage of specified normal $100 \cdot P_{c2}$ versus threshold η (lower left panel); note that the operating point $100 \cdot (P_{c2}, P_{c1})$ in this ROC curve is (80%, 78%) and the corresponding threshold value is $\eta = 6.31$	112
5.1	The ROC curve of LF-based (<i>i.e.</i> , increased-sympathetic based) classification formed by the percentage of identified NSVT versus that of identified non-NSVT (ischemic and normal). Here, the optimal operating point in this ROC curve is (non-NSVT, NSVT) = (62%, 63%).	121

5.2	The ROC curve of HF-based (<i>i.e.</i> , decreased-parasympathetic based) classification formed by the percentage of identified NSVT versus that of identified non-NSVT (ischemic and normal). Here, the optimal operating point in this ROC curve is (non-NSVT,NSVT) = (62%, 61%).	122
5.3	A linear regression analysis was performed on the morphological information marker α versus the LVEF for the NSVT patients; the regression line with a negative slope was also included in the scatter plot. Note that the correlation coefficient between the two variables in this application was $\rho \approx -0.66$.	127
5.4	An illustration of the potential mechanism between left ventricular dysfunction and occurrence of the NSVT.	130
6.1	The application of long-term HRV assessment for prediction of the propensity to NSVT. Note that th_l represents a pre-determined threshold for long-term sympathovagal balance status.	138
6.2	The application of the short-term HRV assessment for prediction of the exact occurrence of NSVT. Note that th_s represents a pre-determined threshold for morphological information marker α derived from short-term sympathovagal balance evolution.	139
6.3	The limitation of EPS-guided therapy as the sole strategy for managing the inducible SMVT (high risk) patients. According to the results suggested by Wilber <i>et al.</i> , treatment for prevention of SCD is unnecessary in patients without inducible SMVT, whereas only approximate 50% of the inducible SMVT patients were drug responders and nonresponders remained at high risk for subsequent SCD.	142

CHAPTER 1

INTRODUCTION

Nonsustained ventricular tachycardia (NSVT), defined as three or more consecutive *ventricular premature beats* (VPBs) with a rate of more than 120 beats/minute and lasting less than 30 seconds [36, 88], is usually asymptomatic, even in patients with cardiac diseases [11]. It can occur in normal individuals as well as in a variety of cardiac and non-cardiac disease states. Among the risk factors for *sudden cardiac death* (SCD), NSVT is the most challenging and difficult to manage because there has been no evidence to suggest a “cause-and-effect” relationship between NSVT and cardiac death although *ventricular tachycardia* (VT) is implicated in most cases of SCD [46]. It has been confirmed, however, that the presence of NSVT is associated with an increased incidence of subsequent sustained VT [62] and is thus considered as a harbinger of SCD [14, 15, 16, 17, 18, 19, 20, 54]. Therefore, the detection of NSVT becomes of great concern for clinicians.

Due to a lack of knowledge regarding the need for, as well as the potential benefits of antiarrhythmic therapy, there have been a number of investigations based on the use of *electrophysiological* (EPS) testing in stratifying risk and directing therapy in patients with NSVT [11, 62, 102, 104, 106]. While EPS testing appears to provide a promising basis for risk stratification and assignment of therapy in patients with

chronic *coronary artery disease* (CAD) and NSVT [11, 62, 106], such testing is highly invasive, expensive, limited to large medical facilities with specialized personnel [15], and limited to effective treatment strategy for patients with inducible VT [81]. Also, this programmed electrical stimulation does not appear to be useful in NSVT patients with *nonischemic heart diseases* (NHD) [81, 88, 102]. Therefore, a noninvasive, low-cost prognostic alternative for risk stratification of NSVT would represent a significant benefit.

During the last decade, more and more effort has been invested in understanding the fluctuations in cardiovascular parameters. The rationale of this growing interest in the study of cardiovascular variability is based on the hope that this approach may serve as an unprecedented tools to explore neural regulatory mechanisms as shown in Fig. 1.1. For this purpose, the instantaneous *heart rate* (HR) has been selected by researchers as the main cardiovascular candidate for analysis of fluctuations because it is the most straightforward keyhole into cardiovascular control [3, 9, 74], and is the most easily measured. *Heart rate variability* (HRV) analysis thus has substantial potential in both physiological studies and clinical investigations since it deals with beat-to-beat fluctuations in the parameters of ECG waveforms due to the influence of the autonomic function. In general, the regulatory components taken into consideration in HRV are sympathetic- and parasympathetic-mediated activities. Since the *autonomic nervous system* (ANS) plays an important role in the genesis of lethal arrhythmias [22], we here propose a research study conducted on assessing HRV for patients with NSVT. We may speculate that instead of EPS testing experiments, such a noninvasive analysis may provide useful information about: (1) the relationship between ANS and NSVT, and (2) how ANS influences NSVT.

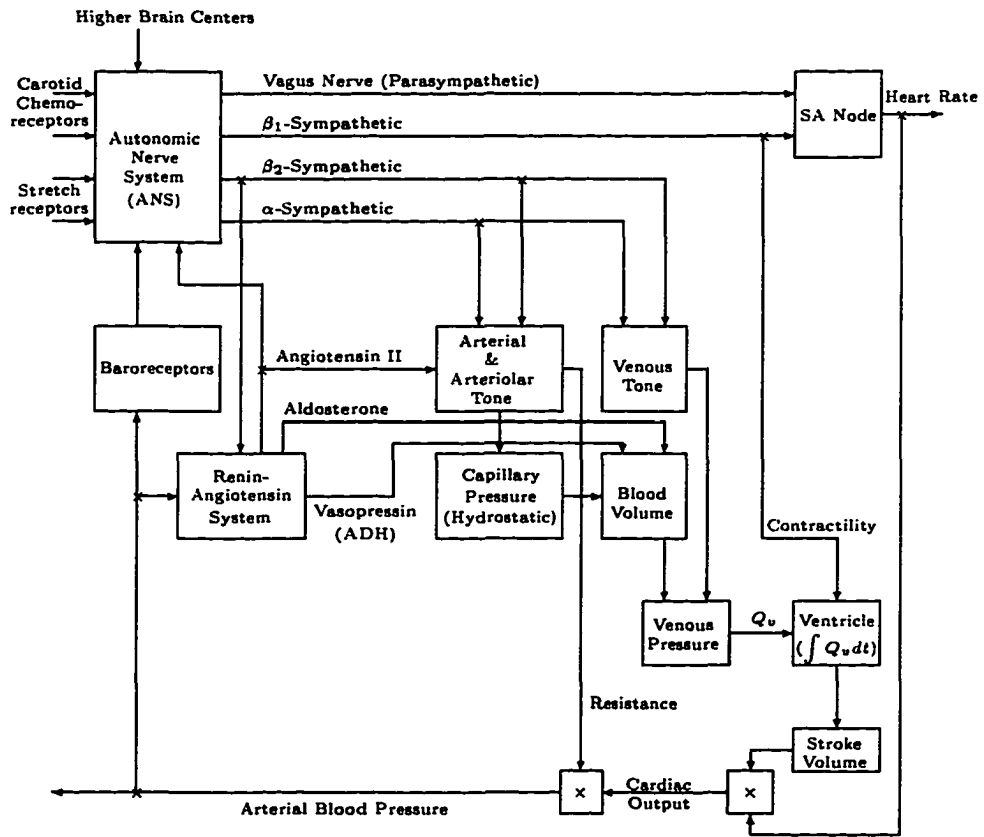


Figure 1.1: A simulant control diagram of the cardiovascular system.

In this research, a novel multiresolution analysis based on *wavelet transform* (WT) is *first* introduced for HRV measurement. Such a technique may provide an accurate time-frequency representation of the HR pattern/behavior so that even short-term autonomic activity can be accurately localized and measured. Assessment of HRV is then performed simply by evaluating the dynamic features defined as the power ratio of *low frequency* (LF) to *high frequency* (HF) components (*i.e.*, $r(t) = \text{LF}(t)/\text{HF}(t)$), known to represent the evolution of the ANS balance state and/or ANS influence, where the LF and HF powers are both derived from WT coefficients. The ultimate goal of this research is to improve the sensitivity and specificity of HRV as a predictor of NSVT and SCD, towards risk stratification as well as mortality prediction for cardiac patients with NSVT.

1.1 Background

In this section, we provide a brief review of heartbeat regulation, HRV analysis and of the clinical importance of NSVT.

1.1.1 Regulation of the Heartbeat

Heart rate (HR) is normally determined by the rate of depolarization of the cardiac pacemaker. In fact, pacemaker tissue is located in the *sinoatrial* (SA) node, the *atrioventricular* (AV) node and the Purkinje fibers. Since the depolarization rate of the SA node is faster than that of other pacemaker tissue and the action potential spreads via the cardiac conducting pathways to other pacemakers before they spontaneously depolarize, the SA node normally determines the HR. In case the SA node fails to generate an impulse, a pacemaker elsewhere usually takes over. Certain local factors, such as temperature changes and tissue stretch, may influence the discharge

frequency of the SA node. However, the principal control of HR is attributed to the ANS. The discussion in this section will be restricted to the nervous control of HR.

The SA node is usually under the tonic influence of both divisions of the ANS. The sympathetic system enhances automaticity, whereas the parasympathetic system inhibits it. The HR represents the net effect of the parasympathetic nerves which reduce it and the sympathetic nerves which increase it. Generally, in healthy and resting individuals parasympathetic tone dominates [10]. When both divisions of ANS are blocked, the HR (referred to as intrinsic HR) of young adults averages about 100 *beats per minute* (BPM).

Parasympathetic Effects

The parasympathetic nerves originate in the medulla oblongata, in cells that lie in the dorsal motor nucleus of vagus or in the nucleus ambiguus [10]. They run down the neck alongside the carotid arteries into the thorax to synapse with postganglionic cells located on the epicardial surface or within the walls of the heart itself. Most of the cardiac ganglion cells are located near the SA node and AV conduction tissue. The parasympathetic postganglionic fibers innervate the SA node, the AV conducting pathways, and the atrial muscles. The question of whether or not the vagi provide an efferent control of ventricular muscle remains controversial. Actually, the most obvious effect of vagal stimulation is to slow, or even stop, the heart. Stimulation of vagal nerves slows the heart or reduces HR. In addition to its effects on SA node, vagal activity also slows AV conduction.

Note that both the SA and AV nodes are rich in cholinesterase. Hence, the effects of a given vagal impulse are ephemeral since the acetylcholine released at the nerve terminals is rapidly hydrolyzed. Also, since the effects of vagal activity on SA and

AV nodal function have a very short latency (\approx 50–100 milliseconds), vagal stimulation results in a peak response either in the first or the second beat after its onset. After termination of vagal stimulation, HR rapidly returns to its previous level. The combination of the brief latency and the rapid decay of the response (because acetylcholine is rapidly hydrolyzed) provides the potential for the vagal nerves to exert a beat-to-beat control of SA and AV nodal function.

Sympathetic Effects

The sympathetic nerves originate in the intermediolateral column of the spinal cord in the upper thoracic region. White rami synapse in the sympathetic ganglia and the grey rami run with the preganglionic vagal fibers over the mediastinum. Both the postganglionic cardiac sympathetic and parasympathetic fibers then form a complex plexus of mixed efferent nerves to the heart. The sympathetic postganglionic fibers approach the base of the heart along the adventitial surface of the great vessels. On reaching the base of the heart, these fibers are distributed to the various chambers as an extensive epicardial plexus. They then penetrate the myocardium. The adrenergic receptors in the nodal regions and in the myocardium are predominantly of the β type, *i.e.*, they are responsive to β -adrenergic agonists (*e.g.*, isoproterenol) and inhibited by β -adrenergic blocking agents (*e.g.*, propranolol). The sympathetic postganglionic fibers innervate the entire heart, including the SA node, the AV conducting pathways and the atrial and ventricular myocardium. Increased activity in the sympathetic nerves results in increases in both HR and the force of contraction. Also, the rate of conduction through the heart of the cardiac impulse is increased and the duration of contraction is shortened.

The effects of sympathetic stimulation decay very *gradually* after the cessation of stimulation. This is because most of the norepinephrine released is taken up again by the nerve terminals and much of the remainder is carried away by the blood stream. These processes are relatively slow. Additionally, the facilitatory effects of sympathetic stimulation on the heart attain steady state values much more slowly than do the inhibitory effects of vagal stimulation. Therefore, vagal activity can exert beat-to-beat control of cardiac function, whereas sympathetic activity cannot.

Baroreceptor Reflex

There is abundant evidence that both the vagal and sympathetic nerves carry not only efferent fibers, but also many afferent fibers that subserve various reflex functions [43]. Arterial baroreceptors and their reflex effects have been studied very extensively both in animals and humans [33, 44, 87, 109]. Baroreceptors are situated in the adventitia of some arteries, particularly the *carotid sinuses* and the *aortic arch*. Increases in arterial blood pressure stretch these vessels and then result in increases in discharge rate in their afferent nerves. Following an increase in blood pressure, the discharge increases abruptly but then rapidly adapts to a rate which may be only moderately raised.

Stimulation of baroreceptors results in increases in efferent cardiac vagal activity and decreases in sympathetic activity. That is, acute changes in arterial blood pressure will reflexly elicit inverse changes in HR via the baroreceptors located in the carotid sinuses and aortic arch. In general, such an inverse relation between HR and arterial blood pressure is usually most pronounced over an intermediate range of arterial blood pressures. Below the range of arterial blood pressures, the high HR is achieved by intense sympathetic activity and the virtual absence of vagal activity.

Contrarily, above this intermediate range, the low HR is achieved by intense vagal activity and a constant low level of sympathetic activity.

Other Reflexes

Bainbridge noted that HR could be influenced by atrial size in 1915. He proposed a reflex linking atrial size to the firing of parasympathetic fibers so that an increase in atrial size led to a decrease in cardiac vagal efferent activity and an increase in HR. In fact, atrial receptors are stimulated mainly by stretching due to increases in atrial volume. Their discharge rate is directly related to atrial pressure. The reflex response is to subserve the Bainbridge reflex, which is to increase HR in response to an increase in venous return [65]. The atrial receptors are located in the venoatrial junctions— in the right atrium at its junctions with the venae cavae; in the left atrium at its junctions with the pulmonary veins.

The cardiac response to peripheral chemoreceptor stimulation is the resultant of primary and secondary reflex mechanisms. The primary reflex effect of carotid chemoreceptor excitations is mainly to *excite* the medullary vagal center and thus to decrease HR. The secondary effects are mediated by the respiratory system. The respiratory stimulation by the arterial chemoreceptors produces hypocapnia and increases lung inflation and then tends to *inhibit* the medullary vagal center. Hence, the primary and secondary effects tend to *neutralize* each other and carotid chemoreceptor influences HR only minimally.

Respiratory Sinus Arrhythmia

Respiratory sinus arrhythmia (RSA) can be defined simply as the variations in HR that occur simultaneously with respiratory activity. Respiration influences a large

number of autonomic and hemodynamic parameters, leading to a variety of proposed physiological mechanisms for the origin of RSA. In fact, rhythmic variations in HR occurring at the respiratory frequency are detectable in most individuals. It has been noted that RSA is both a frequency- and an amplitude-dependent phenomenon [8, 29, 32, 47]. In this aspect, it was concluded that (1) at a given respiratory frequency, the amplitude of the change in HR increases as the tidal volume increases, and (2) for a given tidal volume, the amplitude of the change in HR decreases as the respiratory frequency increases. It is also noted that RSA usually diminishes with increasing age [47]. Additionally, most investigations suggest that cardiac vagal efferents are involved in mediating the HR fluctuations that occur with respiration. That is, RSA is predominantly or exclusively mediated by respiratory gating of parasympathetic efferent activity to the heart [40, 41, 89]. This is because the acetylcholine released at the vagal endings is removed so rapidly that the rhythmic changes in activity can elicit rhythmic variations in HR. Therefore, RSA is exaggerated when vagal tone is enhanced. Recordings from the autonomic nerves to the heart reveal that the neural activity increases in the sympathetic fibers during inspiration, whereas the neural activity increases in the vagal fibers during expiration. Since respiration continually perturbs cardiovascular hemodynamics, it has the potential to influence cardiac autonomic efferent activity through a variety of direct and indirect mechanisms (as shown in Fig. 1.2) described below.

Both reflex and central factors contribute to the genesis of the RSA. Observing Fig. 1.2, we see that during inspiration the intrathoracic pressure decreases and thus, venous return to the right atrium is accelerated so that atrial stretch is increased, eliciting the Bainbridge reflex to increase HR. After a period of time required for

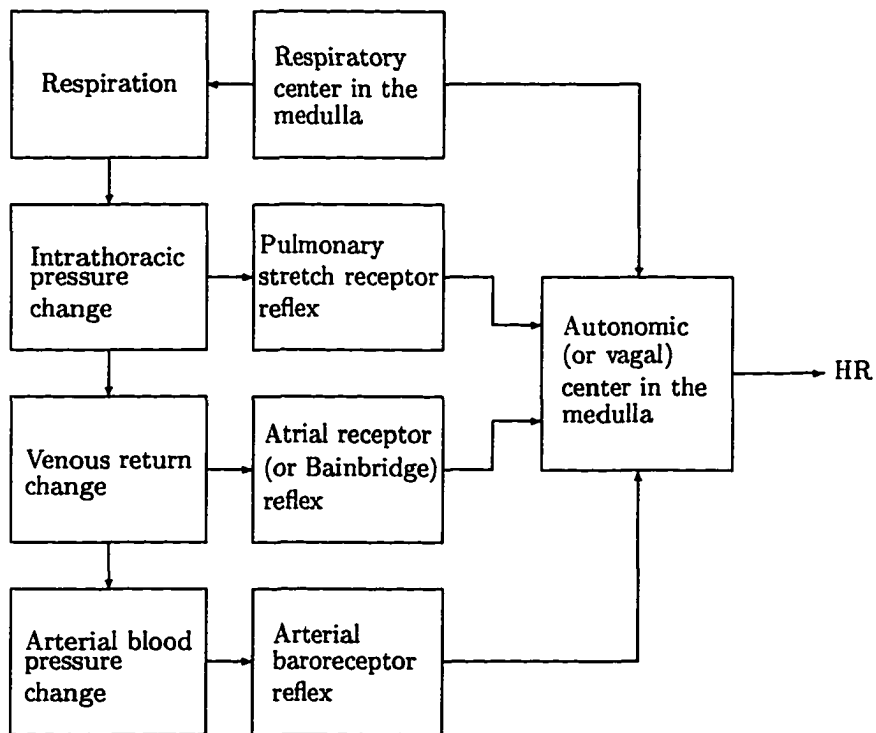


Figure 1.2: Factors contributed to RSA. Respiration influences a wide range physiological parameters through its mechanical effects and through direct links in the central nervous system.

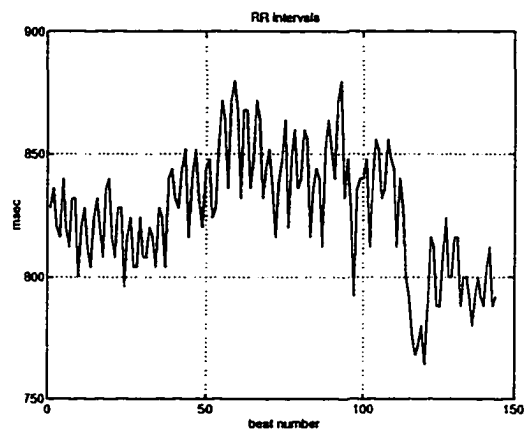
the increased venous return to arrive the left ventricle, cardiac output increases and arterial blood pressure is thus raised. HR is then reflexly decreased through baroreceptor stimulation. Also, stretch receptors in the lungs may also affect HR. Moderate pulmonary inflation may increase HR reflexly. The afferent and efferent limbs of this reflex are located in the vagal nerves. In addition, central factors are also responsible for RSA. That is, a direct interaction between the respiratory and cardiac autonomic (vagal) centers in the medulla generates RSA as well.

1.1.2 HRV Analysis

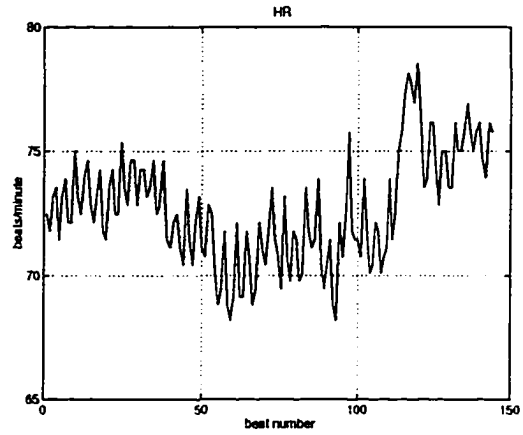
For the intact cardiovascular system (see Fig. 1.1), feedback and control mechanisms are particularly efficient at maintaining the mean value of *arterial blood pressure* (ABP) and central venous volume within a narrow range by constant regulation of HR and vascular tone. Certainly, quantifying the changes in the mean value of ABP or HR may not reveal substantial responses in the underlying control system during periods of hemodynamic stress. Alternatively, analysis of beat-to-beat variability of cardiac parameters such as HR and ABP can provide specific quantitative information about modulation of cardiac parasympathetic, cardiac sympathetic, and peripheral sympathetic nervous activity [4, 96, 98]. Thus, interest in HRV in the medical community is based on the possible use of measures of HRV to indicate ANS activity. From the above studies, it was clear that the HRV signal consists well-defined rhythms, which have been successfully shown to contain physiological information. Figs. 1.3(a)–(c) give an RR-interval signal, HR signal and power spectral plot of the RR signal, respectively, from a normal individual who was breathing quietly. Experiments using pharmacologic blockade of the sympathetic and parasympathetic inputs to the SA

node have demonstrated that HR fluctuations at frequencies > 0.15 Hz are mediated virtually completely by vagal activity (due primarily to respiration), whereas those at frequencies < 0.15 Hz are mediated by both vagal and sympathetic activities (mainly due to baroreflex elicited by ABP change). Long period rhythms at frequencies < 0.03 Hz may be mediated by neurohormones and these rhythms account for the long-term regulation mechanisms probably related to thermoregulation, to the renin-angiotensin system and to other humoral factors. The power spectrum shown in Fig. 1.3(c) depicts these three main contributions to the total power which are well identifiable in three different frequency ranges. It should be noted that the above findings actually allow a precise description of response characteristics of HR to ANS inputs as a function of frequency.

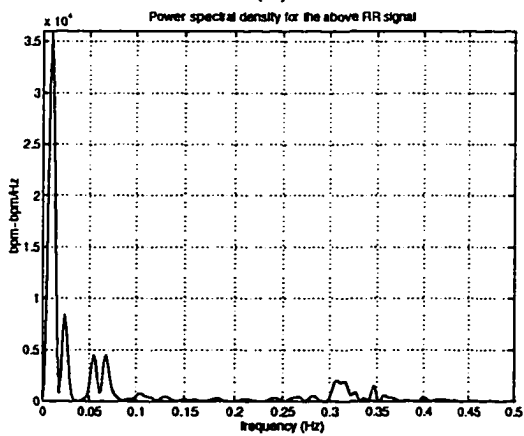
In addition to having proven useful in understanding cardiovascular in normal adults, alterations in autonomic nervous tone are observed in different disease states. The critical importance of normal HRV was first elucidated in the observations of fetal HR, where it became clear that absence of the normal beat-to-beat variability of HR would indicate an abnormal central nervous modulation of HR and thus might be an indication for emergency Caesarean operation. Furthermore, there is evidence to show that the HRV measures are altered by various disease states, such as diabetes [34, 58, 66], *congestive heart failure* (CHF) [98], hypertension [76], transplantation [5, 95] and heart diseases [59], and that the abnormalities may have prognostic significance. In certain illness, these changes in ANS activity may be important modulators of patient outcome. For example, there is a large body of experimental evidence suggesting that activation of the sympathetic nervous system during *myocardial infarction* (MI)



(a)



(b)



(c)

Figure 1.3: The RR-interval signal, HR signal and RR power spectrum obtained from a normal individual: (a) RR signal; (b) HR signal; (c) power spectrum of the RR signal as given in (a).

greatly increases the chance that a fatal cardiac arrhythmia may occur. In contrast, parasympathetic activation appears to be protective in this setting [30].

It has been reported that lethal heart rate fluctuations show a diminution in the beat-to-beat variability [23, 69, 83, 97]. In particular, measures of HRV may have prognostic value in patients recovering from MI. Several studies have found that a decrease in the range of RR intervals is associated with increased mortality after MI [59, 67, 83]. All these studies suggested that the degree of variability could be a predictor of cardiac pathology in otherwise asymptomatic individuals. While HRV analysis shows great promise in this regard, studies to date were limited either to power spectral analysis such as simple *fast Fourier transform* (FFT) algorithms [52, 51, 63, 67, 83], or to measuring rate fluctuations by quantifying variation via the *standard deviation* (SD) of the rate values, calculated over the entire recording interval [23, 51]. In addition, some studies [23, 83] have also indicated that a *small* number of the beat-to-beat differences in RR intervals above 50 ms could be a strong predictor of *sudden cardiac death* (SCD), even in previously asymptomatic individuals. Although there have been a tremendous number of studies presented for HRV research, yet the methods that were adopted are mostly developed based on the time- or frequency-domain analyses mentioned above. In fact, the suitability of these techniques for this analysis remains uncertain. For instance, FFT analysis is known as one of the simplest and most widely used spectral analysis techniques for biological signal processing [13], but it is only valid under the constraint of stationarity for the signals, so called time-invariant signals [84]. Unfortunately, HR behaves as a highly dynamic and nonstationary signal [56] and thus, the information obtained solely by applying FFT analysis may be inaccurate. As for the time-domain features, mostly

Measure	Description/Definition
SDANN	standard deviation of the averaged normal RR intervals in successive 5-minute blocks over 24 hours
SDNN	standard deviation of the set of all normal RR intervals over 24 hours
SDNN index	mean of the standard deviations of normal RR intervals in successive 5-minute blocks over 24 hours
RMSSD	root-mean-square successive difference for all normal RR intervals over 24 hours
PNN50	percentage of differences between adjacent normal RR intervals > 50 over 24 hours

Table 1.1: Definitions for time domain measures of HRV.

based on *standard deviation* (SD) calculation such as SDANN, SDNN, SDNN index, RMSSD, RR50 and so on [23, 83], are known as the most popular choices. Table 1.1 provides a list of the definitions for these time domain measures of HRV. However, SD is a notoriously non-robust estimator and also, these indices may not well reflect subtle or asynchronous variations of HR fluctuations.

Wavelet analysis is a potentially useful tool since it allows an attractive time-frequency representation of the signal. In general, the *wavelet transforms* (WT) represent the temporal characteristics of a signal by its spectral components in the frequency domain. Although it has been widely used in the signal processing of biomedical signals and the subject has grown rapidly in the past few years [1, 2], no WT-based application to HRV analysis has been reported to date. In this work, we introduce this novel method to this application.

1.1.3 The Clinical Significance of Nonsustained Ventricular Tachycardia (NSVT)

Each year more than 300,000 individuals die suddenly in the United States from cardiac disease [88]. Without organic heart disease, patients with NSVT may expect to have a normal life. On the other hand, NSVT could be a very strong predictor of cardiac arrest in patients who have cardiac diseases. The occurrence of NSVT in patients with structural heart disease may serve as a prognostic indicator of an increased risk of mortality and sudden death. Since NSVT does not pose the same risk for cardiac patients, the prognosis for patients with NSVT varies depending on the underlying type of heart disease and management/treatment thus becomes a dilemma. In general, the management of asymptomatic patients with NSVT should first attempt to stratify the risk for cardiac arrest and devise a treatment plan that can reduce the incidence of mortality due to cardiac arrest. However, the classification of such patients remains a major challenge using all existing tests. That is, there is a lack of an *effective* strategy for identifying *high-risk* patients who would benefit the most from treatment.

EPS testing, alternatively known as *programmed electrical stimulation* (PES) or *programmed ventricular stimulation* (PVS), plays an important role in the risk stratification and the management of patients with CAD and NSVT. It is used in order to characterize the inducibility and the morphology, rate and hemodynamic consequences of arrhythmias. It also guides treatment strategies, such as the selection of antiarrhythmic drug therapy and the suitability for antiarrhythmic surgery or implantation of an implantable defibrillator. This invasive technique has been devoted to risk stratification of patients after *myocardial infarction* (MI). Generally speaking, these

<i>Test</i>	<i>Risk/Prognostic Factor</i>	<i>Clinical Applications</i>
EPS	↑ Sustained monomorphic VT inducibility	CAD or post-MI
Ambulatory ECGs (Holter monitoring)	↑ Complexity or frequency of VPBs	Widespread use
Treadmill test	1. ↑ Residual ischemia 2. ↓ Exercise tolerance 3. ↑ Exercise-induced arrhythmia	CAD
Coronary angiography	↑ Vessel occlusions (LAD, LCX, RCA)	CAD
Left ventricular function	↓ LVEF	CAD or post-MI
Signal-averaged ECG	↑ Late potentials	CAD or post-MI

Table 1.2: A list of the existing tests and their associated risk factors (VT– ventricular tachycardia; CAD– coronary artery disease; VPB– ventricular premature beat; LVEF– left ventricular ejection fraction; LAD– left anterior descending coronary artery; LCX– left circumflex coronary artery; RCA– right coronary artery).

studies suggested that the induction of sustained VT in patients with impaired left ventricular function, chronic *coronary artery disease* (CAD) and spontaneous NSVT may identify a subgroup at high risk of SCD and similar patients without inducible sustained VT are at much lower risk. However, in [62, 106] both studies indicated while that the noninducible VT implies a low risk group has been well established, the EPS-directed therapy of the inducible patients still have limited efficacy.

Also, a number of risk stratification efforts have been devoted to patients with NSVT and known cardiac diseases. In particular, the CAD or post-MI patient population is the most convenient group for these studies. Table 1.2 provides a list of the existing tests reported to be of value in identifying high-risk NSVT patients. Note that no single test can solely achieve a complete assessment of a patient’s risk. But that combination of several tests might be very helpful.

In addition to serving as a risk predictor, NSVT itself is also known as a risk factor. Therefore, the prediction of NSVT is important clinically as well. As described

previously, HRV can be measured in a number of ways and is known as a useful index of autonomic tone. It is also noted that autonomic activity plays an important role in the genesis of lethal arrhythmias [22]. The applications of HRV analysis to the assessment of NSVT, however, have not been widely explored and only limited studies have been reported to date [36, 49, 105]. Fei *et al.* [36] assessed spectral HRV immediately before the onset of NSVT based on STFT analysis. They found that the power ratio LF/HF had increased for a period of from 2 to 18 minutes before VT in comparison with mean LF/HF over 24 hours (1.67 ± 0.63 vs. 1.24 ± 0.60 , $p < 0.001$) and that such an increment was mostly due to decreased HF (4.70 ± 1.15 vs. 5.10 ± 1.06 $\ln[\text{ms}^2]$, $p = 0.001$) while LF remained unchanged (6.37 ± 1.20 vs. 6.34 ± 0.91 $\ln[\text{ms}^2]$, $p = 0.786$). This conclusion is questionable, however, because the distributions for all comparison pairs appeared *seriously* overlapped. Also, since circadian variability of an individual could be very significant within a day, the assessment of HRV right before the onset of NSVT might be *misleading* if simply compared with the averaged LF/HF over the entire 24-hour period. Vybiral *et al.* [105] reported that there is no significant change in the time-domain HRV before the onset of spontaneous ventricular fibrillation. As for the prognostic value of HRV to NSVT, Farrell *et al.* [35] suggested that a decreased HRV was more predictive of arrhythmic events than the signal-averaged ECG (the presence of late potentials), frequent VPBs, treadmill test or LVEF. Additionally, they found that in multivariate analysis of combinations of risk factors, the combination of late potentials by SAECG and reduced HRV was more predictive than any other combination. However, direct evidence for a change or derangement in HRV immediately before the onset of NSVT is still scarce and remains to be fully defined.

In this dissertation research, we aim to improve the measurement of HRV as a predictor of NSVT based on the wavelet method first, and then to assess HRV prior to the onset of episodes of spontaneous NSVT such that the noninvasive risk stratification as well as the mortality prediction tasks for cardiac patients with NSVT may be achieved.

1.2 Contribution of this Research Work

According to the description above, it is known that the *autonomic balance status* (ABS) can be quantified by HR via the LF to HF spectral power ratio. In this research work, we study the relationship between ANS and NSVT by assessing short-term ABS immediately before the onset of NSVT. A novel WT-based scheme for HRV assessment is introduced. Due to the characteristic of varying *frequency resolutions* (FR), the WT can optimize the use of time-frequency information so that instantaneous ABS may be measured over a very fast time frame (8-second period) far more accurately than via the traditional *short-time Fourier transform* (STFT) based analysis which employs a fixed FR. A morphological information marker α is then used to indicate the behavior of ABS waveform. In general, a large α may imply a trend of (1) more, or (2) unusually large peaks relative to the entire ABS waveform.

1.3 Overview

This dissertation is organized as follows. Chapter 2 provides a summary of the underlying theory of the WT-based multiresolution method. In Chapter 3, the rationale and numerical experiments of the validation task for the application of this method

to HRV analysis are described. A comparison of the performances respectively obtained by applying WT-based multiresolution and STFT analyses to HRV data for a group of control subjects is also included in Chapter 3. In Chapter 4 we describe the application of wavelets to the prediction of NSVT in patients with organic cardiac disease. In addition to the prediction task, descriptions of the pattern classification methods used to separate NSVT/non-NSVT classes are also presented in this chapter. Chapter 5 provides a performance evaluation for the proposed methods by further analyzing the numerical results obtained in Chapter 4 and also, provides a discussion of some underlying clinical implications revealed by these numerical results. Finally, in Chapter 6, we summarize this research work as well as suggest potential extensions of this work for future exploration.

CHAPTER 2

REVIEW OF WAVELET TRANSFORM-BASED TECHNIQUES

Wavelet analysis methods have been widely used in the signal processing of biomedical signals [1, 2]. In general, these methods represent the temporal characteristics of a signal by its spectral components in the frequency domain. Being a powerful alternative for the analysis of nonstationary signals whose spectral features are changing over the course of time, wavelet analysis is very important to the analysis of biological signals since most of the statistical characteristics of these signals are nonstationary. The term “wavelet” was first introduced by Grossman and Morlet [39] to describe how a square integrable function forms a basis for $L^2(\mathcal{R})$ with appropriate translations and dilations. Then, Daubechies [25, 26] and Mallat [72] related wavelet theory to discrete signal processing. Due to a number of theoretical and practical contributions, the subject has grown rapidly in the past few years [1].

Generally speaking, the basis functions in $L^2(\mathcal{R})$ used for *wavelet transforms* (WTs) are referred to as wavelets. Thus, the study of wavelets is the study of bases for $L^2(\mathcal{R})$ which have the property that all of the basis functions are self-similar and differ only by translation and change of scale from one another. In signal processing applications, orthogonal wavelets are used almost exclusively although there exist

non-orthogonal wavelets [21]. A wavelet can be visualized as a damped sinusoidal wave with very small amplitude (perhaps zero) outside some bounded interval, and with a somewhat distorted shape so that the orthogonality conditions all hold. Because the wavelets used in practice usually vanish outside a bounded interval, this *compactly supported* characteristic allows the WT to transfer a time-domain function into a representation that is localized not only in frequency but also in time as well, permitting a good time resolution at HF and good frequency resolution at LF. In this section, a brief introduction to wavelet analysis is presented. The description is mainly based on discussing the design and implementation of the orthonormal WTs, so called *multiresolution analysis* (MRA).

2.1 Continuous Wavelet Transform (CWT)

We begin from the *continuous wavelet transform* (CWT) with notations. Denote $L^2(\mathcal{R})$ as the space of square integrable functions in real number line, *i.e.*,

$$L^2(\mathcal{R}) = \{f(x) : \|f(x)\|^2 = \int_{-\infty}^{\infty} |f(x)|^2 dx < \infty\}. \quad (2.1)$$

The inner product of two functions $f(x), g(x) \in L^2(\mathcal{R})$ is given by

$$\langle f(x), g(x) \rangle = \int_{-\infty}^{\infty} f(x)g^*(x)dx, \quad (2.2)$$

and the *Fourier transform* (FT) of a function $f(x) \in L^2(\mathcal{R})$ is thus defined as

$$F(\omega) = \langle f(x), e^{j\omega x} \rangle = \int_{-\infty}^{\infty} f(x)e^{-j\omega x}dx. \quad (2.3)$$

Assume that the signals we encounter are in $L^2(\mathcal{R})$ (*i.e.*, finite energy signals). Also, assume that the analyzing functions come from a fixed function $\psi(x) \in L^2(\mathcal{R})$, so called “mother wavelet,” and they are formed by using a variety of translations

and dilations of $\psi(x)$. In other words, the analyzing functions are expressed by

$$\psi_{a,b}(x) = \frac{1}{\sqrt{|a|}} \psi\left(\frac{x-b}{a}\right) \quad \text{with } a, b \in \mathbb{R}; a \neq 0. \quad (2.4)$$

Typically, a mother wavelet needs to satisfy two constraints– (1) it must decay with respect to time:

$$\lim_{x \rightarrow \infty} |\psi(x)| = 0 \quad (2.5)$$

and (2) its integral over the entire time axis must vanish:

$$\int_{-\infty}^{\infty} \psi(x) dx = 0. \quad (2.6)$$

Both constraints will guarantee that the analyzing functions $\psi_{a,b}(x)$ are well localized and oscillate like a wave. Observing Eq. 2.4 we can see that as a decreases, $\psi_{a,b}(x)$ shrinks and gets localized in time and simultaneously, the FT of $\psi_{a,b}(x)$ increases in band width, resulting in poor frequency resolution. When a becomes larger, $\psi_{a,b}(x)$ dilates in time and gets localized in frequency. Hence, the frequency resolution improves at the expense of the time resolution. Note that these functions are scaled by a factor of $\frac{1}{\sqrt{|a|}}$ so that their $L^2(\mathbb{R})$ norms are independent of a and identical one another. That is,

$$\begin{aligned} \|\psi_{a,b}\|^2 &= \frac{1}{|a|} \int_{-\infty}^{\infty} \psi\left(\frac{x-b}{a}\right) \psi^*\left(\frac{x-b}{a}\right) dx \\ &= \frac{1}{|a|} \int_{-\infty}^{\infty} |a| \psi(\xi) \psi^*(\xi) d\xi \\ &= \int_{-\infty}^{\infty} \psi(\xi) \psi^*(\xi) d\xi \\ &= \|\psi\|^2. \end{aligned} \quad (2.7)$$

Actually, this norm-identity guarantees energy preservation. The *continuous wavelet transform* (CWT) of a function $f(x) \in L^2(\mathbb{R})$ is then defined as

$$W_\psi f(a, b) = \langle f(x), \psi_{a,b}(x) \rangle$$

$$= \frac{1}{\sqrt{|a|}} \int_{-\infty}^{\infty} f(x) \psi^*\left(\frac{x-b}{a}\right) dx. \quad (2.8)$$

In wavelet analysis, we always set the translation parameter $b = ka$, $k \in Z$ and usually set the scale parameter $a = 2^{-j}$, $j \in Z$ (a is not restricted to powers of 2) so that $\psi_{a,b}(x)$ becomes the form

$$\psi_{a,b}(x) = 2^{j/2} \psi(2^j x - k) = \psi_{j,k}(x) \quad \text{with } j, k \in Z. \quad (2.9)$$

The family $\{\psi_{j,k}(x) : j, k \in Z\}$ is referred to as the family of wavelets derived from the wavelet ψ . The determination of ψ is based on the concept of MRA that will be described in next section.

2.2 Multiresolution Analysis

The initial goal of *multiresolution analysis* (MRA) is to state properties of a function $\phi \in L^2(R)$, the so called generating function or scaling function, from which a wavelet $\psi \in L^2(R)$ can be then derived. Given that $\phi \in L^2(R)$ and $\phi_{j,k}(x) = 2^{j/2} \phi(2^j x - k)$ (Note that here $\phi_{j,k}(x)$'s also satisfy the norm-identity, *i.e.*, $\|\phi_{j,k}\|^2 = \|\phi\|^2$), we define

$$V_0 = \overline{\text{span}\{\phi_{0,k}(x) : k \in Z\}} \quad (2.10)$$

$$V_j = \overline{\text{span}\{\phi_{j,k}(x) : k \in Z\}} = \{f(2^j x) : f \in V_0\}. \quad (2.11)$$

Thus, by definition, V_0 is the closure of the set formed by all linear combinations of translates of ϕ by integers, V_j is the set of all scaled versions, with scale factor $a = 2^{-j}$, of elements of V_0 . The set $V = \{V_j : j \in Z\}$ is then referred to as an MRA of $L^2(R)$ if the following conditions are satisfied:

1. V forms a nested sequence of closed subspaces: $V_j \subset V_{j+1}$, for all $j \in Z$,

2. $f(x) \in V_j \Leftrightarrow f(2x) \in V_{j+1}$, for all $j \in Z$,
3. $f(x) \in V_j \Leftrightarrow f(x - n) \in V_j$, for all $n \in Z$,
4. $\bigcap_{j \in Z} V_j = \{0\}$,
5. $\bigcup_{j \in Z} V_j$ is dense in $L^2(R)$,
6. There exists a scaling function $\phi \in V_0$ with a non-zero integral (i.e., $\int_{-\infty}^{\infty} \phi(x) dx \neq 0$) and its integer translates, $\{\phi(x - k) : k \in Z\}$, forms a basis for V_0 .

Now, we can develop the wavelet analysis from the concept of MRA. By condition 1 above, since V_{j+1} is a larger space than V_j , we may speculate that there exists a “detail” space, W_j , so that $V_{j+1} = V_j \oplus W_j$ where $V_j \perp W_j$. In other words, the space W_j contains the detail information needed to go from V_j to V_{j+1} ; similarly, the details peeled off while going from V_{j+1} to V_j are stored in W_j . Symbol \oplus denotes the *orthogonal direct sum* (ODS) of V_j and W_j .¹ Using the recursive form, we have

$$V_{j+1} = \cdots \oplus W_{j-3} \oplus W_{j-2} \oplus W_{j-1} \oplus W_j = \bigoplus_{n=-\infty}^j W_n, \quad (2.12)$$

where $W_l \perp W_m$ for $l \neq m$. Therefore, we can finally conclude that

$$\bigoplus_{n \in Z} W_n = L^2(R). \quad (2.13)$$

Eq. 2.13 shows that there exists an ODS decomposition of $L^2(R)$, implying that for every $f(x) \in L^2(R)$, it has a unique expression as

$$f(x) = \sum_{j \in Z} g_j(x), \quad g_j(x) \in W_j. \quad (2.14)$$

¹Note that $V = S_1 \oplus S_2$ represents that a Hilbert space V is the “orthogonal direct sum” of closed subspaces S_1 and S_2 if: (1) for every $v \in V$, there only exist a unique $s_1 \in S_1$ and a unique $s_2 \in S_2$ such that $v = s_1 + s_2$ and (2) $S_1 \perp S_2$, i.e., $\langle s_1, s_2 \rangle = 0$ for all $s_1 \in S_1$ and $s_2 \in S_2$.

We now turn to the construction of the wavelet ψ . This construction presumes that the $\phi_{0,k}$'s are orthonormal and real-valued. Thus, the function $\psi \in W_0$ which we will construct has the properties that the $\psi_{0,k}$'s (defined by Eq. 2.9) are orthonormal real-valued functions and that $\{\psi_{0,k}(x) = \psi(x - k) : k \in Z\}$ forms a basis for W_0 . Then, we immediately have $\{\psi_{j,k}(x) = 2^{j/2}\psi(2^j x - k) : k \in Z\}$ forms a basis for W_j . This is the key-point of MRA since it gives a general algorithm for the construction of wavelet bases for $L^2(R)$. Furthermore, since $W_j \perp W_{j'}$ for $j \neq j'$ and $\psi_{j,k}$'s are orthonormal wavelets at j th level, we have

$$\langle \psi_{j,k}, \psi_{j',k'} \rangle = \int_{-\infty}^{\infty} \psi_{j,k} \psi_{j',k'}^* dx = \delta_{jj'} \delta_{kk'}. \quad (2.15)$$

That is, $\psi_{j,k}$'s have the orthogonality between levels (scales) and translates. Thus, $\Psi = \{\psi_{j,k}(x) : j, k \in Z\}$ represents an orthonormal family of wavelets. This normally implies that Ψ serves as a basis for $L^2(R)$. Therefore, any function $f(x) \in L^2(R)$ has a series expansion of the form

$$f(x) = \sum_{j,k \in Z} d_j(k) \psi_{j,k}(x) \quad (2.16)$$

and the coefficients $\{d_j(k)\}$ are called WT of the function $f(x)$, where

$$d_j(k) = \langle f(x), \psi_{j,k}(x) \rangle = W_\psi f(2^{-j}, k2^{-j}), \quad (2.17)$$

consistent to Eq. 2.8.

2.3 Filter Banks and Fast Wavelet Transform

In this section, the applications of filter banks to the calculation of *fast wavelet transform* (FWT), or known as *discrete wavelet transform* (DWT), is described. Since $\phi \in V_0 \subset V_1$ and $\{\sqrt{2}\phi(2x - n) : n \in Z\}$ is a basis of V_1 , we have

$$\phi(x) = \sum_n \sqrt{2}h(n)\phi(2x - n). \quad (2.18)$$

Eq. 2.18 is referred to as the *dilation equation* or *two-scale difference equation*. Also, $\psi \in W_0 \subset V_1$ since $V_1 = V_0 \oplus W_0$, therefore

$$\psi(x) = \sum_n \sqrt{2}g(n)\phi(2x - n). \quad (2.19)$$

The design of a wavelet analysis involves the estimates of $\phi(x)$, $h(n)$ and $g(n)$. In fact, the wavelet analysis can be started either by carefully selecting the scaling function $\phi(x)$ or by choosing the appropriate scaling and wavelet filter coefficients $h(n)$ and $g(n)$. It is, however, very difficult to solve for $\phi(x)$ and $\psi(x)$ and usually we do not need to do that in practice. In many applications, we work directly with $h(n)$ and $g(n)$ instead of $\phi(x)$ so that the wavelet computations can be easily and fastly performed simply by employing these filter coefficients. Since we note that $V_0 \perp W_0$ implies $\phi(x) \perp \psi(x)$, this is followed by

$$\begin{aligned} \langle \phi(x), \psi(x) \rangle &= 0 \\ \Rightarrow \langle \sum_n \sqrt{2}h(n)\phi(2x - n), \sum_n \sqrt{2}g(n)\phi(2x - n) \rangle &= 0 \\ \Rightarrow \sum_n h(n)g(n) &= 0. \end{aligned} \quad (2.20)$$

Therefore, according to Eq. 2.20 we see that once $h(n)$ is given, a possible solution for $g(n)$ is thus given by

$$g(n) = (-1)^n h(1 - n). \quad (2.21)$$

We now start to describe how to use the filter bank concept to perform an FWT calculation. Using the recursions in Eq. 2.18, we then obtain

$$\begin{aligned} \phi(2^j x - k) &= \sum_n \sqrt{2}h(n)\phi(2(2^j x - k) - n) \\ &= \sum_m \sqrt{2}h(m - 2k)\phi(2^{j+1}x - m), \end{aligned} \quad (2.22)$$

where $m = 2k + n$ (variable change). Multiplying both sides by $2^{j/2}$, Eq. 2.22 then has the form as

$$\phi_{j,k}(x) = \sum_m h(m - 2k)\phi_{j+1,m}(x). \quad (2.23)$$

Similarly, Eq. 2.19 leads to

$$\psi_{j,k}(x) = \sum_m g(m - 2k)\phi_{j+1,m}(x). \quad (2.24)$$

Now, consider a function $f(x) \in V_{j+1}$. $f(x)$ has a series form as

$$f(x) = \sum_k c_{j+1}(k)\phi_{j+1,k}(x). \quad (2.25)$$

Also, since $V_{j+1} = V_j \oplus W_j$ is known, $f(x)$ can be alternatively expressed by

$$f(x) = \sum_k c_j(k)\phi_{j,k}(x) + \sum_k d_j(k)\psi_{j,k}(x). \quad (2.26)$$

Based on the assumption made previously, we know that both $\phi_{j,k}$ and $\psi_{j,k}$ are orthonormal. Equating Eqs. 2.25 and 2.26 and then taking inner product operations with $\phi_{j,k}$ (using the expression in Eq. 2.23) and with $\psi_{j,k}$ (using the expression in Eq. 2.24), we thus obtain

$$c_j(k) = \sum_m h(m - 2k)c_{j+1}(m) \quad (2.27)$$

and

$$d_j(k) = \sum_m g(m - 2k)c_{j+1}(m), \quad (2.28)$$

respectively, where c_j represents the *scaling function coefficients* in V_j (coarse); d_j denotes the *wavelet coefficients* in W_j (detail). Similarly, we can also obtain a synthesis form as

$$c_{j+1}(k) = \sum_m h(k - 2m)c_j(m) + \sum_m g(k - 2m)d_j(m). \quad (2.29)$$

Therefore, Eqs. 2.27– 2.28 define the FWT and Eq. 2.29 defines its inverse version (IFWT); the relations in Eqs. 2.27 and 2.28 define the *forward transform* used for analysis (signal decomposition), while Eq. 2.29 defines the *inverse transform* used for synthesis (signal reconstruction).

Observing Figs. 2.1(a) and (b), we can get the idea of the implementations of FWT and IFWT, respectively, from the filter bank structures. Fig. 2.1(a) is the realization form of Eqs. 2.27 and 2.28, whereas Fig. 2.1(b) is that of Eq. 2.29. Generally speaking, Fig. 2.1(a) demonstrates the next lower level signal decomposition. Letting $\tilde{h}(k) = h(-k)$ and $\tilde{g}(k) = g(-k)$, the scaling coefficients $c_j(k)$ and wavelet coefficients $d_j(k)$ can be obtained by first performing a convolution between $c_{j+1}(k)$ and $\tilde{h}(k)$, and between $c_{j+1}(k)$ and $\tilde{g}(k)$, respectively, and then downsampling both the resultant signals by a factor of 2. Similarly, Fig. 2.1(b) provides the demonstration of the next higher level signal reconstruction. For example, to reconstruct $c_{j+1}(k)$ from $c_j(k)$ and $d_j(k)$, we first upsample $c_j(k)$ and $d_j(k)$ by a factor of 2 (scheme: putting *zero* between the consecutive samples), then filter both the upsampled signals using $h(k)$ and $g(k)$, respectively, and finally add both the resultant signals to get $c_{j+1}(k)$.

Define a matrix \mathbf{H} by $H_{km} = h(m - 2k)$ and note that here the size of \mathbf{H} is infinite (*i.e.*, $-\infty$ th, \dots , -1 th, 0 th, 1 th, \dots , ∞ th rows and columns). The k th row is the 0 th row shifted to the right by $2k$ units if $k > 0$, or to the left by $2|k|$ units if $k < 0$. \mathbf{H} , in fact, has a circulant structure. Similarly, define a matrix \mathbf{G} by $G_{km} = g(m - 2k)$ and \mathbf{G} has the same circulant structure as \mathbf{H} . According to Eqs. 2.23 and 2.24, we see that the matrix

$$\mathbf{W} = \begin{bmatrix} \mathbf{H} \\ \mathbf{G} \end{bmatrix}$$

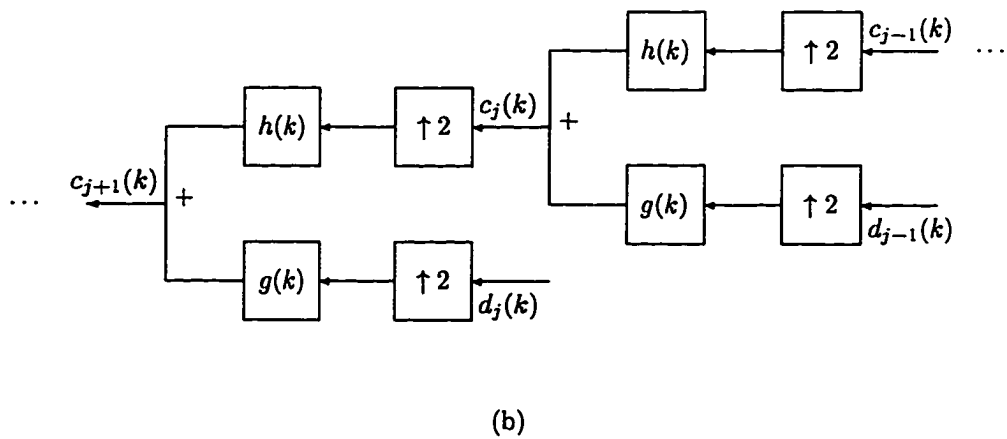
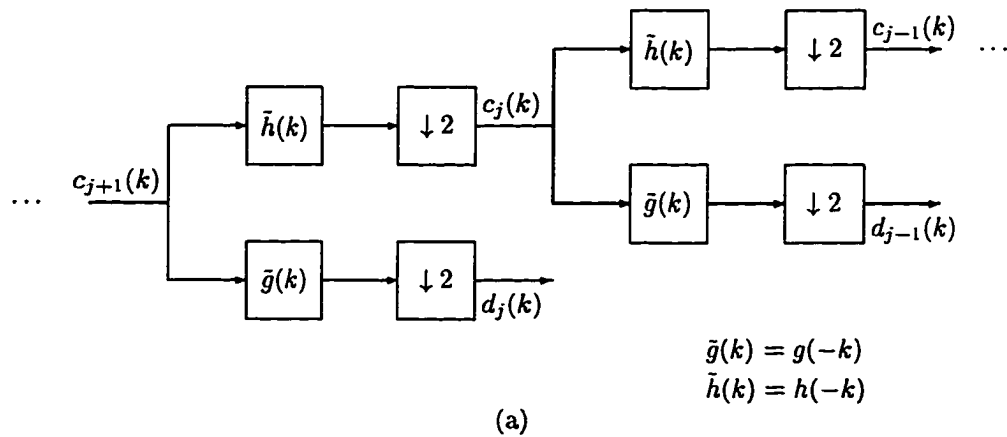


Figure 2.1: (a) Implementation of FWT using a filter bank structure (analysis decomposition scheme); (b) implementation of IFWT using a filter bank structure (synthesis reconstruction scheme).

is the matrix of an orthonormal basis change from the basis $\{\phi_{j+1,k}(x) : k \in Z\}$ to the basis $\{\phi_{j,k}(x), \psi_{j,k}(x) : k \in Z\}$ in V_{j+1} . Therefore, \mathbf{W} is necessarily *unitary* and *real*. We thus have

$$\mathbf{W}\mathbf{W}^T = \begin{bmatrix} \mathbf{H} \\ \mathbf{G} \end{bmatrix} \begin{bmatrix} \mathbf{H}^T & \mathbf{G}^T \end{bmatrix} = \begin{bmatrix} \mathbf{H}\mathbf{H}^T & \mathbf{H}\mathbf{G}^T \\ \mathbf{G}\mathbf{H}^T & \mathbf{G}\mathbf{G}^T \end{bmatrix} = \mathbf{I} \quad (2.30)$$

and

$$\mathbf{W}^T\mathbf{W} = \begin{bmatrix} \mathbf{H}^T & \mathbf{G}^T \end{bmatrix} \begin{bmatrix} \mathbf{H} \\ \mathbf{G} \end{bmatrix} = \mathbf{H}^T\mathbf{H} + \mathbf{G}^T\mathbf{G} = \mathbf{I}. \quad (2.31)$$

The above two equations will accordingly result in the following relationships:

$$\mathbf{H}\mathbf{H}^T = \mathbf{I} \quad (2.32)$$

$$\mathbf{G}\mathbf{G}^T = \mathbf{I} \quad (2.33)$$

$$\mathbf{G}\mathbf{H}^T = \mathbf{H}\mathbf{G}^T = \mathbf{0} \quad (2.34)$$

$$\mathbf{H}^T\mathbf{H} + \mathbf{G}^T\mathbf{G} = \mathbf{I}. \quad (2.35)$$

Letting $\mathbf{h} = [h(0) \ h(1) \ \cdots \ h(p-1)]^T$ and $\mathbf{g} = [g(0) \ g(1) \ \cdots \ g(p-1)]^T$, \mathbf{h} and \mathbf{g} can be referred to as a *discrete wavelet pair* if both the matrices \mathbf{H} and \mathbf{G} , respectively defined in Eqs. 2.36 and 2.37, satisfy Eqs. 2.32– 2.35. It follows that we can obtain discrete wavelet pairs with desirable properties without going through the process of constructing a multiresolution analysis [21]. Instead, we can directly solve Eqs. 2.32 through 2.35.

Furthermore, the FWT computation can be also performed simply using the operators \mathbf{W} , \mathbf{H} and \mathbf{G} . Let \mathbf{f} be a discrete signal with a finite length of $N = 2^M$. A

natural decimation of the finite-length signal \mathbf{f} occurs in the FWT process. Assume that $h(n) = 0$ for $n < 0$ and $n > p-1$ for some positive integer p . For each scale level $j \in \{-1, -2, \dots, -K\}$ (K is a positive integer), let \mathbf{H}_j and \mathbf{G}_j be $2^{M+j} \times 2^{M+j+1}$ dimensional matrices, defined by the finite dimensional analogues of \mathbf{H} and \mathbf{G} , *i.e.*,

$$\mathbf{H}_j = \begin{bmatrix} h(0) & h(1) & h(2) & \cdots & h(p-1) & 0 & 0 & 0 & \cdots & 0 \\ 0 & 0 & h(0) & \cdots & h(p-3) & h(p-2) & h(p-1) & 0 & \cdots & 0 \\ \vdots & \vdots & \ddots & \ddots & \ddots & \ddots & \ddots & \ddots & \ddots & \ddots \\ 0 & 0 & 0 & \cdots & \cdots & 0 & 0 & 0 & h(0) & h(1) \end{bmatrix} \quad (2.36)$$

and

$$\mathbf{G}_j = \begin{bmatrix} g(0) & g(1) & g(2) & \cdots & g(p-1) & 0 & 0 & 0 & \cdots & 0 \\ 0 & 0 & g(0) & \cdots & g(p-3) & g(p-2) & g(p-1) & 0 & \cdots & 0 \\ \vdots & \vdots & \ddots & \ddots & \ddots & \ddots & \ddots & \ddots & \ddots & \ddots \\ 0 & 0 & 0 & \cdots & \cdots & 0 & 0 & 0 & g(0) & g(1) \end{bmatrix}, \quad (2.37)$$

where \mathbf{H}_{-1} or \mathbf{G}_{-1} is $2^{M-1} \times 2^M$, \mathbf{H}_{-2} or \mathbf{G}_{-2} is $2^{M-2} \times 2^{M-1}$, \dots and so forth. In practice, we stop generating \mathbf{H}_j and \mathbf{G}_j when the number of columns in both matrices $2^{M+j+1} < p$. Obviously, here we have $2^{M-K+1} > p$ for some $K \leq M$. At the same time, it can be inferred that the filter length p determines the maximum number of scales used in FWT. Define an operator \mathbf{W}_j as

$$\mathbf{W}_j = \begin{bmatrix} \mathbf{H}_j \\ \mathbf{G}_j \end{bmatrix}.$$

Now, in order to perform the FWT or DWT, denoted as $W_{-K}\mathbf{f}$, we can simply apply the operator \mathbf{W}_j to the coarse signal at each scale level:

$$\begin{aligned} W_{-1}\mathbf{f} &= \mathbf{W}_{-1}\mathbf{f} = \begin{bmatrix} \mathbf{H}_{-1}\mathbf{f} \\ \mathbf{G}_{-1}\mathbf{f} \end{bmatrix} \\ W_{-2}\mathbf{f} &= \begin{bmatrix} \mathbf{W}_{-2}\mathbf{H}_{-1}\mathbf{f} \\ \mathbf{G}_{-1}\mathbf{f} \end{bmatrix} = \begin{bmatrix} \mathbf{H}_{-2}\mathbf{H}_{-1}\mathbf{f} \\ \mathbf{G}_{-2}\mathbf{H}_{-1}\mathbf{f} \\ \mathbf{G}_{-1}\mathbf{f} \end{bmatrix} \\ W_{-3}\mathbf{f} &= \begin{bmatrix} \mathbf{W}_{-3}\mathbf{H}_{-2}\mathbf{H}_{-1}\mathbf{f} \\ \mathbf{G}_{-2}\mathbf{H}_{-1}\mathbf{f} \\ \mathbf{G}_{-1}\mathbf{f} \end{bmatrix} = \begin{bmatrix} \mathbf{H}_{-3}\mathbf{H}_{-2}\mathbf{H}_{-1}\mathbf{f} \\ \mathbf{G}_{-3}\mathbf{H}_{-2}\mathbf{H}_{-1}\mathbf{f} \\ \mathbf{G}_{-2}\mathbf{H}_{-1}\mathbf{f} \\ \mathbf{G}_{-1}\mathbf{f} \end{bmatrix} \end{aligned}$$

$$\begin{aligned}
& \vdots \\
W_{-K}\mathbf{f} = & \begin{bmatrix} \mathbf{H}_{-K}\mathbf{H}_{-K+1}\cdots\mathbf{H}_{-2}\mathbf{H}_{-1}\mathbf{f} \\ \mathbf{G}_{-K}\mathbf{H}_{-K+1}\cdots\mathbf{H}_{-2}\mathbf{H}_{-1}\mathbf{f} \\ \vdots \\ \mathbf{G}_{-3}\mathbf{H}_{-2}\mathbf{H}_{-1}\mathbf{f} \\ \mathbf{G}_{-2}\mathbf{H}_{-1}\mathbf{f} \\ \mathbf{G}_{-1}\mathbf{f} \end{bmatrix}. \tag{2.38}
\end{aligned}$$

The output given by Eq. 2.38 is the FWT/DWT of the original signal \mathbf{f} at scale $-K$. Note that both the DWT results obtained by applying Eqs. 2.27– 2.28 and applying Eq. 2.38 to \mathbf{f} are identical. Moreover, suppose that \mathbf{f} is a function in V_0 (*i.e.*, $\mathbf{f} \in V_0$), we may readily obtain that

$$\begin{aligned}
\mathbf{G}_{-1}\mathbf{f} & \in W_{-1}, \\
\mathbf{G}_{-2}\mathbf{H}_{-1}\mathbf{f} & \in W_{-2}, \\
\mathbf{G}_{-3}\mathbf{H}_{-2}\mathbf{H}_{-1}\mathbf{f} & \in W_{-3}, \\
& \vdots \\
\mathbf{G}_{-K}\mathbf{H}_{-K+1}\cdots\mathbf{H}_{-2}\mathbf{H}_{-1}\mathbf{f} & \in W_{-K}, \\
\mathbf{H}_{-K}\mathbf{H}_{-K+1}\cdots\mathbf{H}_{-2}\mathbf{H}_{-1}\mathbf{f} & \in V_{-K}.
\end{aligned}$$

By Eqs. 2.18 and 2.19, we see that if $\phi(x)$ and $\psi(x)$ are *compactly supported* (*i.e.*, the function value vanishes outside a bounded interval), the filters $h(k)$ and $g(k)$ are *finite impulse response* (FIR) filters so that the summations in the FWT given by Eqs. 2.27– 2.29 are finite. This apparently is of use in practical implementations. If they are not compactly supported, a fast decay is thus desirable so that the filters can be reasonably approximated by FIR filters. Note that $h(k)$ acts like a *low-pass filter* (LPF) with the passband of $[0, \pi/2]$ and $g(k)$ similarly behaves like a *high-pass filter* (HPF) with the passband of $[\pi/2, \pi]$. Both FIR filters are also known as *quadrature*

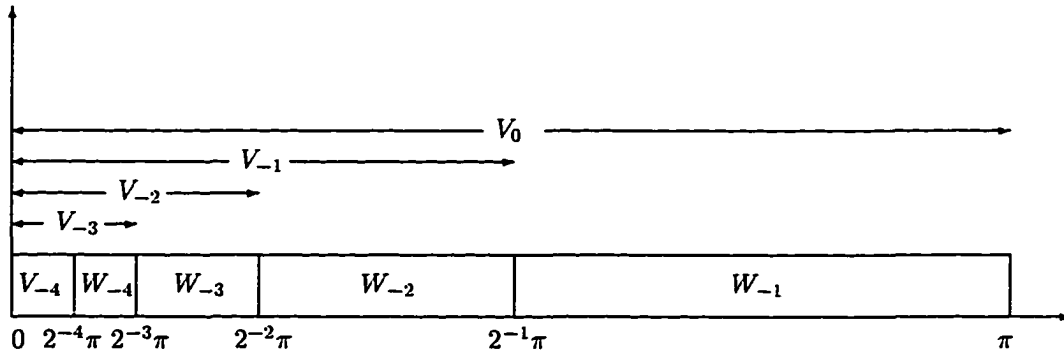


Figure 2.2: Dyadic blocks in frequency domain

mirror filters (QMF). Further, by Eq. 2.18 the FT of $\phi(x)$ must satisfy

$$\Phi(\omega) = \frac{1}{\sqrt{2}} H\left(\frac{\omega}{2}\right) \Phi\left(\frac{\omega}{2}\right), \quad (2.39)$$

implying that the major part of the energy of the function in V_0 (respectively W_0) should be concentrated in the band $[0, \pi]$ (respectively $[\pi, 2\pi]$). This means that the wavelet expansion splits the frequency space into dyadic blocks $[2^j\pi, 2^{j+1}\pi]$ with $j \in \mathbb{Z}$ [70, 71], as illustrated by Fig. 2.2.

Now that given $c_{j+1}(k)$, we know how to compute next lower level $c_j(k)$ and $d_j(k)$. But, what are the initial coefficients used to start this FWT computation process for a function $f(x)$? A trivial approximation could be

$$c_j(k) \approx f(k/2^j). \quad (2.40)$$

Therefore, we begin at level $j = 0$ and the approximated signal $c_0(k)$ can be thus given as

$$c_0(k) = f(k). \quad (2.41)$$

Then, a wavelet analysis can be obtained by successively decomposing c_j into c_{j-1} and d_{j-1} for $j \leq 0$. Also, initially the QMF filters should be determined as well. In this aspect, there are a number of existing algorithms developed for the derivations of the scaling filter $h(k)$ [25, 26, 27, 28, 70, 71, 72]. Note that these wavelets all have different properties. Once $h(k)$ is determined by using any one of these algorithms, the wavelet filter $g(k)$ can be obtained simply using Eq. 2.21.

CHAPTER 3

DESIGN AND METHOD VALIDATION OF WT-BASED ANALYSIS SCHEMES FOR HRV INVESTIGATIONS

In this chapter, we seek for some potential WT applications for HRV and then, examine the suitability of the WT-based algorithms to HRV assessments by evaluating the results obtained from a method validation task.

3.1 Rationale

The ruling action of the ANS controls is not static. Due to this dynamic action, the physiological parameters do not remain in the same stationary status but are modified by the evolving condition of the cardiovascular regulatory systems [68]. Consequently, it is noted that the HR waveform varies in different time-scale levels, *i.e.*, it varies from seconds to seconds, minutes to minutes and hours to hours. Traditional spectral analysis, such as FFT or STFT methods, requires that the signal desired to be analyzed is statistically stationary. The problem with the STFT is that both time and frequency resolutions of the transform are *fixed* over the entire time-frequency plane. Therefore, selecting a short analysis window may cause poor frequency resolution and on the other hand, while a long analysis window may improve

the frequency resolution, it loses the time resolution and compromises the assumptions of stationarity within the window so that the time-varying (or nonstationary) characteristic of the windowed signal is unable to be preserved. Hence, FFT-based methods sometimes may not be appropriate to physiological signal processing. Many HRV analyses, however, have been performed overwhelmingly by using these spectral estimation techniques for extracting the frequency-domain features. In order to accurately identify the changes in a variety of time scales, selecting a technique that can simultaneously gain good resolutions for both slow- (LF) and quick-changed (HF) components buried in the HR waveform so that a multiresolution signal analysis may be achieved becomes the most essential for HRV investigation.

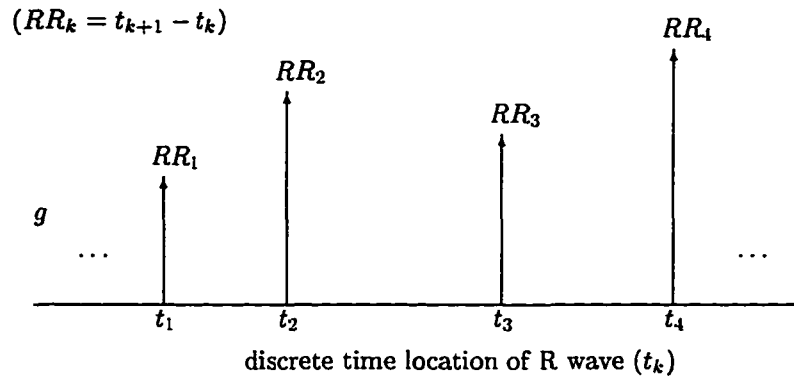
Actually, a great interest is given to the WT which, among the broad field of possible applications, allows an attractive time-frequency representation of the signal. Note that WT does not increase the information having already been present in a signal. It is just an alternate which provides a more useful representation of the signal. WT-based method serves as an excellent tool to satisfy the requirement described above since it employs analysis windows with variable size so that the trade-off effects between time and frequency resolutions may be minimized, towards the optimal time-frequency representation for signals of interest. Therefore, using such a multiresolution analysis it is possible to resolve HF components or to obtain time resolution in the same plot for better evidencing the different features of the signal simultaneously. This may permit a promising and hopeful beginning for HRV investigation. In the following, an HR data measurement and preprocessing are described first. Then, a development of potential WT-based applications to HRV analysis and

a method validation task for the new designed analysis schemes with the associated numerical experimental results are also introduced.

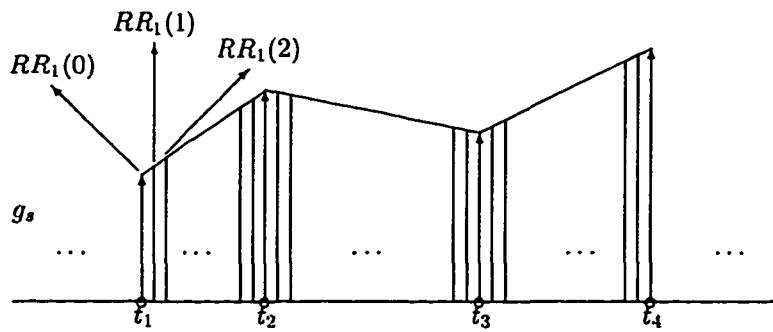
3.2 HR Data Measurement and Preprocessing

In HR data collection, correctly specifying the fiducial point on an ECG signal is the very first step. Theoretically, this point should be the onset of the P wave since it represents the start of activation of cells in the *sinoatrial* (SA) node. However, using the RR time interval as a measure of heart period is generally acceptable because the PR interval remains relatively constant if there is no conduction disorder. In fact, the measurement of RR interval is more convenient since the R wave is more easily identifiable than the P wave on the ECG tracing. Such a sequence of RR durations is usually referred to as an *RR interval tachogram* or more concisely, *tachogram*. The corresponding HR signal can be then obtained by calculating the *reciprocals* of RR intervals. Since an RR or HR signal obtained from the above process is expressed as a function of the beat number, in order to operate in the more common time scales such as second or millisecond (*e.g.*, for HRV spectral analysis) more efforts should be devoted to preprocessing the HR waveform so that it can be expressed as a function of *discrete-time* (DT) with uniform sampling period in the abscissa. The preprocessing task is mainly accomplished by *interpolating* and *resampling* the RR sequence.

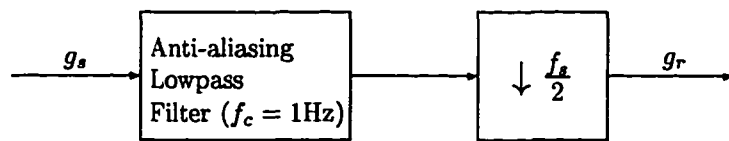
Fig. 3.1 provides schematic diagrams to interpret how to derive the RR signal and how to convert it as a DT function. The steps involved are described as follows. First, an ECG is sampled at a sufficiently high rate, f_s , to determine the time location of the R waves with a sufficient accuracy. Denoting RR_k as the RR interval corresponding



(a)



(b)



(c)

Figure 3.1: HR Measurement and preprocessing procedure.

to the k -th beat and t_k as the discrete time location of the k -th R wave, we then have

$$RR_k = t_{k+1} - t_k. \quad (3.1)$$

Observing Fig. 3.1(a), we see that for a given t_k , there is a corresponding RR_k . Note that here the magnitude of RR_k only represents number of samples between two consecutive R waves rather the actual RR interval in real time. Actually, the corresponding real-time RR interval (denoted as RRI_k) is measured by

$$RRI_k = RR_k \cdot \Delta T_s = RR_k \cdot \frac{1000}{f_s}, \quad (3.2)$$

where ΔT_s represents the sampling period with the unit of *millisecond* (ms).

Since the tachogram can be considered as an irregularly sampled waveform, by means of interpolation (*e.g.*, either linear or p -th order polynomial) a continuous signal can be thus rendered suitable for conversion to a regularly sampled waveform so that it might be further processed digitally [92]. Here, after obtaining a series of RR_k 's from an ECG signal, a linear interpolation task is performed next, as shown in Fig. 3.1(b). First, we may speculate that the RR signal g in Fig. 3.1(a) is an *envelope* of a spurious RR signal g_s that had the same sampling rate f_s as the original ECG signal. Considering any pair of two consecutive RR intervals in g , say RR_k and RR_{k+1} , it can be readily inferred that there should exist $(t_{k+1} - t_k + 1)$ samples, including RR_k and RR_{k+1} , between these two RR intervals in g_s . Denoting the n -th RR samples between RR_k and RR_{k+1} as $RR_k(n)$, using linear interpolation $RR_k(n)$ is then estimated as

$$RR_k(n) = RR_k + n \cdot \frac{RR_{k+1} - RR_k}{t_{k+1} - t_k}, \quad \text{for } n = 0, 1, \dots, (t_{k+1} - t_k), \quad (3.3)$$

or equivalently (using Eq. 3.1),

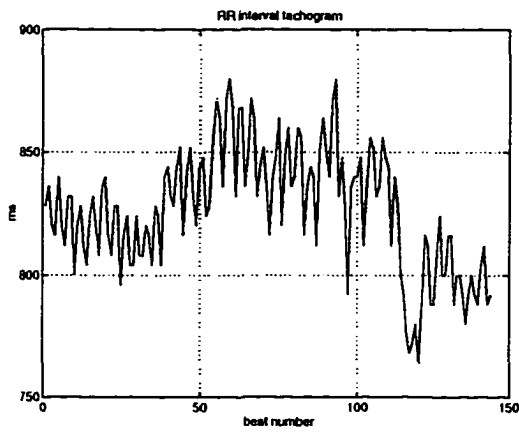
$$RR_k(n) = RR_k + n \cdot \frac{RR_{k+1} - RR_k}{RR_k}, \quad \text{for } n = 0, 1, \dots, RR_k. \quad (3.4)$$

Obviously, we have $RR_k(0) = RR_k$ and $RR_k(RR_k) = RR_{k+1}$. Observing Fig. 3.1(b), we see that after interpolating all the adjacent RR interval pairs an estimated RR waveform with uniform sampling period in time domain is then constructed.

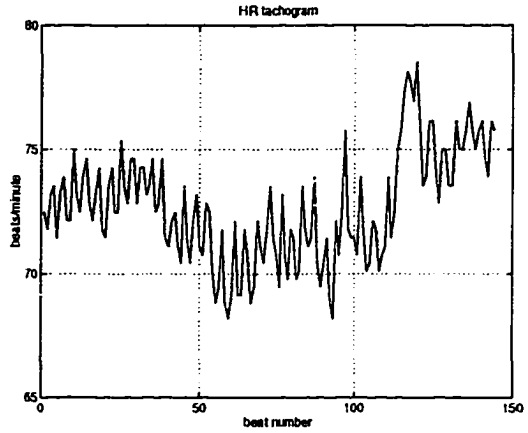
The final step involved in the data preprocessing task is to resample the interpolated RR waveform, as shown in Fig. 3.1(c). In general, the frequency components of interest for HRV analysis is usually less than 1 Hz [56], therefore according to the Nyquist sampling theorem we here choose the resampling rate as 2 Hz (*i.e.*, decimated by a factor of $\frac{f_s}{2}$) so that all frequency components below 1 Hz can be thus preserved. Also, to prevent the aliasing effect due to downsampling, a lowpass filter, referred to as the *anti-aliasing filter*, with cutoff frequency $f_c = 1$ Hz is introduced before the decimation stage. As a result, a resampled RR signal g_r with a uniform sampling period (0.5 second) in time domain is then obtained. Similarly, the corresponding resampled HR signal can be measured by calculating the reciprocals of the resampled RR signal. Fig. 3.2 gives illustrations of an original RR, HR tachograms and the corresponding resampled signals, respectively. These resampled signals thus provide a desired form used for HRV analysis.

3.3 Design of WT-based Analysis Schemes

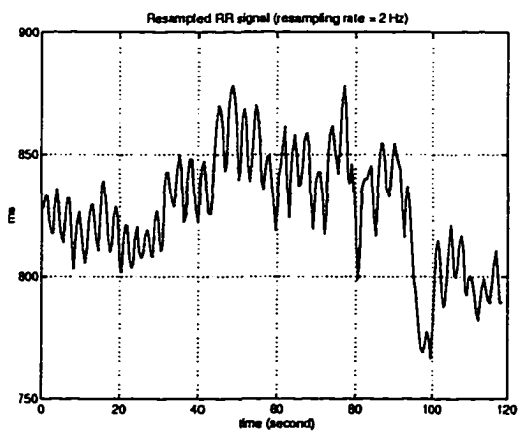
A description of WT-based analysis scheme design is presented in this section. Before developing the algorithms, we first calculated FWT for the two resampled RR signals obtained from a subject under supine and tilt maneuvers, respectively, and examine how temporal representations of the LF and HF components behave during both position states. For this purpose, after obtaining the WT coefficients for both RR signals two illustrations for supine and tilt stimulations were constructed and



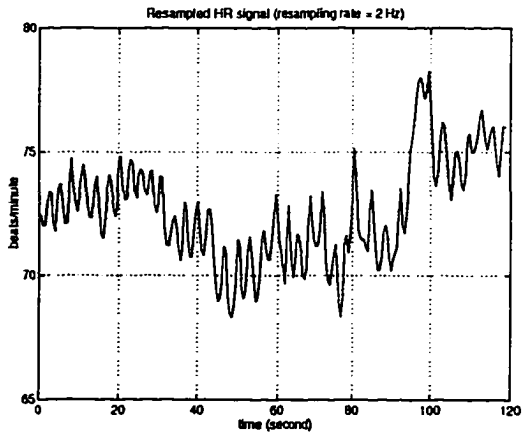
(a)



(b)



(c)



(d)

Figure 3.2: Illustrations of RR and HR signals: (a) an RR interval tachogram; (b) an HR tachogram; (c) the corresponding resampled RR signal; (d) the corresponding resampled HR signal.

shown in Figs. 3.3 and 3.4, respectively. Note that in both illustrations each one of them consisted of the resampled RR waveform and the corresponding composite detail signals at all levels. Observing these figures closely, it appeared that in Fig. 3.3 the oscillations in the HF bands (*i.e.*, ≥ 0.15 Hz), such as $[0.125, 0.25]$ Hz ($j = -3$) and $[0.25, 0.5]$ Hz ($j = -2$), were more clearly monitored with *larger* amplitudes and at the same time, those in the LF band ranged from 0.03125 Hz to 0.0625 Hz ($j = -5$) seemed more suppressive, in comparison with the same frequency locations in Fig. 3.4. The basis functions we adopted here and throughout this dissertation were the Daubechies orthonormal wavelets generated by both scaling filter $h(n)$ and wavelet filter $g(n)$ with 8 filter coefficients. Fig. 3.5 shows the estimates of the corresponding scaling function $\phi(t)$ and wavelet function $\psi(t)$.

According to the previously researches [56, 69, 96], it has been confirmed that LF components (usually below 0.1 Hz) of HRV spectrum should correspond to a mediated activity of sympathetic and vagal nerves while HF components (usually above 0.15 Hz) solely correspond to vagal response, mainly due to respiratory activity. Therefore, it can be seen that the preliminary wavelet analysis results presented by both Figs. 3.3 and 3.4 are accordingly consistent to the fact of physiological events, *i.e.*, an increase of the sympathetic activity (LF components) and a decrease of the vagal activity (HF components) when changing from supine to tilt.

Since there exists an antagonist relation between LF and HF powers, the power ratio $r = \text{LF}/\text{HF}$ can be thus visualized as an index used to quantify the ANS or sympathovagal balance. Actually, to further study how ANS influences on the HRV, particularly during a very short time interval, we must be very careful in estimating the short-time spectral powers to guarantee that LF/HF can be measured in the

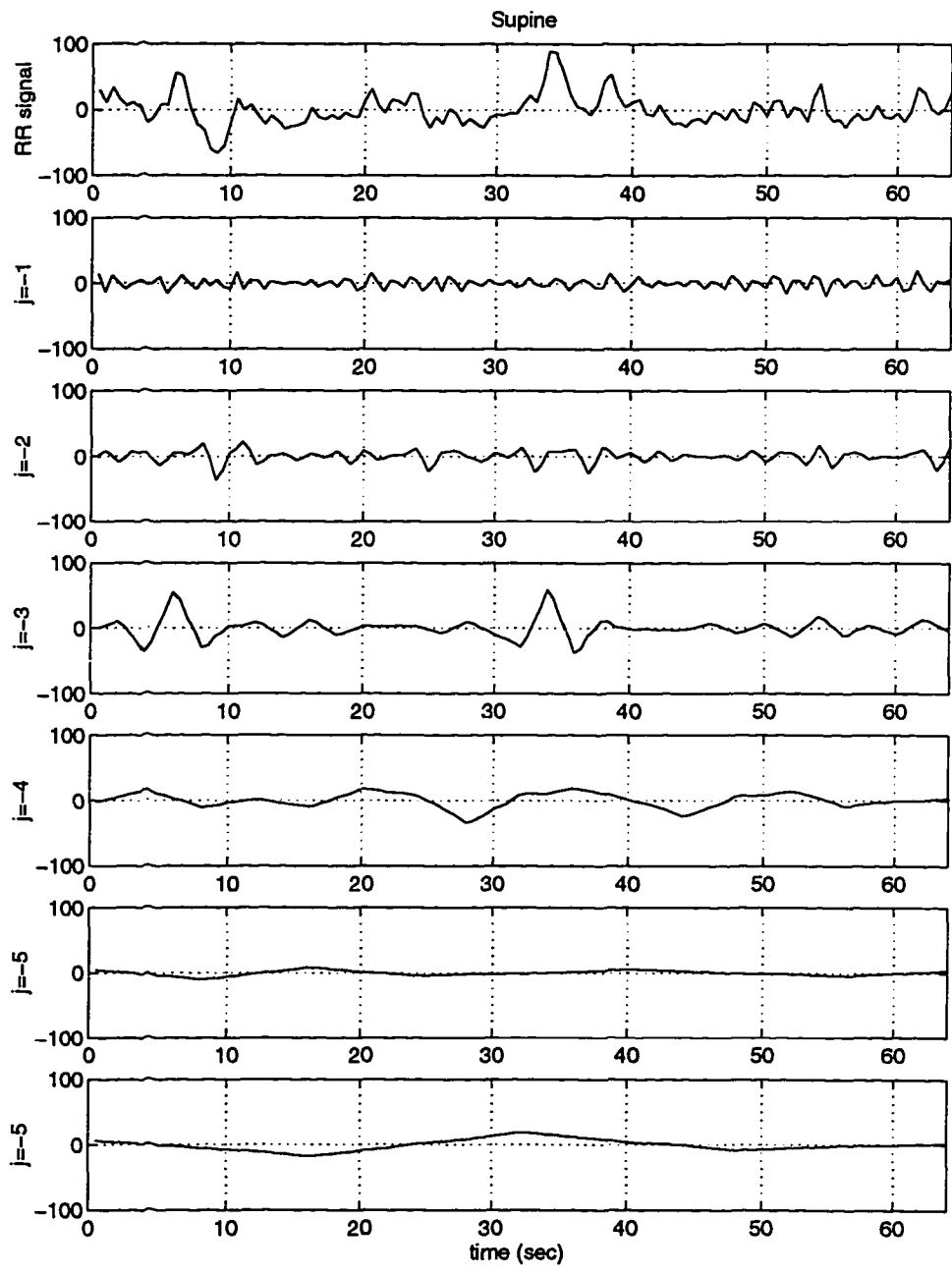


Figure 3.3: WT-based multiresolution representation of the RR signal for a subject at supine position. Top panel– normalized RR signal; the second to the sixth panels (from the top)– composite detail signals with corresponding scaling levels: 2^{-1} to 2^{-5} (i.e., in subspaces W_{-1} to W_{-5}), respectively; bottom panel– composite coarse signal at level 2^{-5} (V_{-5}).

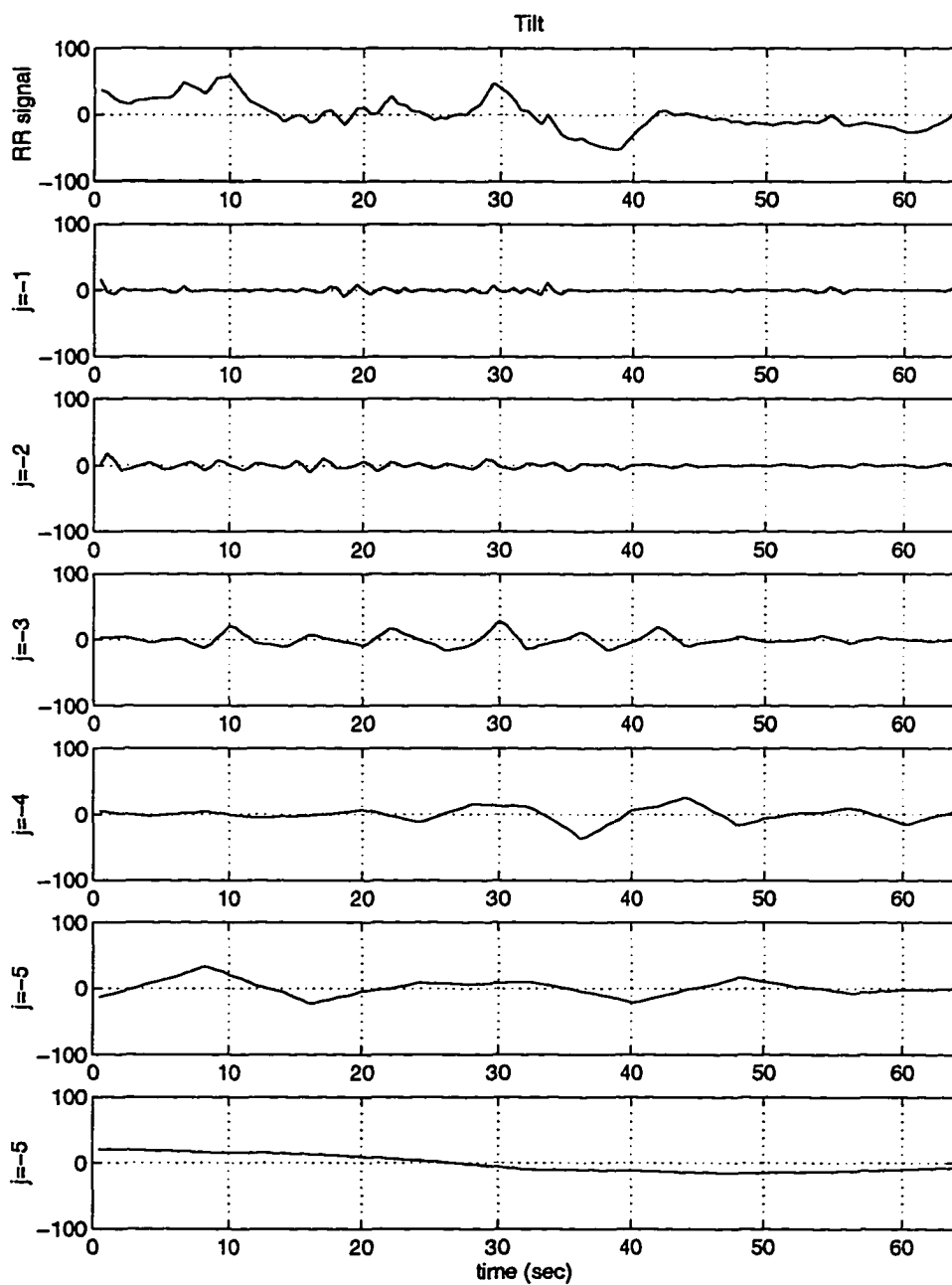


Figure 3.4: WT-based multiresolution representation of the RR signal for a subject at tilt position. Top panel– normalized RR signal; the second to the sixth panels (from the top)– composite detail signals with corresponding scaling levels: 2^{-1} to 2^{-5} (i.e., in subspaces W_{-1} to W_{-5}), respectively; bottom panel– composite coarse signal at level 2^{-5} (V_{-5}).

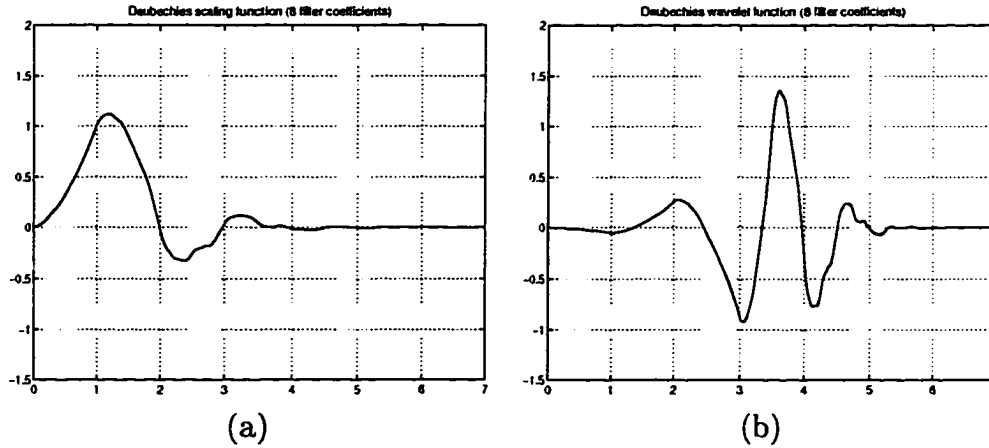


Figure 3.5: (a) scaling function $\phi(t)$; (b) wavelet function $\psi(t)$. Both are estimated by Daubechies wavelet system filters $h(n)$ and $g(n)$ with 8 filter coefficients (successive approximation).

most appropriate and efficient manner so an accurate instantaneous autonomic (or sympathovagal) balance status estimation may be then attained. Fortunately, wavelet analysis may do this. Two algorithms based on WT application for short-time HRV analysis will be presented in the following sections.

3.3.1 Analysis Scheme 1

In order to perform a short-time HRV analysis,² we may calculate power (or energy) ratios on windowed RR signals simply by employing the *segmental* WT coefficients since these coefficients carry the signal information. A scheme is designed as follows. First, we set the window length to T seconds and let T be *fixed* throughout all scaling levels. Fig. 3.6 provides a schematic plot of the coverage in the time-frequency plane for wavelet analysis. In this figure, the thick-line blocks represent the windowed

²Note that throughout this dissertation the “short-time HRV” is quantified via the instantaneous sympathovagal balance states.

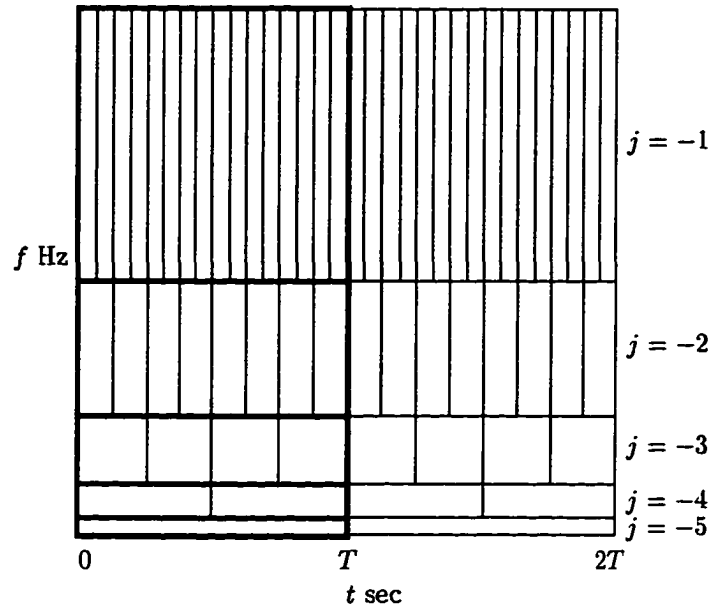


Figure 3.6: Time-frequency tiles and coverage of the time-frequency plane for wavelet analysis (thick-line blocks represent windowed regions that occupy the same real time interval T ; also, each thin-line block has the same number of WT coefficients).

regions at all levels sharing the same real time interval T . Also, each thin-line block has the same number of WT coefficients. In general, the higher the level is, the more the number of WT coefficients are contained by a thick-line block. Specifically, suppose that this T -second window comprises N WT coefficients at level 2^j , it can be readily inferred that this T -second window would comprise $N \cdot 2^k$ WT coefficients at level $2^{(j+k)}$ as well.

Now a short-time spectral power calculation can be performed as follows. Given an RR tachogram we first convert it into a uniformly-sampled RR signal by using the techniques described in Section 3.2 and then, calculate the FWT for this resampled

RR signal. After that, either the value of real-time window length T or, more conveniently, the total number of windows for analysis needs to be determined. Once the FWT has been computed and the total number of windows for analysis, denoted as N_{win} , is determined, the WT coefficients at each level is then *equally* divided into N_{win} groups. To clearly express this short-time spectral power calculation scheme in mathematical form, a number of useful denotations are defined here. Letting N_j represent the total number of WT coefficients at level 2^j and assuming that there are L levels in FWT analysis, the *composite* detail signal in real time domain at level 2^j can be expressed by

$$D_j(t) = \sum_{k=0}^{N_j-1} d_j(k)\psi_{j,k}(t), \quad \text{for } j = -1, \dots, -L, \quad (3.5)$$

where $D_j(t)$ is a continuous-time signal. Since our analysis is actually based on a discrete-time RR signal processing, $D_j(t)$ should be further sampled by a sufficiently fast sampling period T_s as³

$$D_j(nT_s) = \sum_{k=0}^{N_j-1} d_j(k)\psi_{j,k}(nT_s), \quad \text{for } j = -1, \dots, -L. \quad (3.6)$$

$D_j(nT_s)$ thus represents the discrete-time signal components corresponding to the dyadic frequency bands $[2^j\pi/T_s, 2^{j+1}\pi/T_s]$. Also, for each window at level 2^j we here assume that there are N'_j WT coefficients and $N'_j = N_j/N_{win}$. Since it has been noted that the quantitative information of the sympathetic- and vagal-mediated activities are reflected by the LF and HF powers, respectively, using the denotations defined above the autonomic balance state corresponding to the i -th window can be measured

³Note that in order to avoid aliasing effects due to sampling process, T_s needs to meet the Nyquist criterion that $T_s \leq \pi/\Omega_{RR}$, where Ω_{RR} is the bandlimit of the continuous-time RR signal. Here, T_s is identical to the resampling period of the original RR signal, *i.e.*, $T_s = 1/f_s$.

by the form as

$$\begin{aligned}
r_i &= \frac{\sum_{j=\text{LF}} \|D_j(nT_s)\|^2}{\sum_{j=\text{HF}} \|D_j(nT_s)\|^2} \quad (\text{for } (i-1)T \leq nT_s < iT) \\
&= \frac{\sum_{j=\text{LF}} \sum_{k=(i-1)N'_j}^{iN'_j-1} d_j^2(k) \|\psi_{j,k}(nT_s)\|^2}{\sum_{j=\text{HF}} \sum_{k=(i-1)N'_j}^{iN'_j-1} d_j^2(k) \|\psi_{j,k}(nT_s)\|^2} \\
&= \frac{\sum_{j=\text{LF}} \sum_{k=(i-1)N'_j}^{iN'_j-1} d_j^2(k)}{\sum_{j=\text{HF}} \sum_{k=(i-1)N'_j}^{iN'_j-1} d_j^2(k)}, \quad \text{for } i = 1, \dots, N_{win}. \quad (3.7)
\end{aligned}$$

r_i thus provides an insight into autonomic balance status over the i -th short-time window. Such an instantaneous autonomic balance of the heart period signal is thus monitored by a T -second time frame. Since r_i is a time-varying quantity, $\mathbf{r} = \{r_i\}_{i=1}^{N_{win}}$ would represent a vector consisting of the estimates of autonomic balance status versus time evolution. As a result, the investigation of the autonomic dynamics can be simply achieved by \mathbf{r} .

An example for demonstration is described as follow. In this example, each one of the resampled RR signals given by Figs. 3.3 and 3.4 was 64 seconds (≈ 1 minute) in length, the resampling frequency $f_s = 2$ Hz (this yields 128 samples), the time interval of a window for short-time analysis $T = 32$ seconds and the number of FWT analysis levels $L = 5$. This allows the number of the analysis windows $N_{win} = 2$ and each window readily comprises $N'_{-1} = 32$, $N'_{-2} = 16$, $N'_{-3} = 8$, $N'_{-4} = 4$ and $N'_{-5} = 2$ WT coefficients at levels 2^{-1} , 2^{-2} , 2^{-3} , 2^{-4} and 2^{-5} , respectively. Considering Fig. 3.6. we may see that each thin-line block in this figure would contain 2 WT coefficients throughout all levels. In addition, the frequency allocations are listed as follows:

j	corresponding frequency band
-1	0.5–1 Hz
-2	0.25–0.5 Hz
-3	0.125–0.25 Hz
-4	0.0625–0.125 Hz
-5	0.03125–0.0625 Hz

We here chose [0.03125,0.0625] Hz as LF and [0.125,0.5] Hz as HF bands in the demonstrated example. Using Eq. 3.7, r_i is then calculated by

$$r_i = \frac{\sum_{j=-5} \sum_{k=(i-1)N_j}^{iN_j-1} d_j^2(k)}{\sum_{j=-2,-3} \sum_{k=(i-1)N_j}^{iN_j-1} d_j^2(k)}, \quad \text{for } i = 1, 2. \quad (3.8)$$

Obviously, Eq. 3.8 will result in two power ratio values as r_1 and r_2 , which *approximately* indicate the autonomic balance states during 0–32 seconds and 32–64 seconds, respectively. Note that in this scheme, the last power ratio value should be the least accurate. This is because a number of zeros were padded after the ending point EP (here $EP = 128$) and such a *zero-padding* process obviously would result in inaccurate estimates of WT coefficients, throughout all levels, associated with the signal monitored by the last window. Therefore, in this example we thus only adopted the first power ratio value, r_1 , for performance evaluation.

Applying the WT-based method to both the RR signals given in Figs. 3.3 and 3.4, consequently, we obtained $r_1^{(\text{tilt})} \doteq 0.7409$ and $r_1^{(\text{supine})} \doteq 0.0314$. That is, the power ratio within a very short period (\approx half a minute) obtained from tilt appeared to be *larger* than that obtained from supine, indicating that the *sympathetic activity might dominate in ANS function as the patient is at tilt position*. This is actually consistent to the fact of physiological events.

The WT-based analysis scheme introduced here seems to give a hopeful start. We would further test this analysis scheme on a patient group in Section 3.4 to see if similar promising observations can hold for the more subjects, towards a method

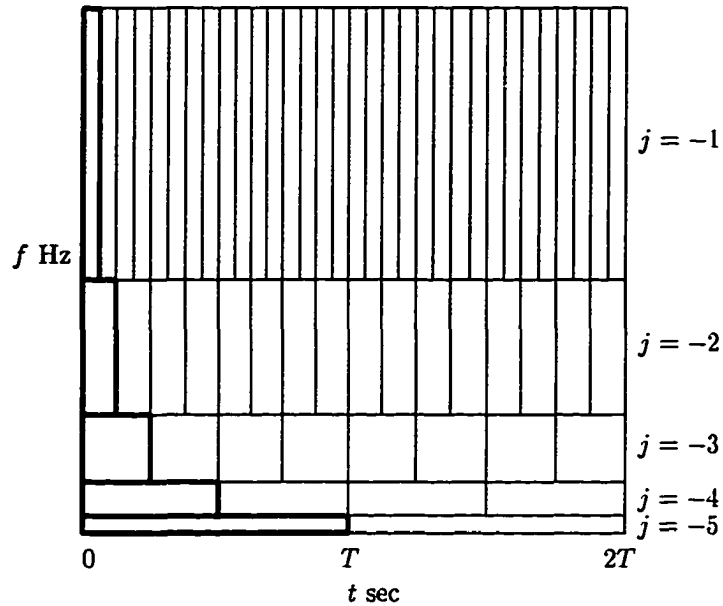


Figure 3.7: Time-frequency tiles and coverage of the time-frequency plane for wavelet analysis (thick-line blocks represent the windowed regions that have the same number of WT coefficients).

validation. Also, a comparison between the results obtained by applying both the WT-based and the traditional STFT methods will be presented.

3.3.2 Analysis Scheme 2

Considering the analysis scheme 1, since the short-time analysis was performed over a fixed T-second period throughout all levels (*e.g.*, LF and HF power calculations), the tile-structure of time-frequency representation contributed by a variable frequency resolution for the WT method was thus ignored. In this section, a better WT-based scheme adequately employing such a unique time-frequency structure will be introduced. Unlike the analysis scheme 1, the one presented in the following may provide more efficient measures of the instantaneous autonomic balance states.

Fig. 3.7 gives the schematic diagram of this new application. First, it should be noted that here the criterion used for window selection is *different* from that used in scheme 1. Instead of selecting the same number of windows throughout all levels by using a fixed real-time period T as the window length in scheme 1, we here adopt a fixed number of WT coefficients, M , as the window length for window selection at all levels so that the number of windows might vary in different levels. In Fig. 3.7, each thick-line block thus indicates a window selected from each level. According to this different window selection criterion, it can be readily inferred that if there are N windows at level 2^j occupying a certain time interval, then the same time interval would also comprise $N \cdot 2^k$ windows at level $2^{(j+k)}$.

Similarly, we first calculate the FWT for a uniformly-sampled RR signal. Once the FWT has been computed and the window length M is determined, the total number of windows at each level, denoted as $N_{win}^{(j)}$, is thus determined by N_j/M , where N_j represents the total number of WT coefficients at level 2^j . The short-time spectral power calculation is then performed on these windows. In other words, each window containing M WT coefficients serves as a *power calculation unit* (PCU). After obtaining power estimates from all PCU's, the instantaneous autonomic balance states can be then measured simply by finding the LF to HF power ratios. This process will be illustrated by an existing example as follows.

Still, the RR signals used in this illustrative example are given by Figs. 3.3 and 3.4. As described in Section 3.3.1, it has been known that the resampled RR signal was 64 seconds in length, the resampling frequency $f_s = 2$ Hz and the number of FWT analysis levels $L = 5$. Choosing the window length as $M = 4$ here, it thus readily resulted in the numbers of the analysis windows $N_{win}^{(-1)} = 16$, $N_{win}^{(-2)} = 8$, $N_{win}^{(-3)} = 4$,

$N_{win}^{(-4)} = 2$ and $N_{win}^{(-5)} = 1$ at levels 2^{-1} , 2^{-2} , 2^{-3} , 2^{-4} and 2^{-5} , respectively. Also, denoting the real time interval occupied by a window at level 2^j as ΔT_j (unit: seconds), we then have $\Delta T_{-1} = 4$, $\Delta T_{-2} = 8$, $\Delta T_{-3} = 16$, $\Delta T_{-4} = 32$ and $\Delta T_{-5} = 64$. The time-frequency tile structure of this illustrative example is provided in Fig. 3.8. Each tile in Fig. 3.8 represents a window in time-frequency plane and contains 4 WT coefficients throughout all levels. Now, considering the structure shown in this figure, we may see that the higher the level is, the faster the window moves. In this example, since we chose, as previously, $j = -5$ as LF (*i.e.*, [0.03125,0.0625] Hz) and $j = -2, -3$ as HF (*i.e.*, [0.125,0.5] Hz), it can be concluded that a window at level 2^{-5} would share the same time interval as that spanned by four windows at level 2^{-3} with proper time location and similarly, by eight windows at level 2^{-2} . Denote i as the enumerative number for windows at level 2^{-5} , l as the enumerative number for windows at level 2^{-3} and m as the enumerative number for windows at level 2^{-2} . Using (i, l, m) to describe the temporal locations of the short-time windows at these three levels, in this example the window movement can be expressed by a sequential representation of (i, l, m) as

$$(1, 1, 1) \rightarrow (1, 1, 2) \rightarrow (1, 2, 3) \rightarrow (1, 2, 4) \rightarrow (1, 3, 5) \rightarrow (1, 3, 6) \rightarrow (1, 4, 7) \rightarrow (1, 4, 8).$$

Therefore, the short-time power ratio calculation is performed according to this sequential order. Denoting the instantaneous power ratio as $r_{i,l,m}$ and recalling LF=[0.03125,0.0625] Hz and HF=[0.125,0.5] Hz in the illustrative example, $r_{i,l,m}$ is thus measured by

$$\begin{aligned}
r_{i,l,m} &= \frac{\frac{1}{\Delta T_{-5}} \sum_{k=(i-1)M}^{iM-1} d_{-5}^2(k)}{\frac{1}{\Delta T_{-3}} \sum_{k=(l-1)M}^{lM-1} d_{-3}^2(k) + \frac{1}{\Delta T_{-2}} \sum_{k=(m-1)M}^{mM-1} d_{-2}^2(k)} \\
&= \frac{\frac{1}{64} \sum_{k=(i-1)M}^{iM-1} d_{-5}^2(k)}{\frac{1}{16} \sum_{k=(l-1)M}^{lM-1} d_{-3}^2(k) + \frac{1}{8} \sum_{k=(m-1)M}^{mM-1} d_{-2}^2(k)}
\end{aligned}$$

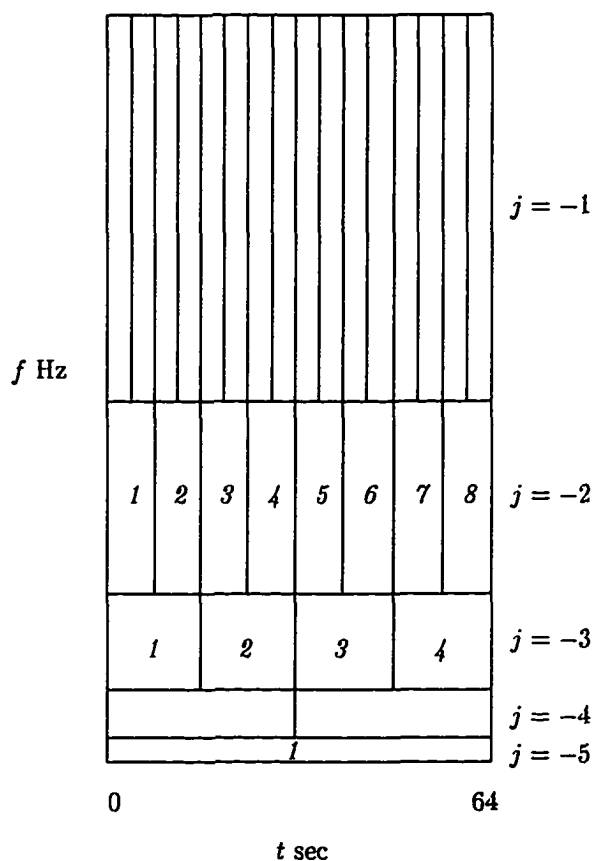


Figure 3.8: An illustration for the demonstrative example in Section 3.3.2. Note that each tile (or window) contains M WT coefficients ($M = 4$); power calculation is then performed on each one of these windows. In addition, the enumerative numbers (in italic style) for the windows at the levels of interest ($j = -2, -3, -5$) are also included. To describe the window movement, a sequential representation of (i, l, m) is thus expressed as: $(1, 1, 1) \rightarrow (1, 1, 2) \rightarrow (1, 2, 3) \rightarrow (1, 2, 4) \rightarrow (1, 3, 5) \rightarrow (1, 3, 6) \rightarrow (1, 4, 7) \rightarrow (1, 4, 8)$.

$$= \frac{\sum_{k=(i-1)M}^{iM-1} d_{-5}^2(k)}{4 \cdot \sum_{k=(l-1)M}^{lM-1} d_{-3}^2(k) + 8 \cdot \sum_{k=(m-1)M}^{mM-1} d_{-2}^2(k)}, \quad (M = 4) \quad (3.9)$$

where $(i, l, m) = (1, 1, 1), (1, 1, 2), (1, 2, 3), (1, 2, 4), (1, 3, 5), (1, 3, 6), (1, 4, 7), (1, 4, 8)$.

Consequently, Eq. 3.9 will result in eight power ratio values as $r_{1,1,1}, r_{1,1,2}, r_{1,2,3}, r_{1,2,4}, r_{1,3,5}, r_{1,3,6}, r_{1,4,7}$ and $r_{1,4,8}$, which *approximately* indicate the autonomic balance states during 0–8, 8–16, 16–24, 24–32, 32–40, 40–48, 48–56 and 56–64 seconds, respectively. Obviously, the scheme 2 can provide measure of the power ratio over a much shorter time period than the scheme 1 so that the instantaneous autonomic balance states can be monitored in a much faster time frame. Also, due to the characteristic of a variable time size in LF and HF windows for WT method, it can be expected that this novel scheme should work much better than the STFT method because the WT-based method allows a more efficient arrangement of time and frequency resolutions so that the temporal-spectral information associated with the RR signals might be maximally utilized. Figs. 3.9 and 3.10 show the power ratio plots obtained by applying this scheme and STFT method, respectively, to the RR signals recorded during supine and tilt stimulations for a subject. Observing both figures we may see that while the STFT-based power ratios failed to discriminate the supine and tilt maneuvers, the WT-based results indicated a clear and complete separation between these two position states for the subject.

In this comparison the short-time (≈ 8 seconds) power ratios obtained from tilt appeared to be generally larger than those obtained from supine and, again, indicated the fact of physiological events that the sympathetic activity might dominate in ANS function as the patient is at tilt position. Similarly, we would further test this analysis scheme on a patient group in Section 3.4 to see if similar promising observations can hold for the more subjects, towards a method validation task. Also, a comparison

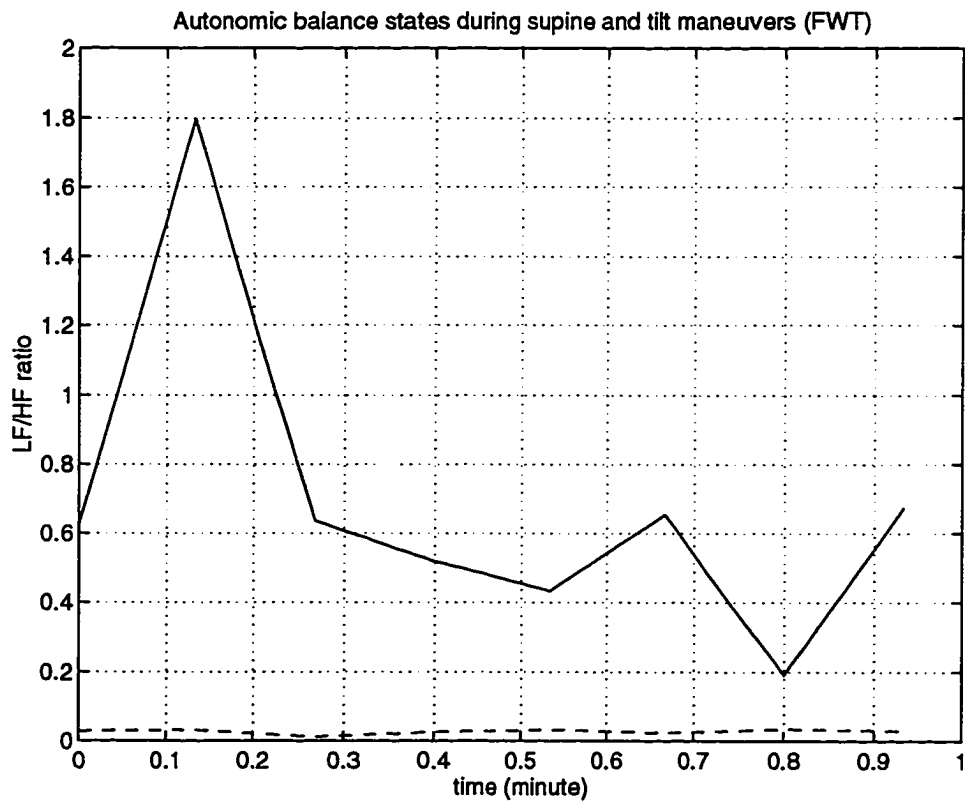


Figure 3.9: The instantaneous autonomic balance states during supine (dash line) and tilt (solid line) maneuvers obtained by the proposed WT-based scheme 2.

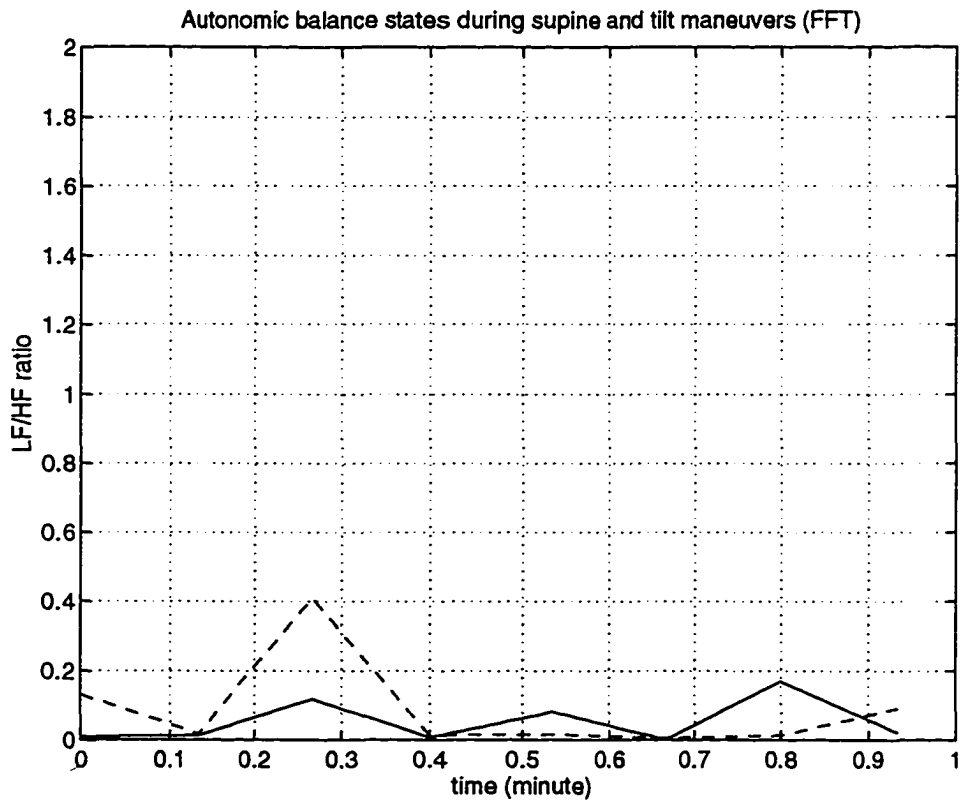


Figure 3.10: The instantaneous autonomic balance states during supine (dash line) and tilt (solid line) maneuvers obtained by the traditional STFT method.

between the results obtained by applying both this WT-based and the traditional STFT methods will be presented.

3.4 Validation Experiments

Before further applying the WT-based analysis schemes introduced in Sections 3.3.1 and 3.3.2 to HRV assessment, a simple numerical experiment for method validation was performed. Such a validation task was initiated by a cardiac autonomic stimulation trial (*i.e.*, supine-tilt maneuvers). We here included a small patient group, consisting of eight healthy adults, that had undergone a simple physical experiment. Using the Holter tape recorder, an RR recording associated with each subject in this group was measured. Each RR recording consists of two episodes and both episodes were measured during supine and tilt maneuvers, respectively, for each subject. Each episode was only approximate 1-minute (64 seconds) in length. HRV examinations were performed on the group using the two WT-based schemes described previously and STFT methods, respectively. A method validation can be then achieved simply by evaluating and comparing the numerical results obtained from both the WT- and STFT-based methods. The details are described in the following sections.

3.4.1 STFT Analysis

For STFT analysis, we here divided the RR signal into K windows so that each RR episode comprises K power ratio values. That is, each window contains $N' = 128/K$ points. Denote the i -th windowed signal as $RR_i(n)$, where

$$\begin{aligned}
 RR_i(n) &= RR((i-1)N' + n), & \text{for } 0 \leq n \leq N' - 1 \\
 &0, & \text{otherwise.}
 \end{aligned} \tag{3.10}$$

Here we used the periodogram spectral estimator [57], known as a Fourier-based method, to estimate the *power spectral density* (PSD), that is,

$$S_{per}(f) = \frac{1}{N'} \left| \sum_{n=0}^{N'-1} RR_i(n) e^{-j2\pi f n} \right|^2, \quad (3.11)$$

where f represents the *fundamental frequency* (or *Nyquist frequency*).

Similarly, we chose the same LF and HF locations as before: LF=[0.03125,0.0625] Hz and HF=[0.125,0.5] Hz. To digitally process the data, we first converted these frequencies to their corresponding fundamental frequencies simply by dividing them by f_s (here $f_s = 2$)

$$f_{l1} = \frac{0.03125}{2}, \quad f_{l2} = \frac{0.0625}{2}, \quad f_{h1} = \frac{0.125}{2}, \quad f_{h2} = \frac{0.5}{2}.$$

Denoting the i -th estimated PSD and the corresponding LF-to-HF power ratio as $S_{per}^{(i)}(f)$ and $r_i^{(FT)}$, respectively, $r_i^{(FT)}$ is then expressed by

$$\begin{aligned} r_i^{(FT)} &= \frac{\int_{f_{l1}}^{f_{l2}} S_{per}^{(i)}(f) df}{\int_{f_{h1}}^{f_{h2}} S_{per}^{(i)}(f) df} \\ &= \frac{\int_{f_{l1}}^{f_{l2}} \frac{1}{N'} \left| \sum_{n=0}^{N'-1} RR_i(n) e^{-j2\pi f n} \right|^2 df}{\int_{f_{h1}}^{f_{h2}} \frac{1}{N'} \left| \sum_{n=0}^{N'-1} RR_i(n) e^{-j2\pi f n} \right|^2 df}, \quad \text{for } i = 1, \dots, K. \end{aligned} \quad (3.12)$$

Since $S_{per}^{(i)}(f)$ cannot be computed for a continuum of frequencies, we are forced to sample it. In general, equally spaced frequency samples are taken so that $f_k = k/N'$ for $k = 0, 1, \dots, N' - 1$ to yield

$$\begin{aligned} S_{per}(f_k) &= \frac{1}{N'} \left| \sum_{n=0}^{N'-1} RR_i(n) e^{-j2\pi f_k n} \right|^2 \\ &= \frac{1}{N'} \left| \sum_{n=0}^{N'-1} RR_i(n) e^{-j\frac{2\pi k}{N'} n} \right|^2, \quad k = 0, 1, \dots, N' - 1. \end{aligned} \quad (3.13)$$

The latter expression is in the form of a DFT and hence may be efficiently computed using an FFT. To approximate $S_{per}^{(i)}(f)$ more closely, we may need to have a finer

frequency spacing. This is accomplished by zero padding the data with $N_p - N'$ zeros and then taking an N_p point FFT. Let $f'_k = k/N_p$ and the frequency spacing Δf will then be $1/N_p < 1/N'$. As a result, Eq. 3.13 becomes

$$\begin{aligned} S_{per}(f'_k) &= \frac{1}{N'} \left| \sum_{n=0}^{N'-1} RR_i(n) e^{-j2\pi f'_k n} \right|^2 \\ &= \frac{1}{N'} \left| \sum_{n=0}^{N_p-1} RR'_i(n) e^{-j\frac{2\pi k}{N_p} n} \right|^2, \quad k = 0, 1, \dots, N_p - 1, \end{aligned} \quad (3.14)$$

where

$$RR'_i(n) = RR_i(n), \quad \text{for } 0 \leq n \leq N' - 1 \quad (3.15)$$

$$0, \quad \text{for } N' \leq n \leq N_p - 1. \quad (3.16)$$

$r_i^{(\text{FT})}$ in Eq. 3.12 is thus approximated by $r_i^{(\text{FFT})}$ in the form as

$$\begin{aligned} r_i^{(\text{FFT})} &= \frac{\sum_{f_{l1} \leq f'_k \leq f_{l2}} \frac{1}{N'} \left| \sum_{n=0}^{N'-1} RR_i(n) e^{-j\frac{2\pi k}{N_p} n} \right|^2 \Delta f}{\sum_{f_{h1} \leq f'_k \leq f_{h2}} \frac{1}{N'} \left| \sum_{n=0}^{N'-1} RR_i(n) e^{-j\frac{2\pi k}{N_p} n} \right|^2 \Delta f} \\ &= \frac{\sum_{N_p f_{l1} \leq k \leq N_p f_{l2}} \left| \sum_{n=0}^{N'-1} RR_i(n) e^{-j\frac{2\pi k}{N_p} n} \right|^2}{\sum_{N_p f_{h1} \leq k \leq N_p f_{h2}} \left| \sum_{n=0}^{N'-1} RR_i(n) e^{-j\frac{2\pi k}{N_p} n} \right|^2}, \quad \text{for } i = 1, \dots, K. \end{aligned} \quad (3.17)$$

$r_i^{(\text{FFT})}$ in Eq. 3.17 thus provides an STFT-based estimate of autonomic balance status over the i -th short-time window.

Note that this method was performed based on the assumption of stationary data. Actually, the choice of the STFT method is imposed by the need to obtain a good compromise between a sufficient frequency resolution that may be achieved with long data records and the stationarity condition of the signal which is required for a reliable spectral estimation. This cannot be maintained for a long time, especially on biological signals. In the following, performance evaluations for both the WT-based schemes described in Sections 3.3.1 and 3.3.2 will be achieved by comparing

the numerical results with those obtained from STFT method, as well as with the fact in physiology, towards a method validation for both WT-based schemes.

3.4.2 Method Validation for Analysis Scheme 1

Denote the power ratio obtained by analysis scheme 1 as $r_i^{(\text{FWT1})}$ first. According to the given demonstrative example in Section 3.3.1, we know that $r_i^{(\text{FWT1})}$ was derived under the condition of $N_{win} = 2$. In order to compare the performance of the scheme 1 with that of STFT method, we here performed the STFT method on the same RR data by also setting number of windows $K = 2$ (*i.e.*, window length $N' = 64$ samples) for each RR episode. Using Eq. 3.17, we then obtained $r_i^{(\text{FFT})}$, for $i = 1, 2$. These $r_i^{(\text{FFT})}$ values hence represented the STFT-based autonomic balance state estimates. The performance evaluation here was mainly focused on the ability in accurately estimating power ratio over a very short window for both WT- and STFT-based methods. As described before, for WT-based method the WT coefficients obtained from the last one window region are usually less accurate than the remainings, therefore we here included all but the last one power ratios in performance evaluation task for both methods. Since in this demonstrative example there were only two windows, we thus observed the first power ratio values, $r_1^{(\text{FWT1})}$ and $r_1^{(\text{FFT})}$, to see how well they can accordingly meet the expected physiological observation, that is, the power ratio over a short window of the RR signal recorded from tilt is *larger* than that from supine.

In this trial, we obtained two power ratio estimates for each one of the eight subjects corresponding to tilt and supine maneuvers, respectively. All the numerical results obtained from both the WT-based analysis scheme 1 and the STFT-based

subject no.	tilt	supine
1	0.7409	0.0314
2	2.6674	0.3588
3	0.6430	0.1377
4	1.2780	0.0113
5	0.5478	0.2021
6	1.3766	0.0532
7	1.8309	0.8900
8	0.2490	0.0604

Table 3.1: $\tau_1^{(\text{FWT1})}$ obtained from the eight subjects during tilt and supine.

subject no.	tilt	supine
1	1.2284	0.3044
2	1.3927	0.7714
3	0.4497	0.3911
4	0.1800	0.4974
5	2.0208	0.1682
6	0.5998	0.1309
7	0.2090	0.6371
8	0.7744	0.3604

Table 3.2: $\tau_1^{(\text{FFT})}$ obtained from the eight subjects during tilt and supine.

method were listed in Tables 3.1 and 3.2. We also presented these results by using bar diagrams as shown in Figs. 3.11 and 3.12. Both plots show the power ratios ($r_1^{(\text{FWT1})}$ and $r_1^{(\text{FFT})}$) obtained by applying WT- and STFT-based analyses, respectively, for the eight subjects under the two different position states. Consequently, we see, from Fig. 3.12, that while two out of eight subjects (subjects 4 and 7) appeared to be identified as wrong positions by FFT analysis, Fig. 3.11 shows that the positions of all eight subjects had been successfully detected. This indicated that the application of wavelet analysis not only was able to resolve the differences between the RR signals recorded from tilt and supine positions, but also worked a bit better (100% detection accuracy) than did the STFT-based method (only 75% detection accuracy), especially on short-time analysis.

According to the above results, it might tell us that the wavelet package could provide a useful tool in many aspects of HRV analysis in future. In fact, the most interesting dissimilarity between Fourier and wavelet transforms is that individual wavelet functions are *localized in space* but Fourier sinusoidal functions are not. Thus, we can see that such an excellent performance from WT-based method should be due to its *compactly supported characteristic*. The nonstationarity of the RR signal, either buried in LF or HF bands, can be preserved and then stored in WT coefficients until the ending point of the entire signal. Since WT coefficients carry the information of RR waveforms in a variety of bands, the spectral power estimation over a very short window can be thus performed simply using the segmental WT coefficients so that the autonomic balance state over a short window may be accurately reflected by power ratio $r_i^{(\text{FWT1})}$. As for STFT-based method, although it can somehow well track the nonstationarity due to short-lived signal or HF components, yet at the same time

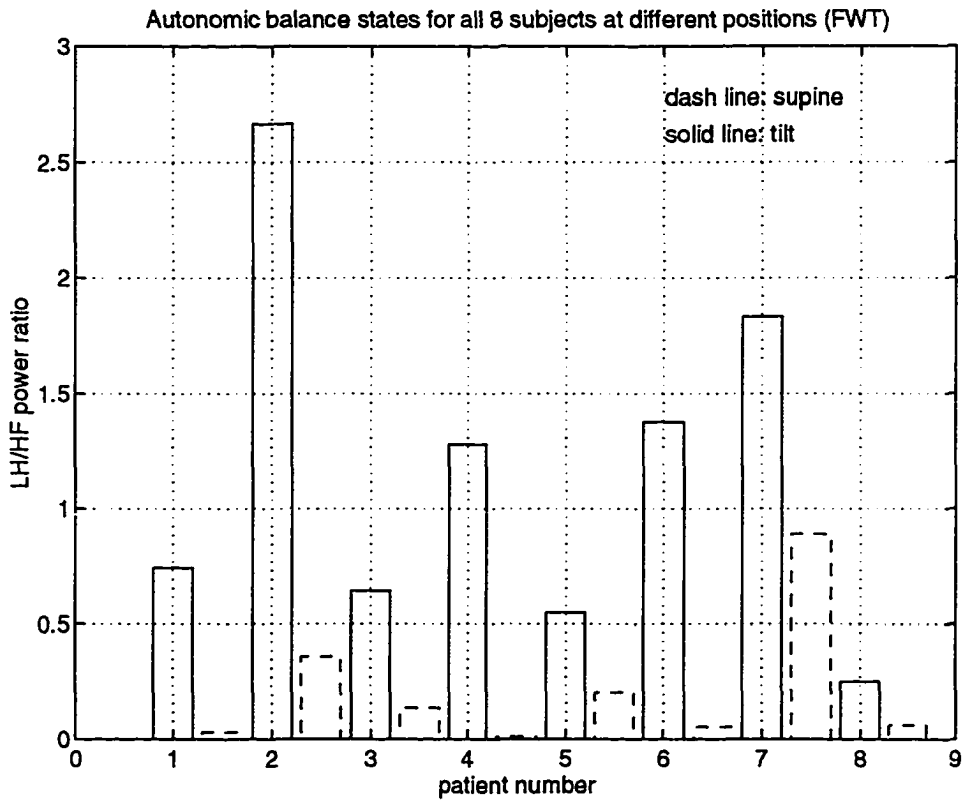


Figure 3.11: Short-time autonomic balance states during supine/tilt positions obtained by FWT analysis for all eight subjects (dash line: supine; solid line: tilt).

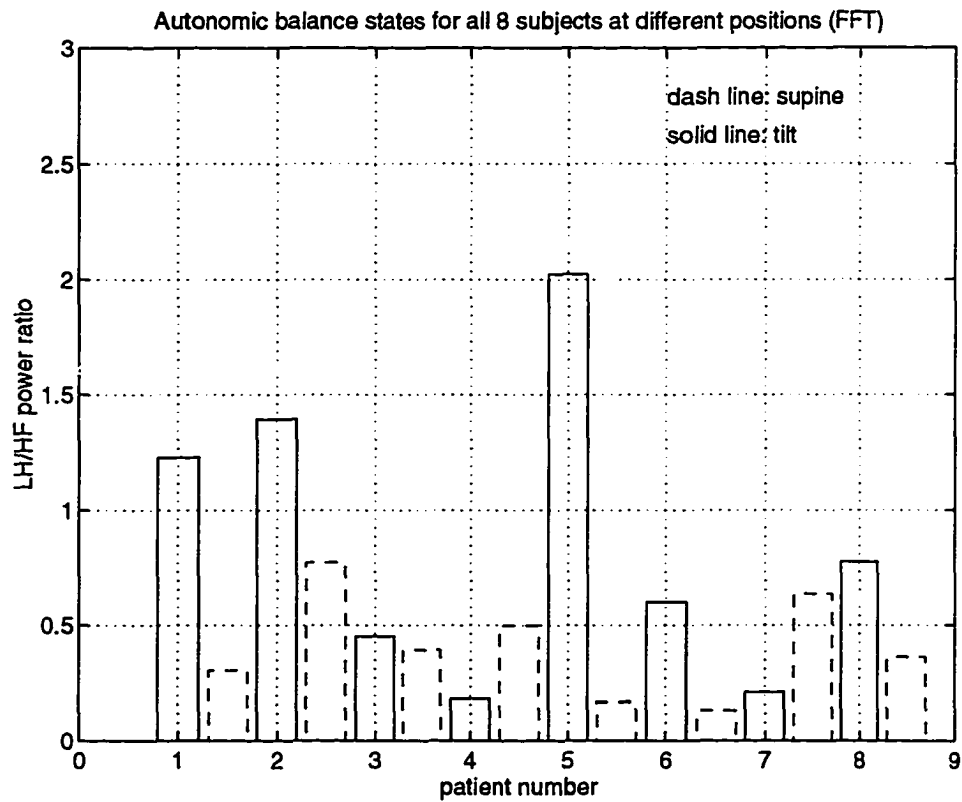


Figure 3.12: Short-time autonomic balance states during supine/tilt positions obtained by FFT analysis for all eight subjects (dash line: supine; solid line: tilt).

it loses resolution in LF components. On the other hand, taking a longer window to well resolve LF components will be simultaneously at the expense of preserving nonstationarity. Additionally, the continuity of the RR segments across the adjacent point of any two consecutive windows is also destroyed by zero paddings introduced by FFT computation. Therefore, because of failure in resolving LF components for shorter window, being unable to preserve the signal nonstationary for longer window and losing coherence of the signals across window boundaries, the STFT-based power estimation over a short window would be more or less distorted and hence the resultant power ratio $r_i^{(\text{FFT})}$ might be severely inaccurate.

3.4.3 Method Validation for Analysis Scheme 2

According to the description and demonstration in Section 3.3.2, we see that the analysis scheme 2 can monitor the instantaneous autonomic balance states in a much faster time frame. We here applied it to the same RR database and see if the tilt and supine positions for more subjects can be also successfully identified by the short-time power ratios of their corresponding RR signals. Recall the structure shown in Fig. 3.8 and the corresponding power ratio calculation formula in Eq. 3.9 first. As previously, choosing $[0.03125, 0.0625]$ Hz and $[0.125, 0.5]$ Hz as LF and HF bands, respectively, the computation in Eq. 3.9 would result in eight power ratio values for each subject during either tilt or supine stimulation and each value reflected the instantaneous autonomic balance state over an 8-second time interval. We then plotted the resultant power ratios for all these eight subjects in Fig. 3.13. Additionally, in order for performance evaluation we also computed the STFT-based power ratios for each subject in the database simply using Eq. 3.17 with number of windows $K = 8$ and then plotted the

results in Fig. 3.14. Note that, in both figures, for each subject while the solid line represents the instantaneous autonomic balance waveform under tilt stimulation, the dash line represents the one under supine stimulation.

As a result, observing Fig. 3.13 we see that there exists a clear separation between the power ratios obtained from tilt and supine stimulations for *almost* all subjects, indicating that the autonomic balance states might be still accurately estimated even during a much shorter time interval by this WT-based scheme. On the contrary, Fig. 3.14 revealed that the STFT-based instantaneous autonomic balance state estimates over very short windows for tilt and supine maneuvers were hard to be distinguished from each other in most cases.

Although STFT-based methods are widely diffused for their easy applicability, computational speed and direct interpretation of the results, Fourier transforms are theoretically defined on infinite data sequences and hence errors are introduced by the need to operate on finite data records in order to obtain estimates of the true functions. In fact, the finite short signal makes it necessary to make assumptions about the data *outside* the window. In most cases, they are considered to be zero. This implicit rectangular windowing process results in a spectral *leakage* in the PSD. Some different windows that more smoothly connect the side samples to zero are often used to solve the problem of leakage. They may, however, introduce a reduction in the frequency resolution. Actually, the frequency resolution is *inversely* related to the windowed data length, *i.e.*, $\Delta f_r \propto \frac{1}{N}$,⁴ and this is reduced by the windowing operation. Generally speaking, the shorter the window length, the worse the frequency resolution. In addition, a fixed frequency resolution for STFT method should also

⁴ Δf_r represents the frequency resolution. Note that this is conceptually different from the frequency spacing Δf introduced by FFT computation.

account for such a degraded performance. Therefore, the STFT-based analysis results appeared to be much worse than those obtained from WT-based analysis.

Since the structure of the analysis scheme 2 permits a more efficient use of the information associated with an RR signal so that accurate autonomic balance estimation over a much shorter time period may be attained, we here select this novel WT-based technique as the *principal method* for this dissertation research. That is, the occurrence of NSVT will be investigated next by assessing the HRV immediately before the onset of NSVT mostly using the principal method.

3.5 Frequency Responses of the Dyadic Wavelet Functions

To this end, a discussion on frequency responses of the dyadic wavelet functions are provided. According to Eq. 2.8, we see that the WT computation is actually obtained by a filtering process. That is, Eq. 2.8 can be realized by a filter bank structure formed by a number of *bandpass* filters, as shown in Fig. 3.15. Note that in this discussion, the dyadic wavelets are considered and the number of scaling levels is set to 5. Therefore, there are 5 filters included in Fig. 3.15 and obviously, each one of them has the form as

$$w_j(t) = 2^{j/2}\psi^*(-2^j t), \quad j = -1, \dots, -5, \quad (3.18)$$

which is the reflected complex conjugate of the scaled wavelet function $\psi(x)$ (by factor of 2^{-j}). Denoting the signal of interest as the input signal $x(t)$, the WT computation is thus performed simply by the convolution as

$$d_j(t) = x(t) * w_j(t), \quad j = -1, \dots, -5, \quad (3.19)$$

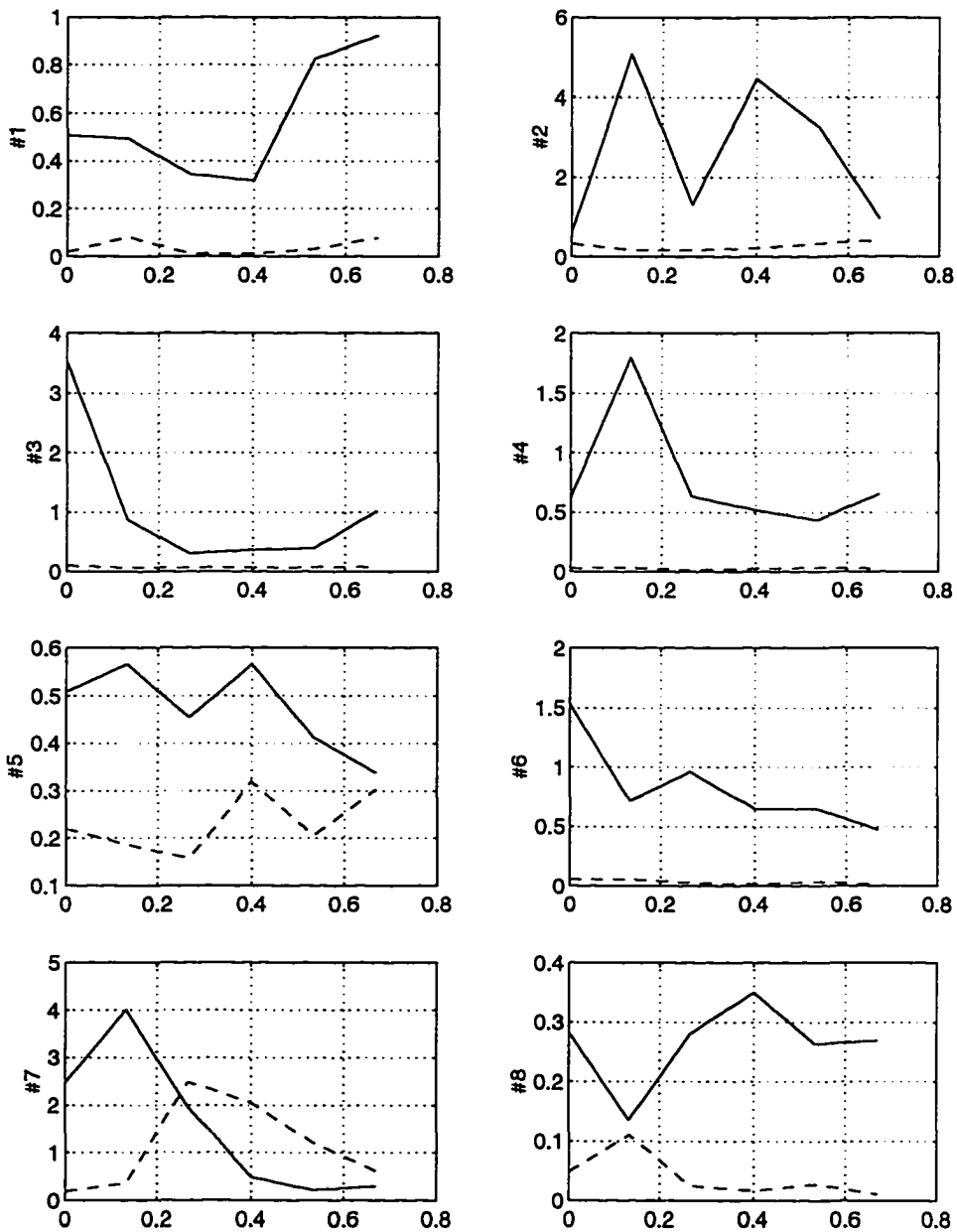


Figure 3.13: The WT-based autonomic balance state estimates (from analysis scheme 2) during supine (dash line) and tilt (solid line) maneuvers for all the eight subjects (#1-#8) in the database for method validation.

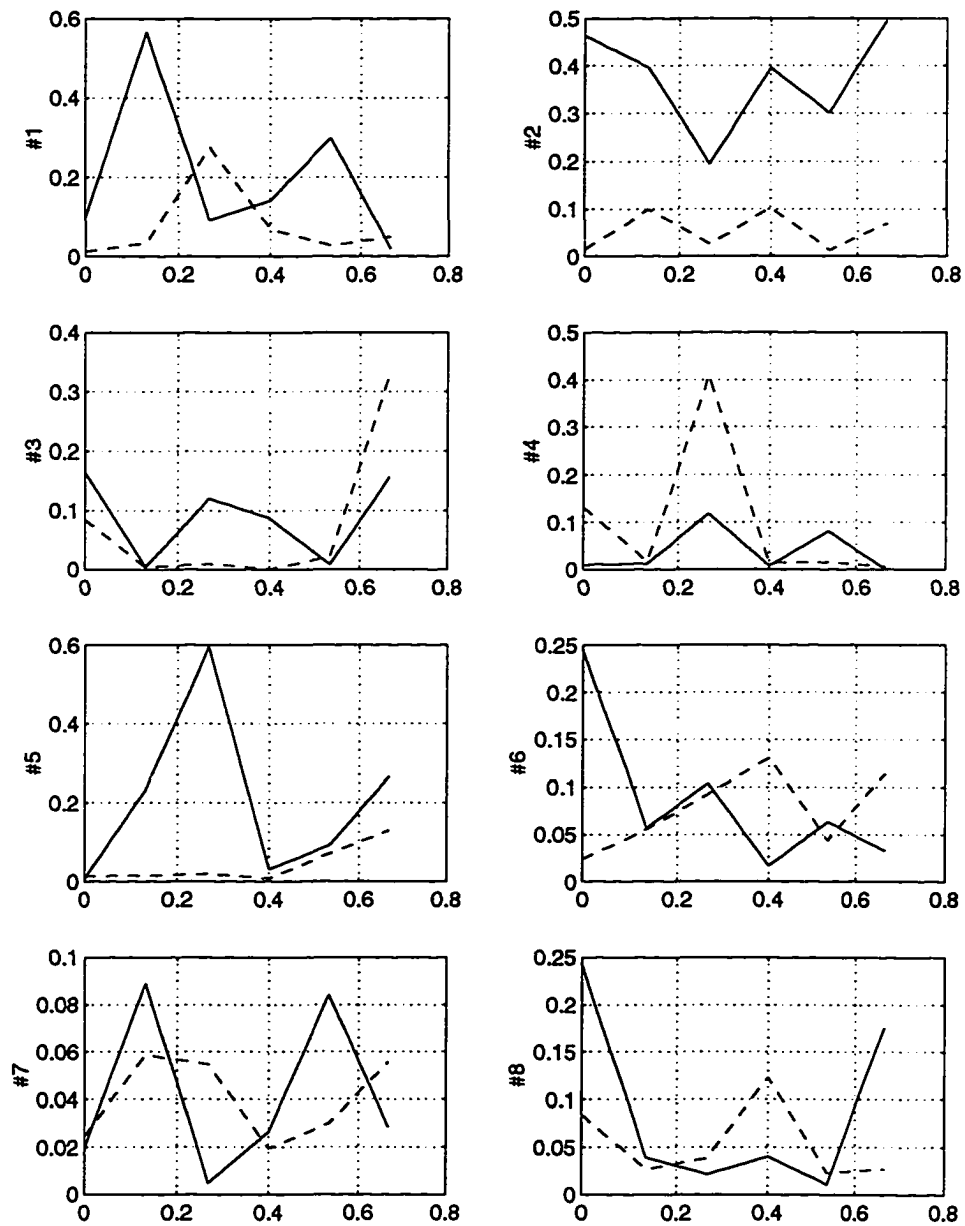


Figure 3.14: The traditional STFT-based autonomic balance state estimates during supine (dash line) and tilt (solid line) maneuvers for all the eight subjects (#1-#8) in the database for method validation.

where $d_j(t)$ represents the detail signal at the j -th dyadic level. Since in this research we employed the Daubechies wavelet system filters with 8 coefficients (denoted as Daubechies(8)), the concern is that although the passbands of $h(k)$ (scaling filter) and $g(k)$ (wavelet filter) should be theoretically equal to $[0,0.5]$ Hz and $[0.5,1]$ Hz (assuming the sampling frequency $f_s = 2$ Hz), respectively, practically both filters do not have sharp cut-off edges in frequency domain. Observing the frequency responses of these two filters shown in Figs. 3.16(a) and (b), we can see the spectra of both filters are very smooth at the cut-off edges. Since there exists a relation between the filter systems $\{h(k), g(k)\}$ and $\{w_j(t)\}_{j=-1}^{-5}$, such blunt cut-off edges associated with $\{h(k), g(k)\}$ may introduce serious leakage to the filters $\{w_j(t)\}_{j=-1}^{-5}$ so that the performance of these filtering processes may be severely degraded.

Filter	Passband (theoretical values)	Passband (3 dB estimates)
$w_{-1}(t)$	0.5–1 Hz	0.5400–0.9990 Hz
$w_{-2}(t)$	0.25–0.5 Hz	0.2812–0.5254 Hz
$w_{-3}(t)$	0.125–0.25 Hz	0.1406–0.2607 Hz
$w_{-4}(t)$	0.0625–0.125 Hz	0.0703–0.1299 Hz
$w_{-5}(t)$	0.03125–0.0625 Hz	0.0352–0.0645 Hz

Table 3.3: Passbands of the 5 filters in Fig. 3.15. Here, the theoretical and the estimated frequency bands (*i.e.*, 3 dB cut-off frequency) are both provided.

Here, we try to quantitatively evaluate how well the filtering processes can preserve and separate signal components in different bands corresponding to a variety of the WT functions. First, the impulse responses of the 5 filters in Fig. 3.15 are calculated by setting $x(t) = \delta(t)$. Fig. 3.17 provides the plots of the impulse responses (left column) and their corresponding spectra (right column) for all these filters when

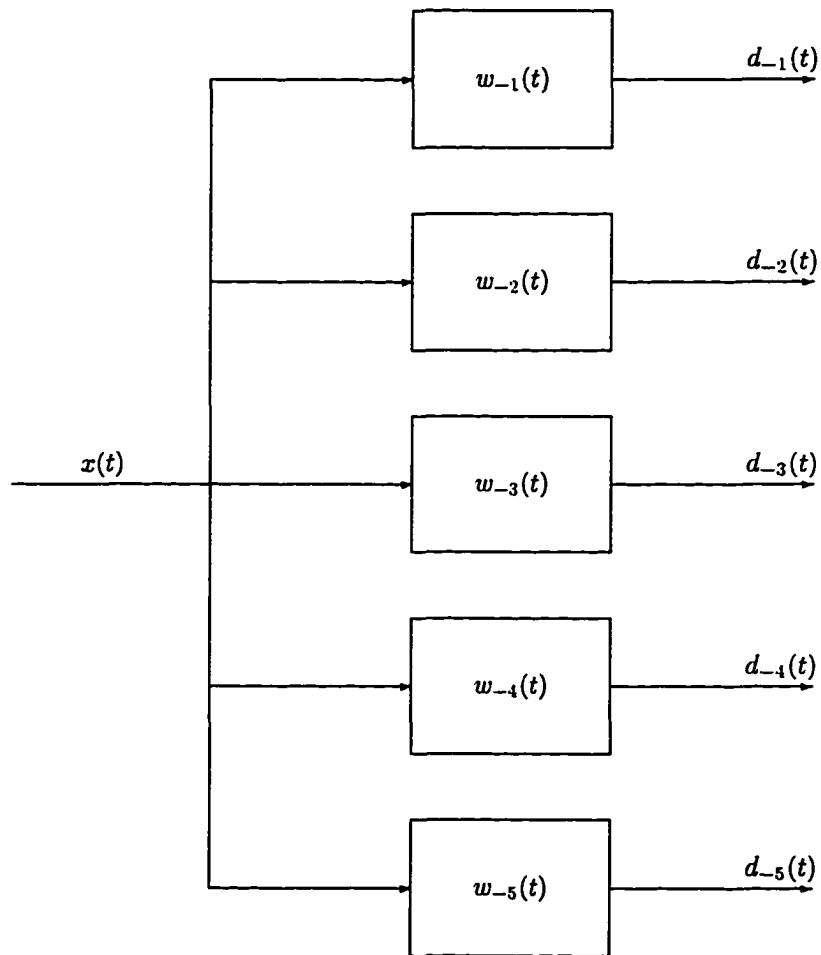


Figure 3.15: Realization of the filtering structure involved in WT computation. $x(t)$ represents the input signal to be analyzed and $d_{-1}(t), \dots, d_{-5}(t)$ represent the output signals of the 5 filters $w_{-1}(t), \dots, w_{-5}(t)$, respectively. Note that the output signals $d_{-1}(t), \dots, d_{-5}(t)$ can be equivalently visualized as the detail signals at level $2^{-1}, \dots, 2^{-5}$, respectively, in WT computation.

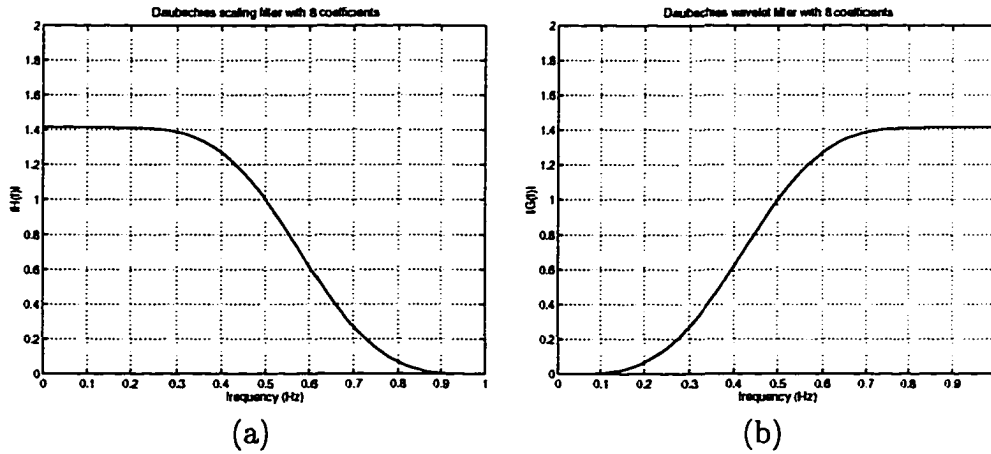


Figure 3.16: Frequency responses of the Daubechies wavelet system filters with 8 coefficients: (a) scaling filter $h(k)$; (b) wavelet filter $g(k)$.

Daubechies(8) is employed. Since the spectrum of $\delta(t)$ is a constant throughout the entire frequency axis, theoretically the impulse responses of the filters $\{w_j(t)\}_{j=-1}^{-5}$ should have a constant band-limited spectra (*i.e.*, the ideal bandpass filters). We see from Fig. 3.17, however, that each one of these frequency responses (represented by solid lines in right column) appears to be a smoother bandpass filter. Table 3.3 provides listings of both the estimated and ideal values of passbands for these filters. In general, it reveals from Table 3.3 that the central frequencies (*i.e.*, 3 dB cut-off frequencies) of these smooth bandpass filters can accordingly well approximate to the ideal ones.

Additionally, Fig. 3.17 also indicates that spectra of these smoother bandpass filters will *overlap* at their edges. Therefore, it can be seen that the filtering processes involved in the WT computation may *not always* be able to completely separate the signal components into different dyadic frequency bands. This may lead to an

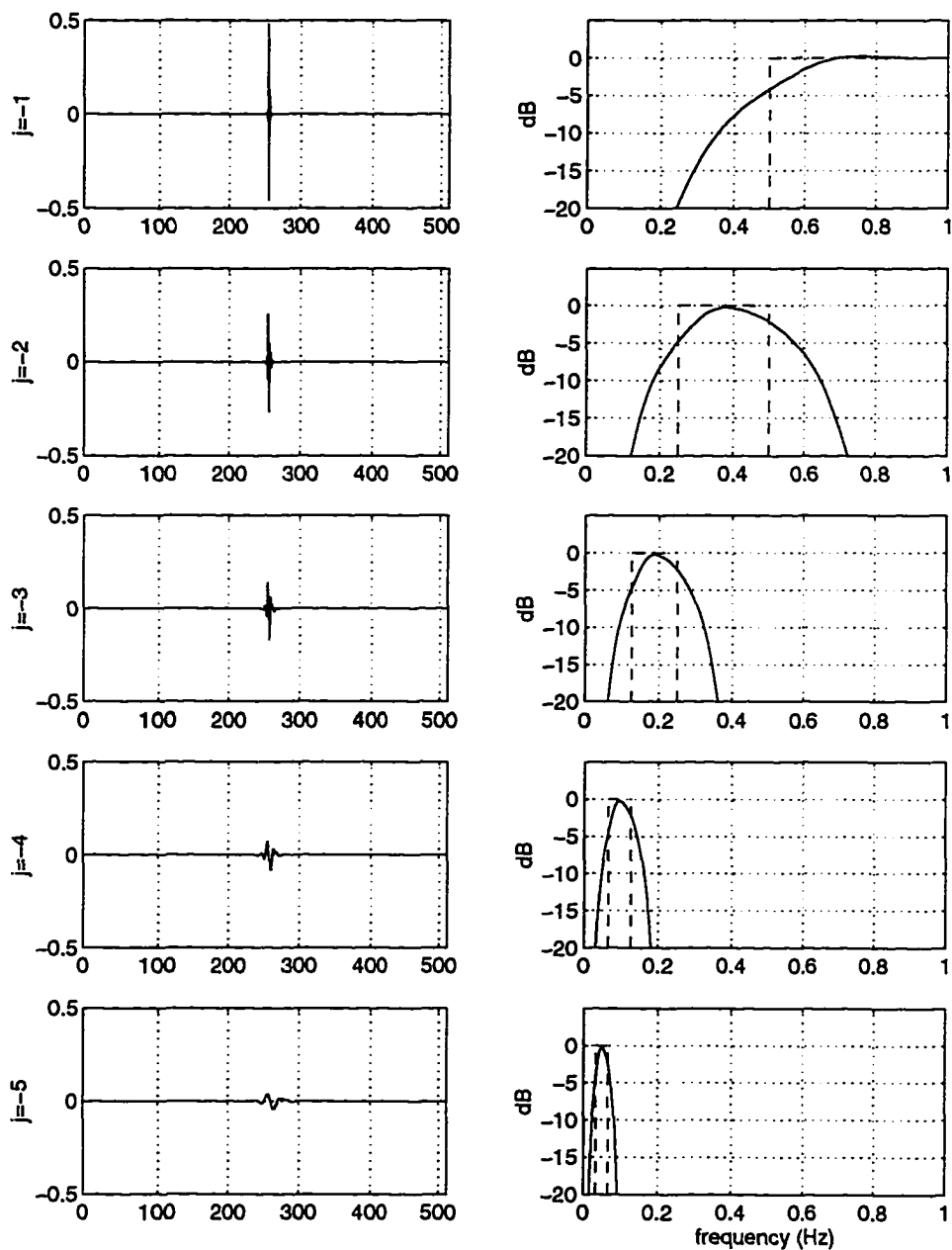


Figure 3.17: Plots of the impulse responses (left column) and their corresponding frequency responses (right column) for all the 5 filters in Fig. 3.15. Note that for each plot in right column, dash line represents the theoretical frequency response (*i.e.*, a ideal bandpass filter) and solid line represent the actual frequency response of the filter $w_j(t)$.

inaccurate spectral power estimation for the signal components in bands of interest. In this dissertation research, we adopted the dyadic bands $j = -2, -3$ as HF and $j = -5$ as LF, and the WT coefficient estimation was performed using Daubechies(8) wavelet system filters. Observing the corresponding frequency responses of these 3 bandpass filters depicted in Fig. 3.18, we may see that there is a overlapped spectral region between the filters $w_{-2}(t)$ and $w_{-3}(t)$, and also another one is found between $w_{-3}(t)$ and $w_{-5}(t)$. The latter may be negligible because the response magnitudes of both filters ($w_{-3}(t)$ and $w_{-5}(t)$) in their common spectral region are all very small (less than -12 dB). The former looks more significant, but almost all the response magnitudes of both filters ($w_{-2}(t)$ and $w_{-3}(t)$) in this overlapped spectral region are less than -5 dB. Fortunately, it appears that Daubechies(8) wavelet system is suitable to this research.

According to the discussion above, it should be noted that *not all* the wavelet system filters are suitable to the application in this research. A bad choice of wavelets may lead to a severely inaccurate spectral power or spectral power ratio estimation and thus degrade the performance of pattern classification task. Generally speaking, a wavelet system that allows a smaller overlapped spectral region between the passbands of any two bandpass filters associated with that wavelet system is desired and can be selected as a candidate for the analysis in this research.

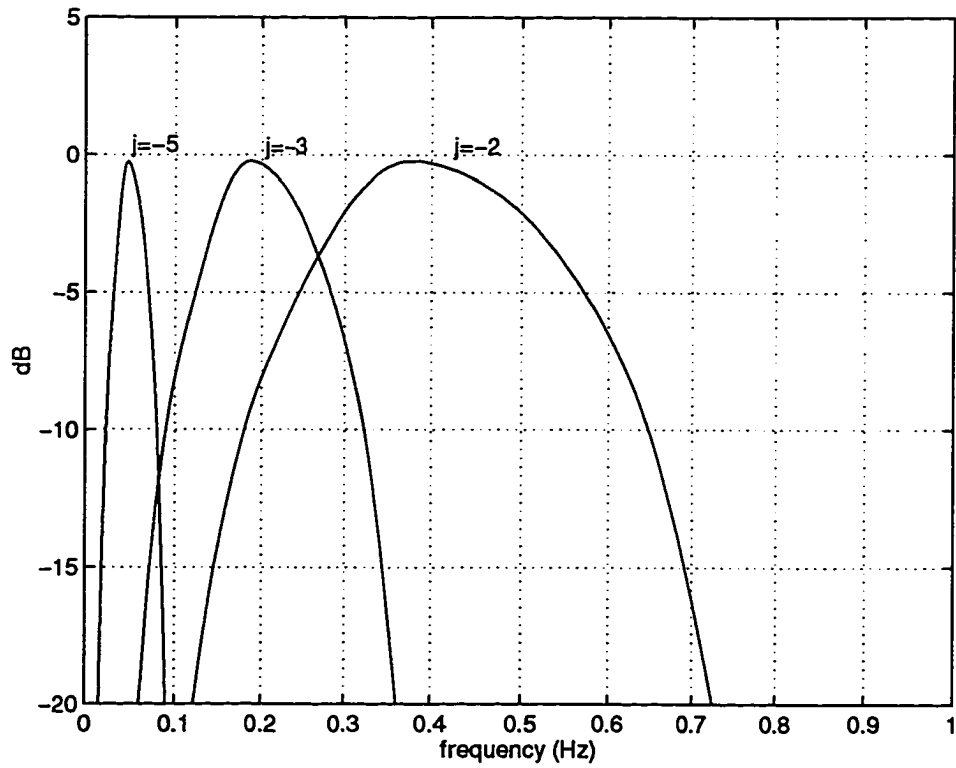


Figure 3.18: Frequency responses of the smooth bandpass filters employed in this research. Here, we adopted the dyadic bands $j = -2, -3$ as HF and $j = -5$ as LF.

CHAPTER 4

THE APPLICATION OF WT-BASED HRV ANALYSIS TO THE PREDICTION OF NSVT

After introducing the WT-based methods and getting confidence from the method validation in Chapter 3, we now seek for the further application of the principal method (*i.e.*, analysis scheme 2) to the proposed research study on the examination of HRV, reflected by the short-time autonomic balance evolution, immediately before the onset of NSVT, towards the investigation and prediction of NSVT.

4.1 A Postulate

A decreased HRV or an increased autonomic balance index quantified by spectral power ratio LF/HF has been recognized as a long-term predictor of SCD and arrhythmic death after MI. There is substantial experimental evidence suggesting that an unbalanced autonomic influence on heart is associated with a propensity to electrical instability and ventricular tachyarrhythmias [75, 99]. However, direct evidence for changes or a derangement in HRV immediately before the onset of spontaneous ventricular tachycardia is still scarce and disputed. It seems that an increased sympathetic activity to the heart is usually arrhythmogenic, whereas parasympathetic activity may serve as a protective effect [36]. We thus here make a postulate that

the *autonomic balance state* (ABS) evolution $LF(t)/HF(t)$ would somehow abruptly increase or reach to a very high level over a short period when measured in 8–20 minutes prior to NSVT episodes, whereas in other cases such as ischemia or healthy the same phenomenon would not be seen in their ABS waveforms.

4.2 Database

We collected a patient group consisting of 64 patients for a numerical experiment of HRV assessment. The patient group was composed of 31 NSVT patients⁵ provided by the cardiology division in the Ohio State University, 28 ischemic patients from the European ST-T database and 5 healthy subjects from the volunteers. Knowing that the European ST-T database was produced with the goal of defining an ECG database as a reference for assessing the quality of ambulatory ECG analysis systems for detection of myocardial ischemia, we therefore adopted this database as the ischemic group in this study.

The database was then constructed by including the ECG signals recorded from these 64 adults first. After detecting the time locations of the R waves for the ECG signal of each patient in the group using an R-wave detection algorithm, the corresponding RR-interval data sequence can be then found simply using Eqs. 3.1 and 3.2. It should be noted that for the purpose of spectral analysis, the RR signals obtained above need to be further preprocessed by a linear interpolation between each pair of consecutive RR values and then, by a resampling task with anti-aliasing filtering as described in Chapter 3. Since the frequency components of interest for HRV analysis is usually below 1 Hz [56], we here set the resampling frequency as $f_s = 2$ Hz.

⁵All these NSVT patients also had *coronary artery disease* (CAD).

4.2.1 Data Selection Criteria

NSVT Selection

In this study, patients with SA node dysfunction, abnormal AV conduction and cardiac pacemakers were excluded. For NSVT episodes, 24-hour RR intervals were obtained from ambulatory Holter ECGs on a commercial Holter scanner system. Knowing that NSVT is defined as three or more consecutive broad QRS complexes with a rate ≥ 120 beats/minute and lasting less than 30 seconds, we thus set criteria for the selection of NSVT episodes to be analyzed as follows. To avoid any potential inaccurate power ratio (or ABS value) estimates resulted from the existence of VPB, an NSVT episode to be analyzed was selected if there was no VPB found within, at least, 512 seconds (≈ 8.53 minutes) prior to the onset of NSVT. Note that the Holter scanner might be occasionally unable to correctly label all QRS complexes (*e.g.*, usually mislabeling normal beats as artifacts), the QRS complexes during the 20-minute period before NSVT were also visually checked to ensure that all normal QRS complexes during this period were correctly labeled. Moreover, patients with frequent NSVT or VT throughout the whole 24-hour recordings were excluded because any “clean” RR signal (“clean” means RR recording without any VPBs) that lasts, at least, 512 seconds could not be found in frequent ectopic beats and such recordings were hence unsuitable for HRV assessment before the onset of NSVT.

Consequently, the selection criteria resulted in a number of RR recordings, *i.e.*, valid *normal-to-normal* (NN) intervals, prior to the onset of NSVT with different length ranged from 8 to 20 minutes. In fact, such a variable episode length will not affect the performance of this research. We may speculate that these NSVT episodes would permit an accurate HRV assessment over an appropriately long period without

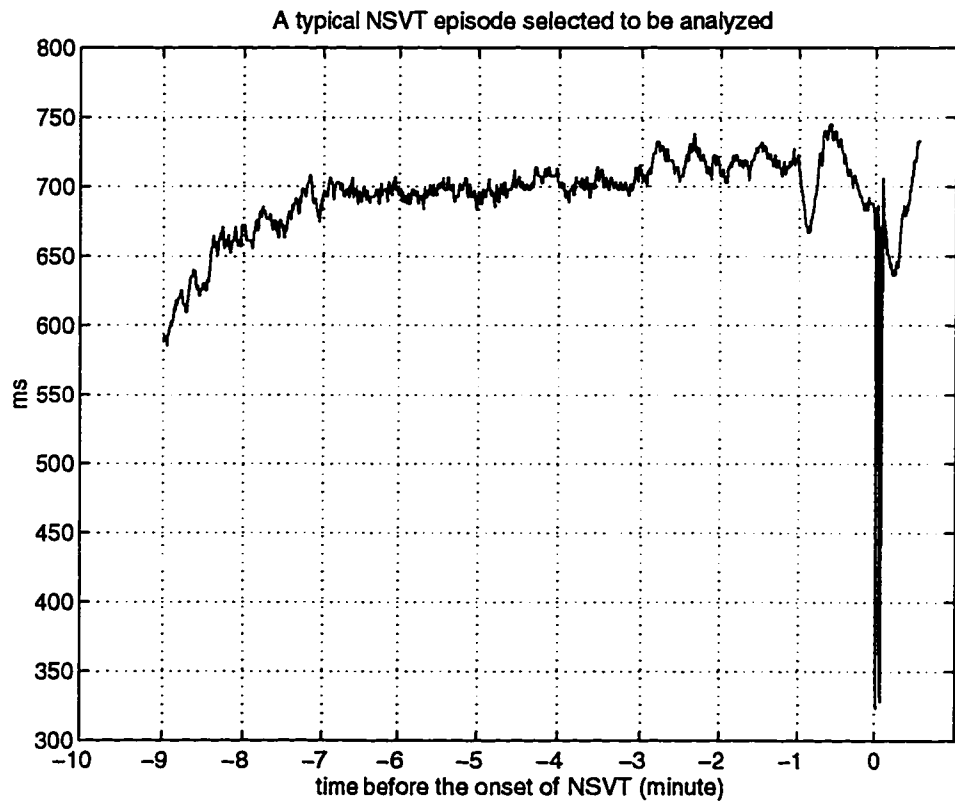


Figure 4.1: A typical observation of RR-interval (or NN-interval) signals for an NSVT episode selected to be analyzed. Note that here the time located at 0 minute represents the onset of NSVT.

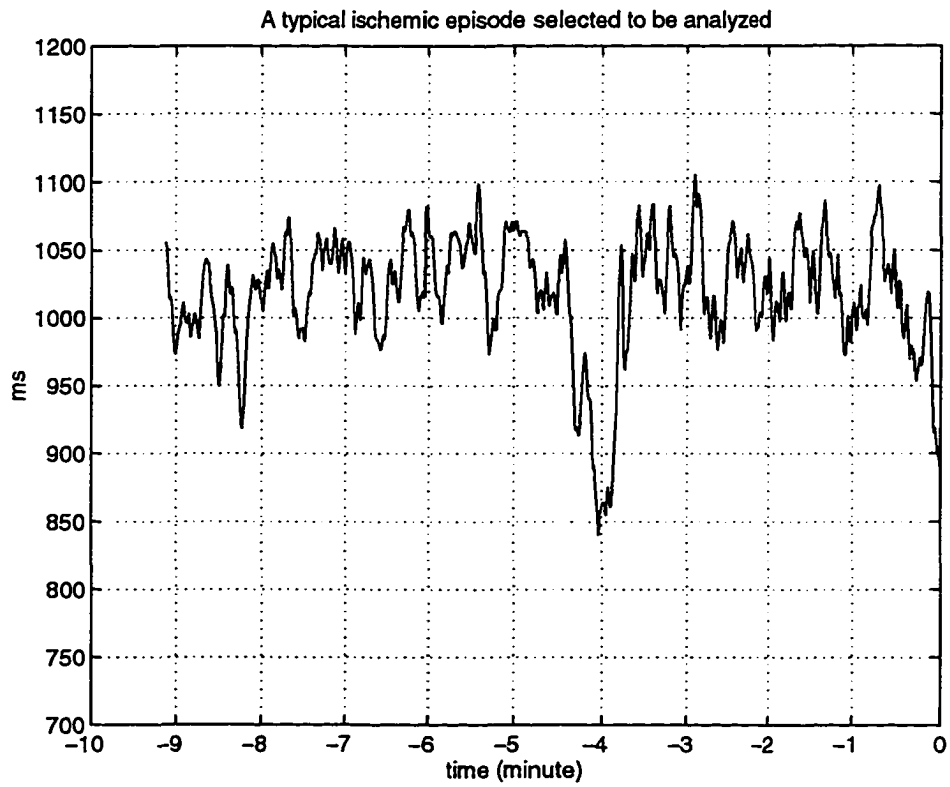


Figure 4.2: A typical observation of RR-interval (or NN-interval) signals for an ischemic episode selected to be analyzed.

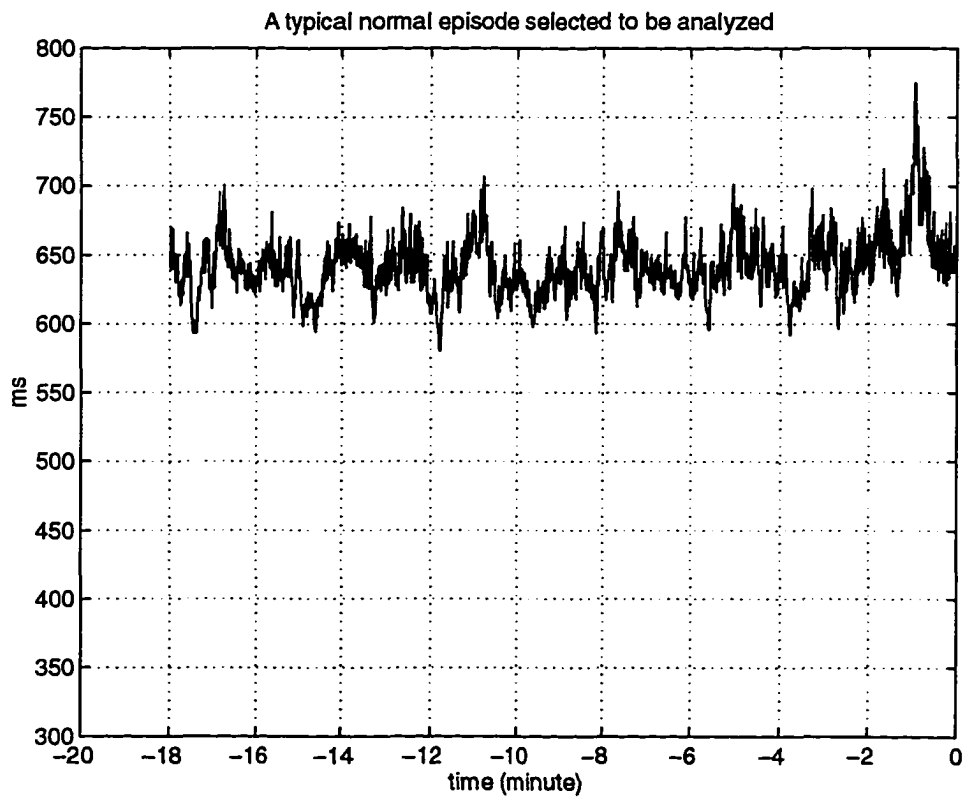


Figure 4.3: A typical observation of RR-interval (or NN-interval) signals for a normal episode selected to be analyzed.

influence from VPBs. Fig. 4.1 gives a typical observation of RR-interval (or NN-interval) signals for a selected NSVT episode. Note that in this figure, the time located at 0 minute represents the onset of NSVT and the HRV assessment was performed immediately before this point of time location.

Non-NSVT Selection

As for the ischemic and healthy subjects, we here randomly selected the RR signals without VPBs for a period lasting at least 8 minutes long but less than 20 minutes. Similarly, Figs. 4.2 and 4.3 show typical examples of RR-interval signals for a selected ischemic and normal episodes, respectively. As a result, the demonstrative RR database was formed by totally 153 episodes, consisting of 87 NSVT episodes, 61 ischemic episodes and 5 healthy episodes.

4.3 Approach

4.3.1 Design Motivation

Short-time HRV was examined on all episodes in the database simply using an approach designed based on the WT-based analysis scheme 2 described in Section 3.3.2. The resampled RR signals were first transformed into wavelet space to allow a temporal representation of the dyadic spectral components buried in signals. The short-time HRV measures were then reflected by the LF to HF spectral power ratio $r_{i,l,m}$ calculated using Eq. 3.9. It should be noted that since the dyadic wavelet analysis only can be applied to an RR signal with the length of 2^m power, in order to get as many short-time power ratios as possible for the entire RR signal the analysis approach applied here needs to be designed based on further modifications on the WT-based analysis schemes 2. Such a modified approach is then able to overcome the analysis-length

limitation problem (*i.e.*, limited to 2's power) resulted from dyadic WT analysis so that the RR data might be utilized with maximum efficacy. Modification of this approach is described in the following.

4.3.2 Analysis Unit (AU) Based Scheme

Here, we define a block with the length of 512 seconds as an *analysis unit* (AU). Generally speaking, an AU can be visualized as a window used to monitor an RR signal in a shorter segment for signal analysis. Similar to the computational structure of the analysis scheme 2, FWT is computed for an AU first. The conceptual diagram of the time-frequency structure in wavelet space for an AU is given in Fig. 4.4. Once the FWT has been computed and the window length (or known as the PCU length) M is determined, the total number of windows (or PCU's) at each level, $N_{win}^{(j)}$, is thus determined by N_j/M , where N_j represents the total number of WT coefficients at level 2^j . The short-time spectral power calculation is then performed on each of these windows using the WT coefficients. After power calculation, the instantaneous ABS can be then measured simply by finding the LF to HF spectral power ratios. Here, we chose window length as $M = 4$ and the number of FWT analysis levels as $L = 5$ for an AU. This resulted in the numbers of the analysis windows $N_{win}^{(-1)} = 128$, $N_{win}^{(-2)} = 64$, $N_{win}^{(-3)} = 32$, $N_{win}^{(-4)} = 16$ and $N_{win}^{(-5)} = 8$ at levels 2^{-1} , 2^{-2} , 2^{-3} , 2^{-4} and 2^{-5} , respectively. These are also illustrated in Fig. 4.4. Recall that LF=[0.03125,0.0625] Hz and HF=[0.125,0.5] Hz. The short-time HRV measures $r_{i,l,m}$ for an AU were calculated using Eq. 3.9 with $(i, l, m) = (1, 1, 1), (1, 1, 2), \dots, (8, 32, 63), (8, 32, 64)$, yielding 64 ABS values equally distributed in the 512-second period.

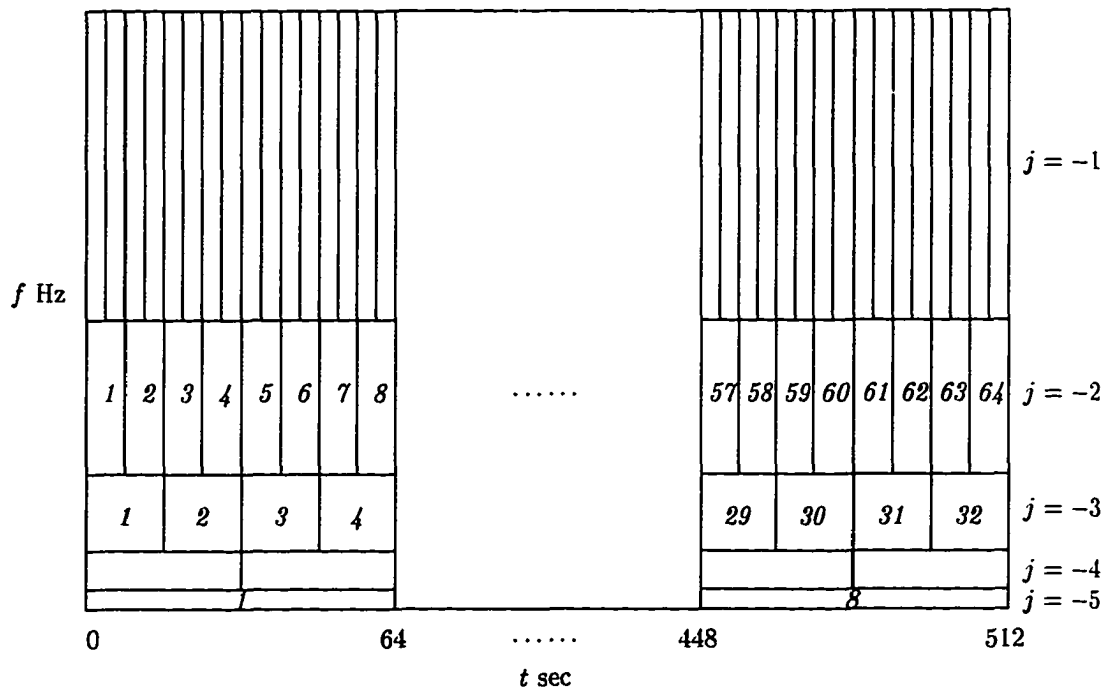


Figure 4.4: The structural plot of an *analysis unit* (AU). It can be seen that varying real-time intervals occupied by the tiles at different levels. Note that here an AU contains 8 windows at the lowest level (level 2^{-5}). Each tile (or window) contains 4 WT coefficients. In addition, the enumerative numbers (in italic style) for the windows at the levels of interest ($j = -2, -3, -5$) are used to describe the window movement, expressed as: $(1, 1, 1) \rightarrow (1, 1, 2) \rightarrow (1, 2, 3) \rightarrow \dots \rightarrow (8, 31, 61) \rightarrow (8, 31, 62) \rightarrow (8, 32, 63) \rightarrow (8, 32, 64)$.

Before processing the next AU further, we need to carefully choose the time-shift for the moving block so that the location next AU can be determined. Observing the structure in Fig. 4.4, first we see that there are 8 ABS values corresponding to an LF power value and also, an AU contains 8 LF power values. Since each fixed LF power value was calculated from a window at the lowest dyadic level (*i.e.*, level 2^{-5}), in order to preserve all the LF, HF power values and ABS values in the *intersectional region* of any two consecutive AU's we thus shifted the block by a step of real-time interval S , where S is a multiple of the time period occupied by a window at level 2^{-5} . That is, the next AU could be obtained by shifting the block by $S = k\Delta T_{-5} = 64k$ seconds, where k is an integer. Here, we chose $k = 1$ so that the real-time shift interval $S = 64$ seconds. Then, we redid the power ratio computation, as described above, for this new AU. Consequently, another 64 power ratios or ABS values would be obtained. Such a shift-and-computation process was repeated until the AU finally reached to the onset of NSVT. Illustration of this process is given in Fig. 4.5. Group the 8 ABS values corresponding to the p -th LF power (*i.e.*, the LF power measured from the p -th window at level 2^{-5}) into a column vector, denoted as $\mathbf{r}_p^{(q)}$, for the q -th AU. Knowing that there existed 8 windows at level 2^{-5} (or $N_{win}^{(-5)} = 8$) for an AU and $S = 64$, we then have

$$\begin{bmatrix} \mathbf{r}_2^{(q)} \\ \mathbf{r}_3^{(q)} \\ \vdots \\ \mathbf{r}_8^{(q)} \end{bmatrix} = \begin{bmatrix} \mathbf{r}_1^{(q+1)} \\ \mathbf{r}_2^{(q+1)} \\ \vdots \\ \mathbf{r}_7^{(q+1)} \end{bmatrix}. \quad (4.1)$$

Eq. 4.1 indicates that the vectors $\mathbf{r}_2^{(q)}, \mathbf{r}_3^{(q)}, \dots, \mathbf{r}_8^{(q)}$ obtained from the q -th AU should be *identical* to the vectors $\mathbf{r}_1^{(q+1)}, \mathbf{r}_2^{(q+1)}, \dots, \mathbf{r}_7^{(q+1)}$ obtained from the $(q + 1)$ -th AU,

respectively. This is because both groups of vectors reflected the ABS evolution in the intersectional region between the q -th and $(q + 1)$ -th AU's.

As noted in Chapter 3, we see that the power ratio estimates involved in the very last windowed region (*i.e.*, $\mathbf{r}_8^{(q)}$, for $q = 1, 2, \dots$) may not be so reliably accurate as the others since the zeros padded after the ending point may cause inaccurate power estimates of the signals at all levels in the last windowed region. However, according to Eq. 4.1 it can be inferred that $\mathbf{r}_8^{(q)}$ may be replaced by a more accurate estimate $\mathbf{r}_7^{(q+1)}$. Therefore, to accurately track ABS evolution over the entire RR signal before NSVT we first performed the shift-and-computation process and then, adopted $\mathbf{r}_1^{(1)}, \mathbf{r}_2^{(1)}, \dots, \mathbf{r}_7^{(1)}$ from the first AU and successively took $\mathbf{r}_7^{(2)}, \mathbf{r}_7^{(3)}, \dots$ from the second, third, ... AU's, respectively, to yield the ABS evolution estimate. This successive ABS padding process is illustrated in Fig. 4.5. It can be also formulated as follows. Suppose we have n AU's for an RR signal, the corresponding ABS evolution estimate, denoted as \mathbf{r}_{evol} , can be simply formed by

$$\mathbf{r}_{evol} = [\mathbf{r}_1^{(1)T} \ \mathbf{r}_2^{(1)T} \ \dots \ \mathbf{r}_7^{(1)T} \ \mathbf{r}_7^{(2)T} \ \mathbf{r}_7^{(3)T} \ \dots \ \mathbf{r}_7^{(n-1)T} \ \mathbf{r}_7^{(n)T} \ \mathbf{r}_8^{(n)T}]^T. \quad (4.2)$$

Note that Eq. 4.2 is not the only path to achieve the estimate of ABS evolution \mathbf{r}_{evol} . According to Eq. 4.1, we can see that $\mathbf{r}_7^{(q)}, \mathbf{r}_6^{(q)}, \dots, \mathbf{r}_2^{(q)}$ may be also replaced by a $\mathbf{r}_6^{(q+1)}, \mathbf{r}_5^{(q+1)}, \dots, \mathbf{r}_1^{(q+1)}$, respectively, and these would result in 6 more paths to attain the identical estimate of \mathbf{r}_{evol} .

To more clearly demonstrate the above processes, a practical example is given in the following descriptions. Table 4.1 provides the numerical power ratio estimates obtained after applying the shift-and-computation process to an RR signal preceding the onset of NSVT (given in Fig. 4.1). Obviously, from this table we may see that there are 5 AU's in this example. Also, we can represent these numerical results

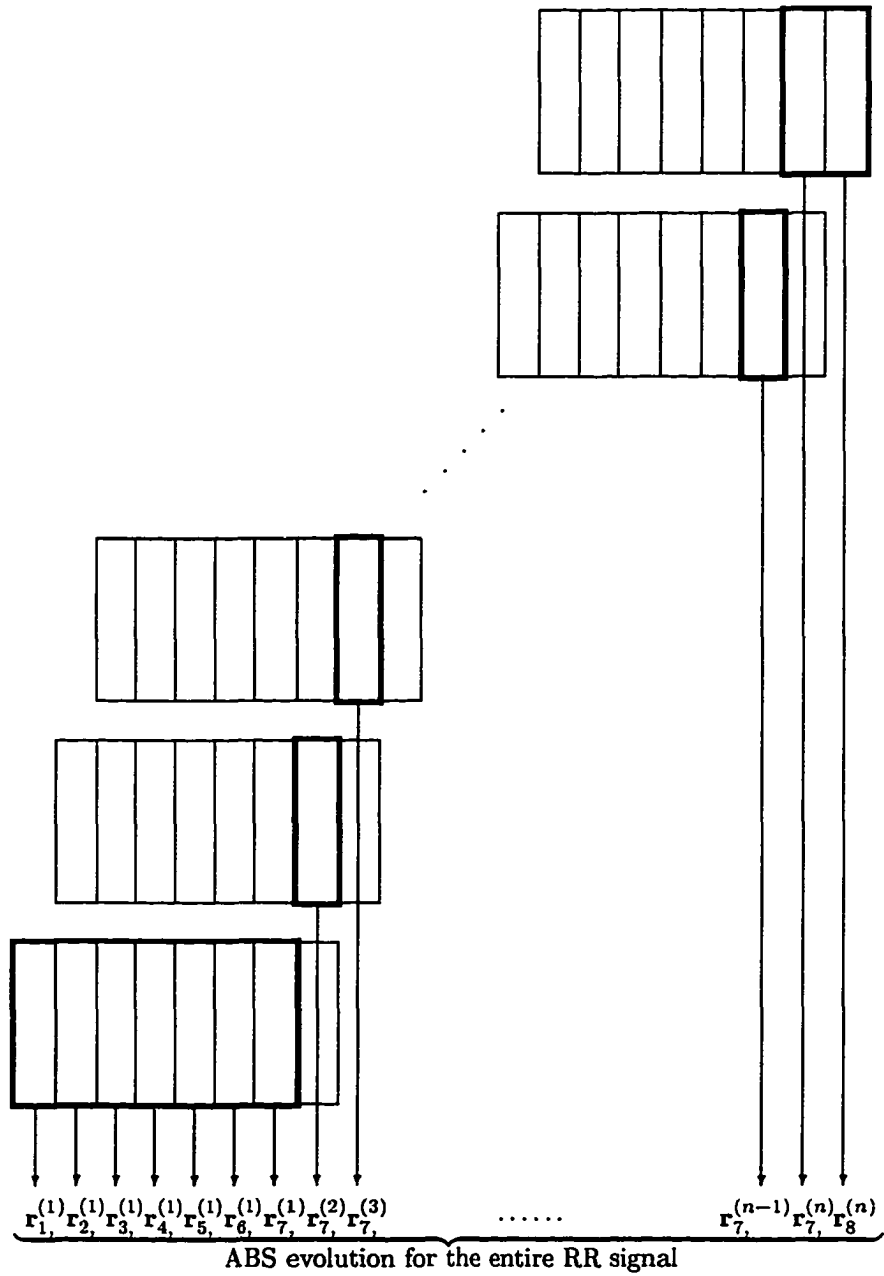


Figure 4.5: The schematic diagram for the AU-based approach. In this diagram, it includes illustrations of both the shift-and-computation and ABS padding processes.

$r_1^{(1)}$	$r_2^{(1)}$	$r_3^{(1)}$	$r_4^{(1)}$	$r_5^{(1)}$	$r_6^{(1)}$	$r_7^{(1)}$	$r_8^{(1)}$
2.5296	0.5230	1.7918	1.3602	1.2599	2.9048	3.1328	4.3143
1.6285	0.4260	2.9369	0.6402	1.6773	6.1764	5.6768	4.2211
7.2145	0.6407	8.5979	1.4546	2.7141	8.2953	3.7326	4.0995
4.4374	0.9775	6.7140	7.0072	1.2478	7.3329	3.4664	2.4771
1.3363	0.7590	1.4191	2.0469	1.0515	2.4412	13.8742	3.3150
1.0422	0.7380	1.4163	1.8032	0.7279	1.6900	10.2032	3.1250
2.0520	3.8313	3.8317	3.7867	0.7432	5.0830	1.6116	5.0457
1.0590	2.8022	1.8474	5.0265	0.6831	3.4568	4.0262	30.6174
$r_1^{(2)}$	$r_2^{(2)}$	$r_3^{(2)}$	$r_4^{(2)}$	$r_5^{(2)}$	$r_6^{(2)}$	$r_7^{(2)}$	$r_8^{(2)}$
0.5230	1.7918	1.3602	1.2599	2.9048	3.1422	5.5016	0.2529
0.4260	2.9369	0.6402	1.6773	6.1764	5.6939	5.3827	0.1523
0.6407	8.5979	1.4546	2.7141	8.2953	3.7439	5.2276	0.2871
0.9775	6.7140	7.0072	1.2478	7.3329	3.4768	3.1588	0.4896
0.7590	1.4191	2.0469	1.0515	2.4412	13.9159	4.2195	0.2560
0.7380	1.4163	1.8032	0.7279	1.6900	10.2339	3.9781	0.2137
3.8313	3.8317	3.7867	0.7432	5.0830	1.6164	4.7866	0.4104
2.8022	1.8474	5.0265	0.6831	3.4568	4.0383	3.3155	13.9495
$r_1^{(3)}$	$r_2^{(3)}$	$r_3^{(3)}$	$r_4^{(3)}$	$r_5^{(3)}$	$r_6^{(3)}$	$r_7^{(3)}$	$r_8^{(3)}$
1.7918	1.3602	1.2599	2.9048	3.1422	5.4936	2.1422	0.5650
2.9369	0.6402	1.6773	6.1764	5.6939	5.3749	1.2899	1.7076
8.5979	1.4546	2.7141	8.2953	3.7439	5.2200	2.4325	0.9384
6.7140	7.0072	1.2478	7.3329	3.4768	3.1542	4.1480	2.6462
1.4191	2.0469	1.0515	2.4412	13.9159	4.2134	2.1688	1.1081
1.4163	1.8032	0.7279	1.6900	10.2339	3.9723	1.8099	1.2126
3.8317	3.7867	0.7432	5.0830	1.6164	4.7796	2.0406	3.4974
1.8474	5.0265	0.6831	3.4568	4.0383	3.3106	3.3808	3.5851
$r_1^{(4)}$	$r_2^{(4)}$	$r_3^{(4)}$	$r_4^{(4)}$	$r_5^{(4)}$	$r_6^{(4)}$	$r_7^{(4)}$	$r_8^{(4)}$
1.3602	1.2599	2.9048	3.1422	5.4936	2.1429	0.9894	9.5751
0.6402	1.6773	6.1764	5.6939	5.3749	1.2903	2.9900	8.2878
1.4546	2.7141	8.2953	3.7439	5.2200	2.4332	1.6431	7.7699
7.0072	1.2478	7.3329	3.4768	3.1542	4.1492	4.6335	7.0017
2.0469	1.0515	2.4412	13.9159	4.2134	2.1695	1.9193	33.7858
1.8032	0.7279	1.6900	10.2339	3.9723	1.8105	2.0981	19.6041
3.7867	0.7432	5.0830	1.6164	4.7796	2.0411	5.4520	0.6001
5.0265	0.6831	3.4568	4.0383	3.3106	3.3818	6.5200	0.2923
$r_1^{(5)}$	$r_2^{(5)}$	$r_3^{(5)}$	$r_4^{(5)}$	$r_5^{(5)}$	$r_6^{(5)}$	$r_7^{(5)}$	$r_8^{(5)}$
1.2599	2.9048	3.1422	5.4936	2.1429	1.0951	3.8036	15.7579
1.6773	6.1764	5.6939	5.3749	1.2903	3.3094	3.2922	15.1594
2.7141	8.2953	3.7439	5.2200	2.4332	1.8186	3.0865	22.0800
1.2478	7.3329	3.4768	3.1542	4.1492	5.1285	2.7813	37.3858
1.0515	2.4412	13.9159	4.2134	2.1695	2.1243	11.5457	53.6971
0.7279	1.6900	10.2339	3.9723	1.8105	2.3222	7.1168	28.0719
0.7432	5.0830	1.6164	4.7796	2.0411	6.0344	8.0126	1.2167
0.6831	3.4568	4.0383	3.3106	3.3818	7.2164	7.2610	0.5138

Table 4.1: Numerical power ratio estimates obtained from 5 AU's for the RR signal in Fig. 4.1; here, each row represents the power ratio vector obtained from an AU.

simply by plotting them. Fig. 4.6 thus gives the plots of the power ratio vectors corresponding to all these 5 AU's, respectively. Using Eq. 4.2 with $n = 5$, one of the resultant ABS evolution estimate \mathbf{r}_{evol} can be found as

$$\mathbf{r}_{evol} = [\mathbf{r}_1^{(1)T} \mathbf{r}_2^{(1)T} \mathbf{r}_3^{(1)T} \mathbf{r}_4^{(1)T} \mathbf{r}_5^{(1)T} \mathbf{r}_6^{(1)T} \mathbf{r}_7^{(1)T} \mathbf{r}_7^{(2)T} \mathbf{r}_7^{(3)T} \mathbf{r}_7^{(4)T} \mathbf{r}_7^{(5)T} \mathbf{r}_8^{(5)T}]^T. \quad (4.3)$$

Or, equivalently,

$$\mathbf{r}_{evol} = [\mathbf{r}_1^{(1)T} \mathbf{r}_2^{(1)T} \mathbf{r}_3^{(1)T} \mathbf{r}_4^{(1)T} \mathbf{r}_5^{(1)T} \mathbf{r}_6^{(1)T} \mathbf{r}_6^{(2)T} \mathbf{r}_6^{(3)T} \mathbf{r}_6^{(4)T} \mathbf{r}_6^{(5)T} \mathbf{r}_7^{(5)T} \mathbf{r}_8^{(5)T}]^T \quad (4.4)$$

$$= [\mathbf{r}_1^{(1)T} \mathbf{r}_2^{(1)T} \mathbf{r}_3^{(1)T} \mathbf{r}_4^{(1)T} \mathbf{r}_5^{(1)T} \mathbf{r}_5^{(2)T} \mathbf{r}_5^{(3)T} \mathbf{r}_5^{(4)T} \mathbf{r}_5^{(5)T} \mathbf{r}_6^{(5)T} \mathbf{r}_7^{(5)T} \mathbf{r}_8^{(5)T}]^T \quad (4.5)$$

$$= [\mathbf{r}_1^{(1)T} \mathbf{r}_2^{(1)T} \mathbf{r}_3^{(1)T} \mathbf{r}_4^{(1)T} \mathbf{r}_4^{(2)T} \mathbf{r}_4^{(3)T} \mathbf{r}_4^{(4)T} \mathbf{r}_4^{(5)T} \mathbf{r}_5^{(5)T} \mathbf{r}_6^{(5)T} \mathbf{r}_7^{(5)T} \mathbf{r}_8^{(5)T}]^T \quad (4.6)$$

$$= [\mathbf{r}_1^{(1)T} \mathbf{r}_2^{(1)T} \mathbf{r}_3^{(1)T} \mathbf{r}_3^{(2)T} \mathbf{r}_3^{(3)T} \mathbf{r}_3^{(4)T} \mathbf{r}_3^{(5)T} \mathbf{r}_4^{(5)T} \mathbf{r}_5^{(5)T} \mathbf{r}_6^{(5)T} \mathbf{r}_7^{(5)T} \mathbf{r}_8^{(5)T}]^T \quad (4.7)$$

$$= [\mathbf{r}_1^{(1)T} \mathbf{r}_2^{(1)T} \mathbf{r}_2^{(2)T} \mathbf{r}_2^{(3)T} \mathbf{r}_2^{(4)T} \mathbf{r}_2^{(5)T} \mathbf{r}_3^{(5)T} \mathbf{r}_4^{(5)T} \mathbf{r}_5^{(5)T} \mathbf{r}_6^{(5)T} \mathbf{r}_7^{(5)T} \mathbf{r}_8^{(5)T}]^T \quad (4.8)$$

$$= [\mathbf{r}_1^{(1)T} \mathbf{r}_1^{(2)T} \mathbf{r}_1^{(3)T} \mathbf{r}_1^{(4)T} \mathbf{r}_1^{(5)T} \mathbf{r}_2^{(5)T} \mathbf{r}_3^{(5)T} \mathbf{r}_4^{(5)T} \mathbf{r}_5^{(5)T} \mathbf{r}_6^{(5)T} \mathbf{r}_7^{(5)T} \mathbf{r}_8^{(5)T}]^T \quad (4.9)$$

Eqs. 4.3– 4.9 give the equivalent estimates of \mathbf{r}_{evol} . In fact, these 7 equations are resulted from the paths (a)–(g) in Fig. 4.7, respectively, used to achieve the same estimates of \mathbf{r}_{evol} . Therefore, the estimate of ABS evolution \mathbf{r}_{evol} can be determined by any one of Eqs. 4.3– 4.9, *i.e.*, by any path in Fig. 4.7. Consequently, in this example the waveform of the ABS evolution was then found and plotted in Fig. 4.8.

Similarly, applying the approach described above to the RR signals given in Figs. 4.2 (ischemic) and 4.3 (normal) we can also find the ABS evolution waveforms for an ischemic and normal episodes, as shown in Figs. 4.9 and 4.10, respectively. Further, observing Figs. 4.8– 4.10 we may get a rough idea in morphological difference between the NSVT and non-NSVT groups, that is, while the ABS waveform generally maintained certain level with no unusual large peaks for either the ischemic or normal, significant spikes can be actually seen in ABS waveform of the NSVT.

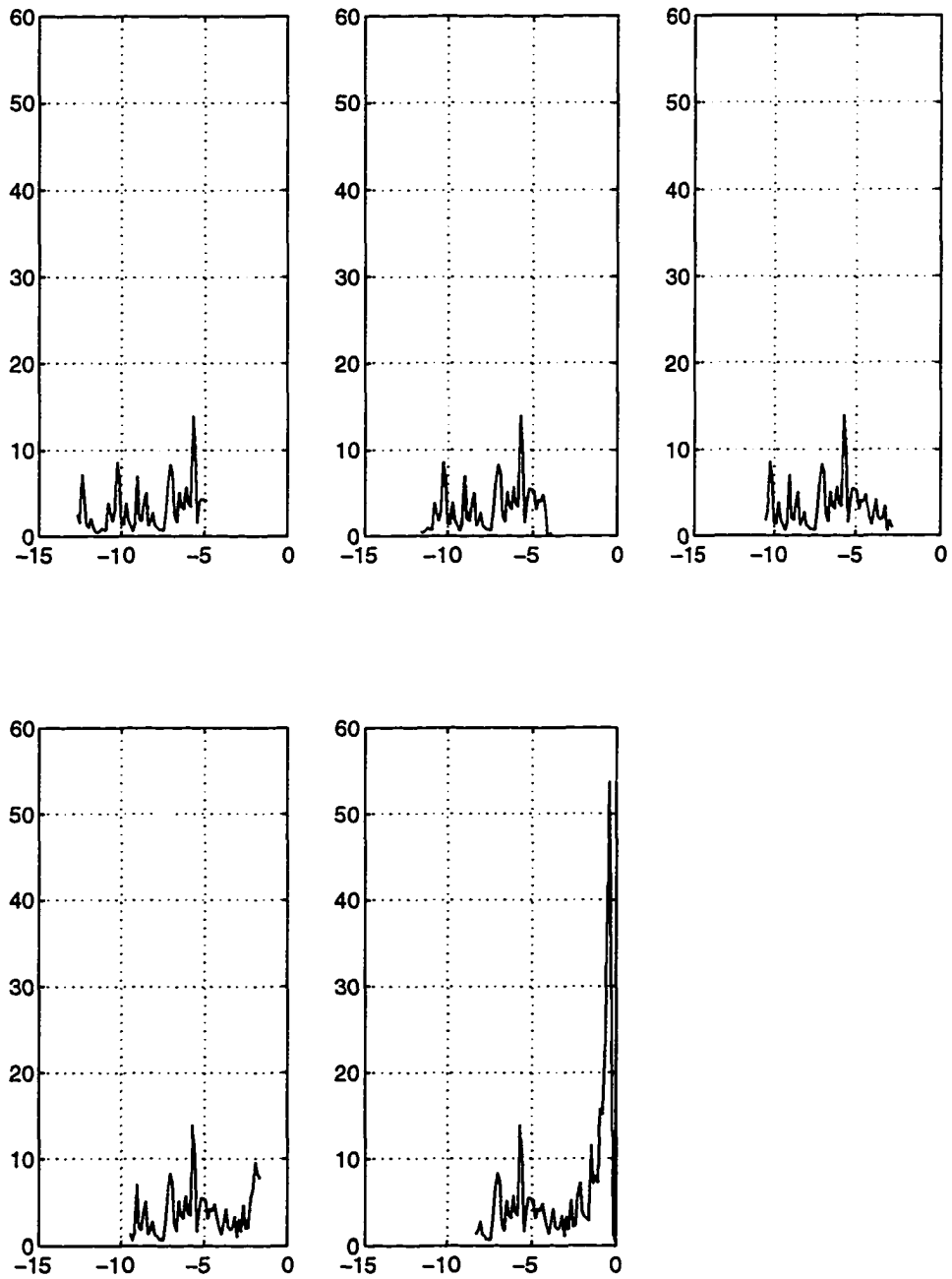


Figure 4.6: The ABS evolutions $([\mathbf{r}_1^{(q)T} \ \mathbf{r}_2^{(q)T} \ \dots \ \mathbf{r}_8^{(q)T}]^T$, for $q = 1, 2, 3, 4, 5$) obtained from all the AU's extracted from an RR signal prior to the occurrence of NSVT (the abscissa represents the time before the onset of NSVT).

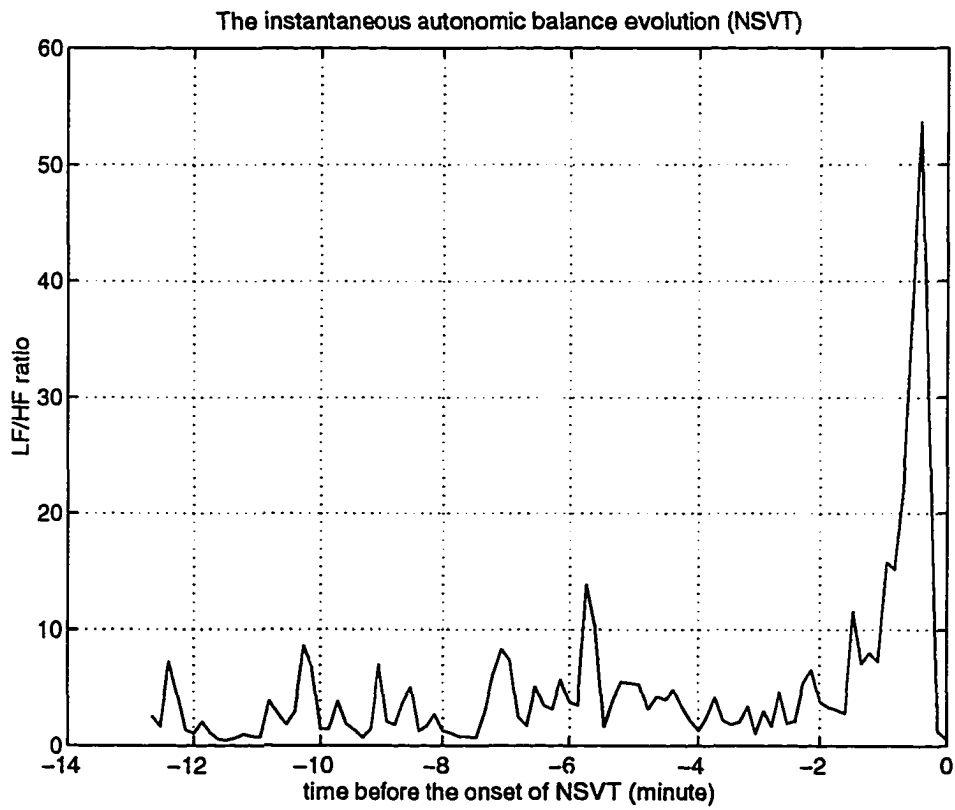


Figure 4.8: The resultant instantaneous ABS evolution for the entire RR signal obtained from Fig. 4.6 (an NSVT episode).

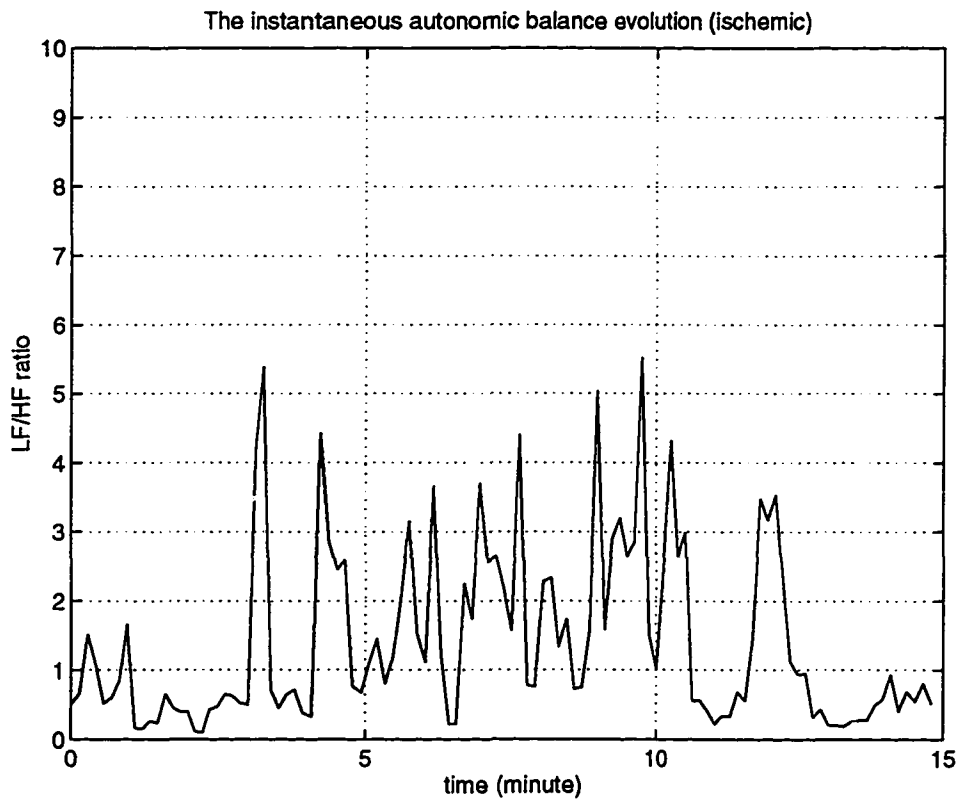


Figure 4.9: The instantaneous ABS evolution obtained from an ischemic episode.

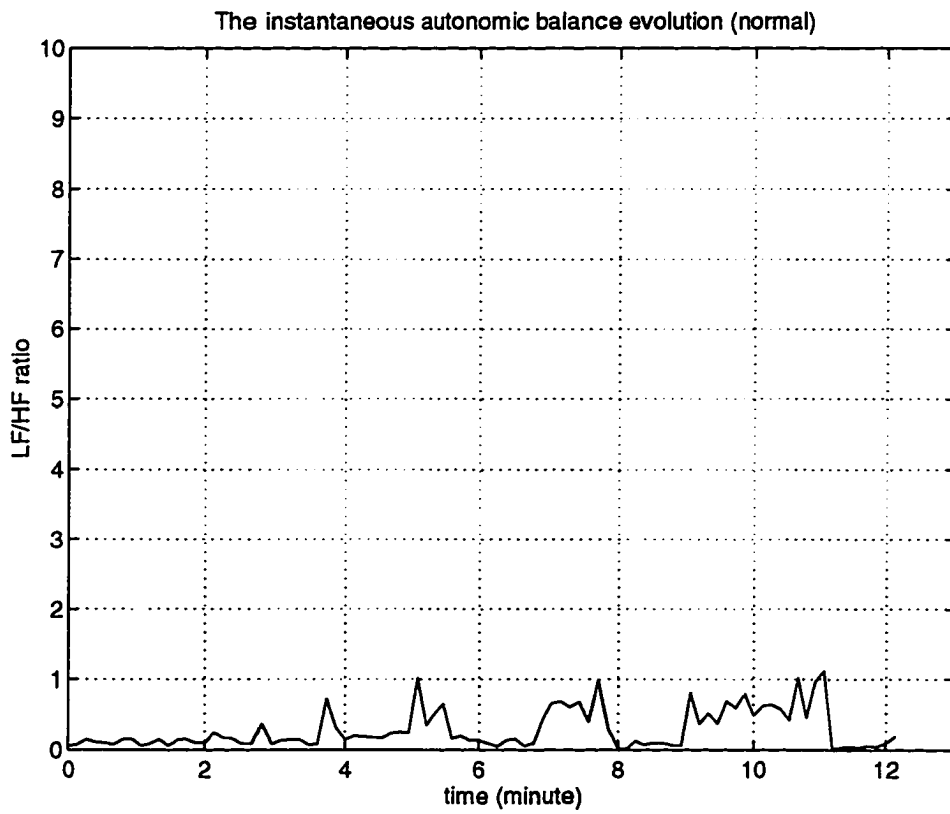


Figure 4.10: The instantaneous ABS evolution obtained from a normal episode.

4.3.3 Morphological Information Indication

Now that \mathbf{r}_{evol} obtained by the above approach can provide an accurate ABS evolution estimate, a careful inspection of the ABS waveform is thus performed next. Since it was described previously that decreased HRV or increased ABS is usually recognized as a long-term predictor of arrhythmic events, we thus postulated that the ABS values would reach the highest or abruptly increase when measured immediately before NSVT. Thus, it is necessary to observe ABS waveforms more closely to see if there were any unusual large values found in the ABS evolution for NSVT. This is because the above phenomenon may imply *abrupt* ANS imbalanced states. Therefore, to decide whether or not an ABS evolution waveform has unusual large ABS values relative to the remaining ones, a *morphological information marker* α used to indicate the information about the behavior of ABS waveform can be thus defined as

$$\alpha = \frac{\overline{\mathbf{r}_{evol} \geq \delta \cdot \max(\mathbf{r}_{evol})}}{\overline{\mathbf{r}_{evol} \leq \delta \cdot \max(\mathbf{r}_{evol})}}, \quad (4.10)$$

where δ represents a fraction factor used for the determination of threshold value. Considering Eq. 4.10, we see that α is quantified as the ratio of the mean value of the entries in \mathbf{r}_{evol} greater than the threshold to that of the entries in \mathbf{r}_{evol} less than the threshold. In fact, a large α would generally imply a trend of more frequent and/or larger power ratio spikes relative to the entire ABS evolution.

An interpretation can be made simply by calculating the values of α for the ABS waveforms as shown in Figs. 4.8– 4.10. The α computations performed on these three \mathbf{r}_{evol} 's are illustrated in Figs. 4.11– 4.13, respectively. Observing these illustrations, we see that once a δ is given, the corresponding threshold, $\delta \cdot \max(\mathbf{r}_{evol})$, is then determined (as shown in the left panels). Consequently, two different probability

distributions can be thus resulted and formed by the ABS values greater than the threshold and by those less than the threshold, respectively (as shown in the right panels). Since α is known as the ratio of the mean values of both distributions (upper to lower), a larger α would indicate a further distance (in decibel) between two distributions, suggesting *relatively* larger ABS values might be found in r_{evol} with higher possibility. Demonstrative examples were given by presenting the results obtained from the α computations illustrated in Figs. 4.11– 4.13. Choosing $\delta = \frac{1}{5}$ empirically, we therefore obtained

$$\alpha \approx 7.7252 \text{ for the NSVT episode;}$$

$$\alpha \approx 5.0085 \text{ for the ischemic episode;}$$

$$\alpha \approx 5.5635 \text{ for the normal episode.}$$

More examples of ABS evolutions and their corresponding α values obtained from NSVT, ischemic and normal episodes were given in Figs. 4.14, 4.15 and 4.16, respectively. From the observations of these instantaneous ABS waveforms, we may see that the ABS evolutions obtained from NSVT episodes seemed to abruptly increase over a 8–20 minute period preceding the onset of NSVT, whereas the same phenomenon could not be seen in those obtained from ischemic and normal episodes. It appeared quite supportive to our postulate. To validate the postulate, however, an inspection on the ABS waveforms for the entire database should be the next essential thing to do. In the following, the morphological information extraction will be performed on the entire database consisting of NSVT, ischemic and normal episodes, towards a statistical significance so the α distributions for the three different types of cardiac conditions may be constructed.

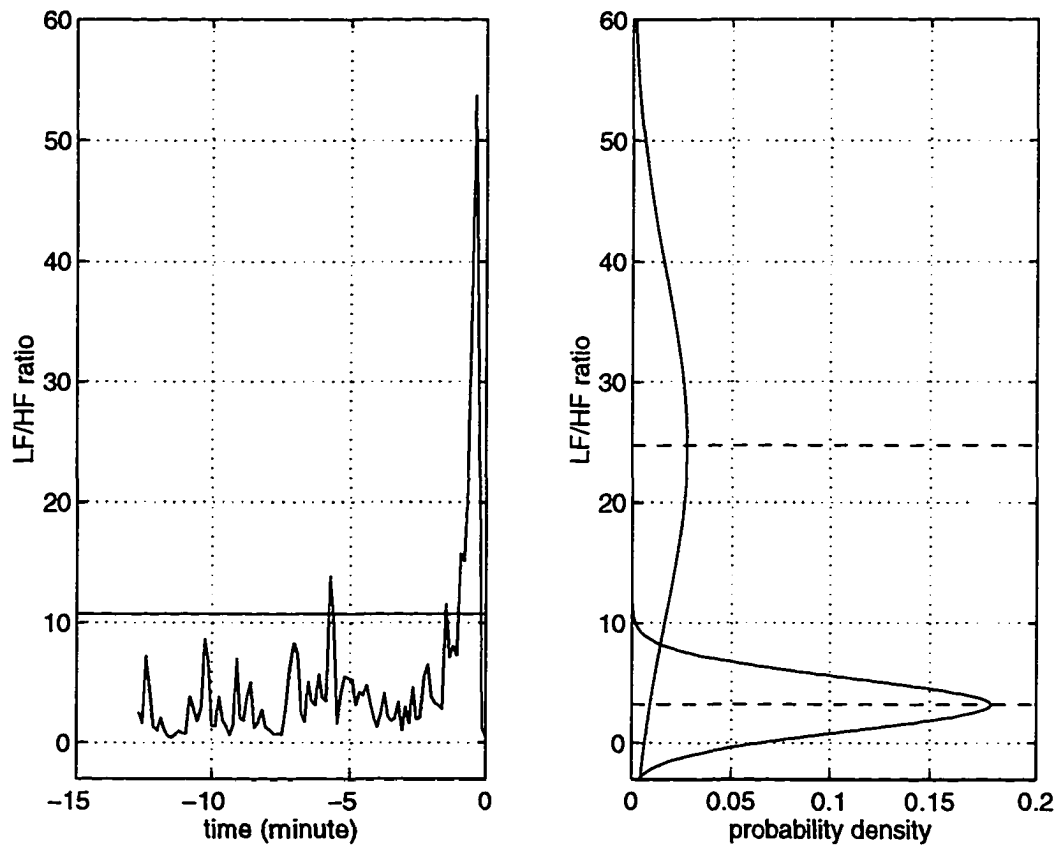


Figure 4.11: Morphological information obtained from the ABS waveform of an NSVT episode: left panel- ABS waveform with the threshold $\delta \cdot \max(\mathbf{r}_{evol})$; right panel- modeled probability density functions resulted from the probability distributions of both groups separated by the threshold; note that dash lines indicate their mean locations.

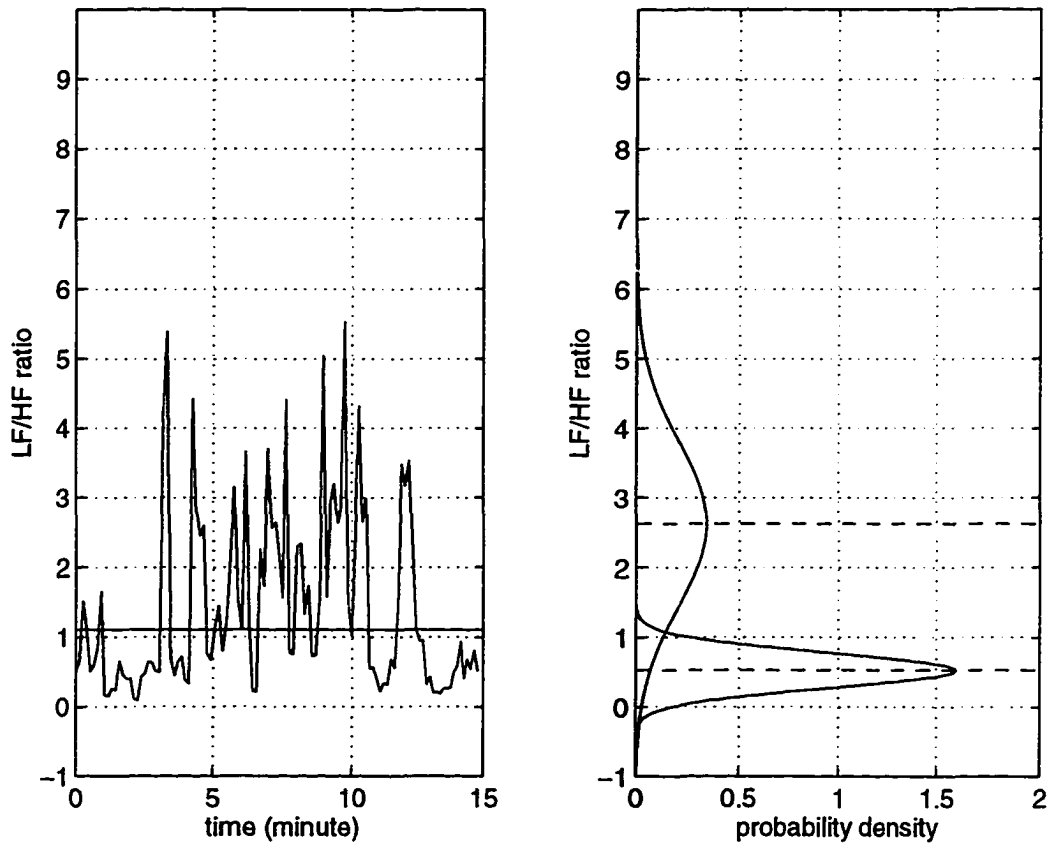


Figure 4.12: Morphological information obtained from the ABS waveform of an ischemic episode: left panel- ABS waveform with the threshold $\delta \cdot \max(\mathbf{r}_{evol})$; right panel- modeled probability density functions resulted from the probability distributions of both groups separated by the threshold; note that dash lines indicate their mean locations.

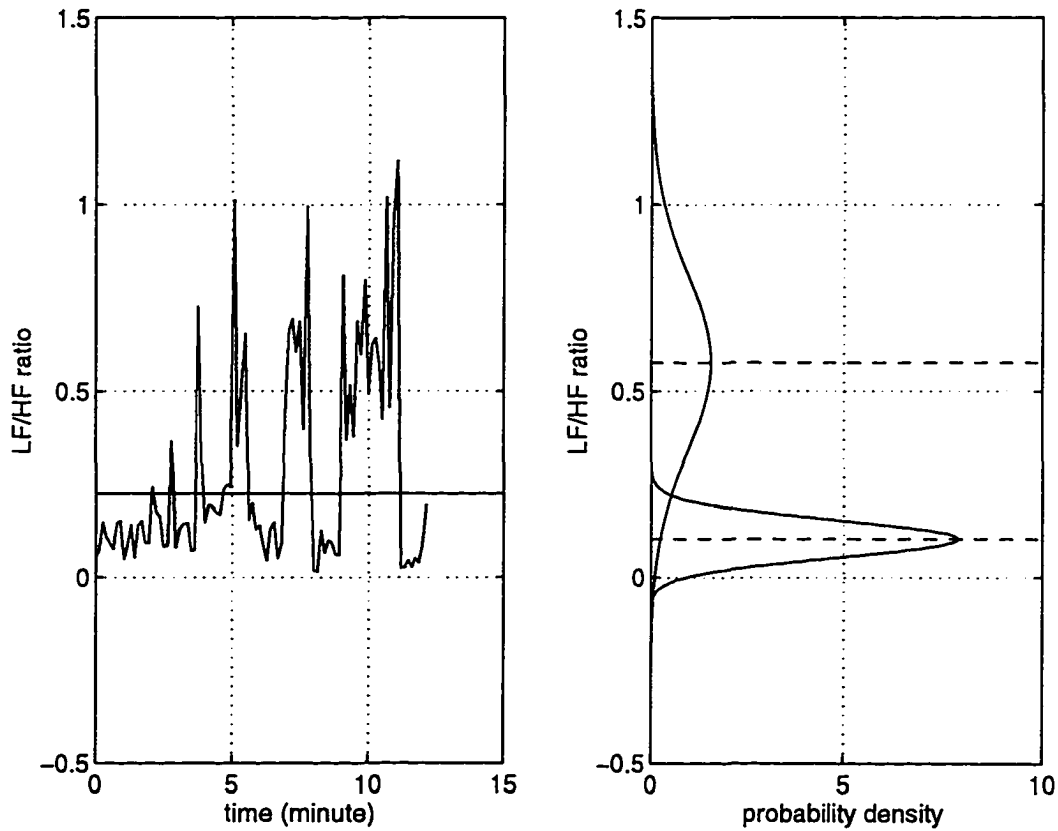


Figure 4.13: Morphological information obtained from the ABS waveform of a normal episode: left panel– ABS waveform with the threshold $\delta \cdot \max(r_{evol})$; right panel– modeled probability density functions resulted from the probability distributions of both groups separated by the threshold; note that dash lines indicate their mean locations.

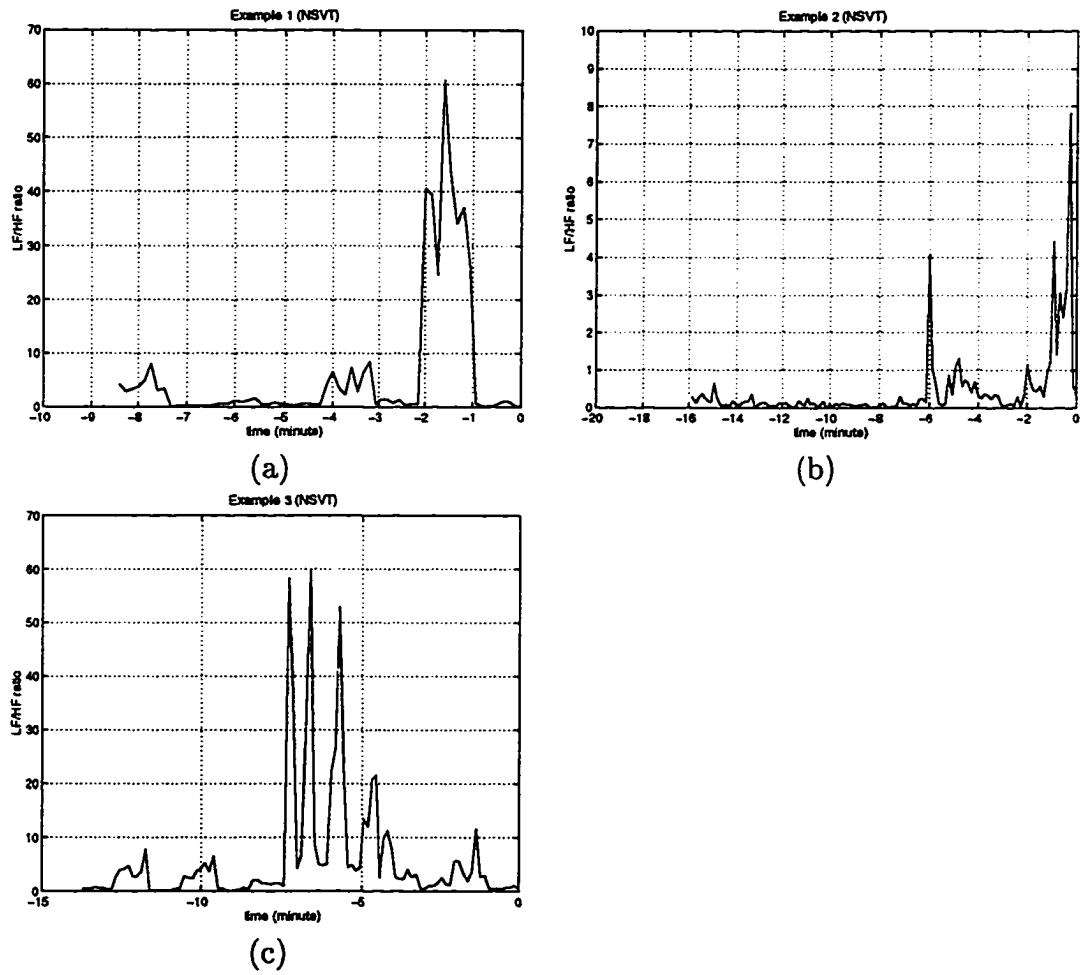


Figure 4.14: Examples of ABS evolutions for NSVT episodes: (a) $\alpha = 21.7873$; (b) $\alpha = 16.4842$; (c) $\alpha = 8.0943$.

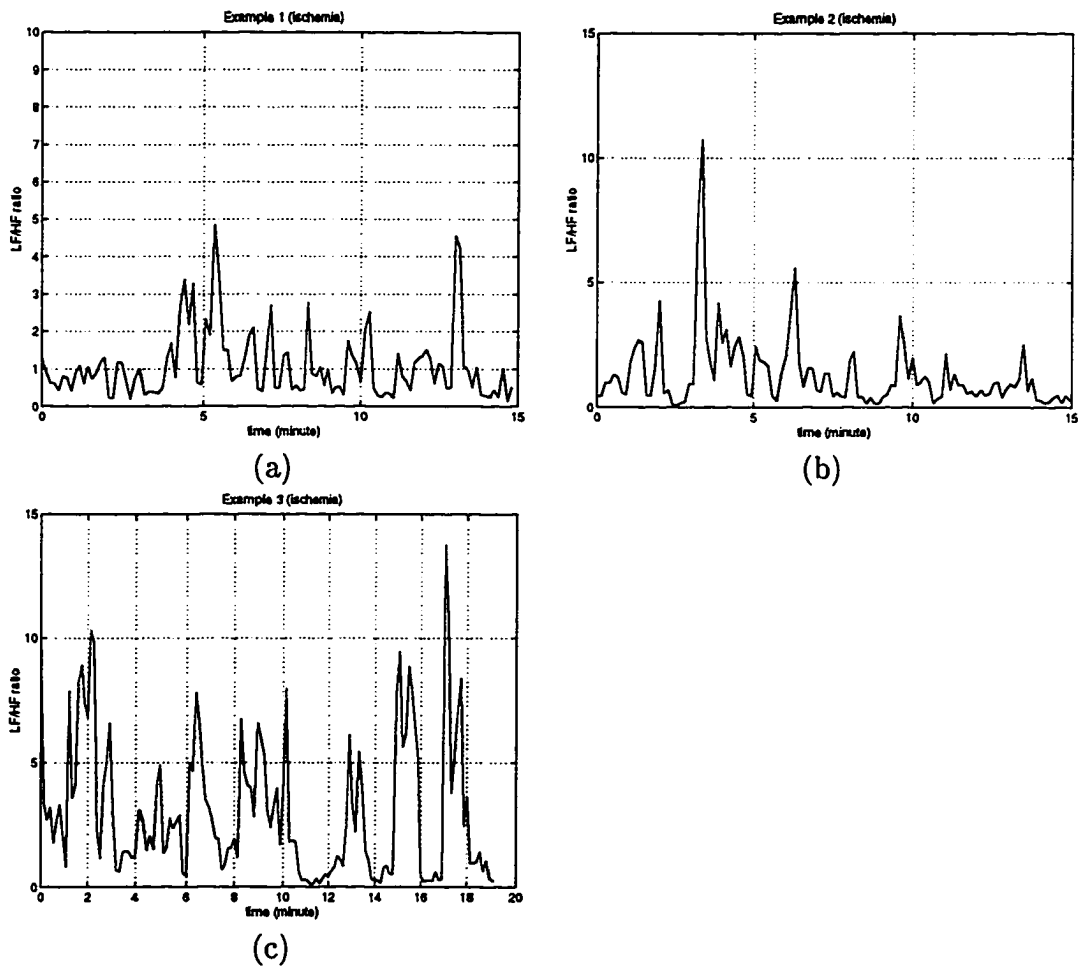
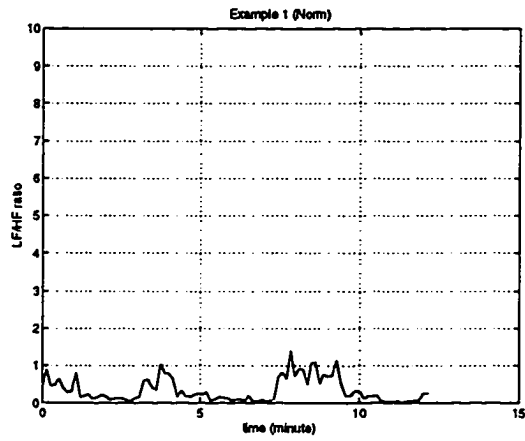
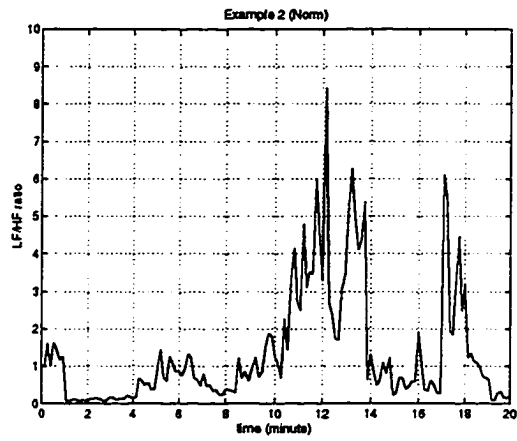


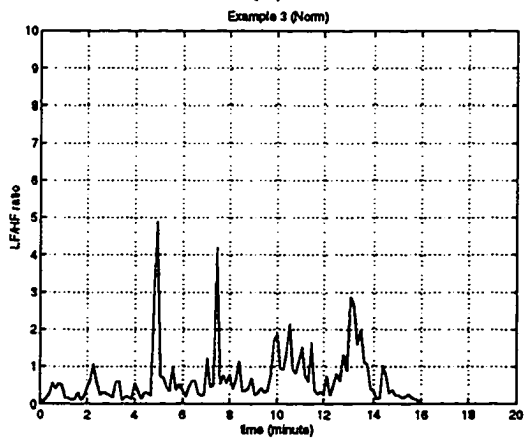
Figure 4.15: Examples of ABS evolutions for ischemic episodes: (a) $\alpha = 3.4921$; (b) $\alpha = 4.4373$; (c) $\alpha = 5.1239$.



(a)



(b)



(c)

Figure 4.16: Examples of ABS evolutions for normal episodes: (a) $\alpha = 5.2610$; (b) $\alpha = 5.9559$; (c) $\alpha = 5.0755$.

4.4 Numerical Experimental Results

This study was formed by 153 episodes. Of the 153 episodes, 87 were NSVT, 61 were ischemic and 5 were normal. We here applied the proposed approach described in last section to all the RR signals in the database. Recall that the LF and HF bands were the same locations as those in validation experiment (*i.e.*, LF=0.03125–0.0625 Hz; HF=0.125–0.5 Hz). The ABS evolutions r_{evol} 's corresponding to all these episodes were then calculated. Considering Figs. 4.8– 4.10 first, we may see that while there were no considerable variations observed in the ABS waveforms obtained from both ischemic and normal episodes (although the averaged ABS value from the ischemic episode appeared to be larger than did that from the normal episode), there were actually significant spikes found in the ABS waveform of the NSVT episode. After inspecting more ABS waveforms for all the three types of cardiac conditions (see Figs. 4.14– 4.16), we may claim that *the ABS evolution seemed to have an abrupt increase over a period several minutes before NSVT rather gradually increased until the onset of NSVT*. To prove or disprove this claim, in addition to simply inspecting the ABS waveforms, a statistical analysis based on the morphological marker α may quantitatively summarize the patterns of ABS evolutions, permitting an α -based pattern recognition on various types of cardiac conditions so the prediction of NSVT may be practically feasible.

4.4.1 Performance: Distributions of α

Now that we calculated the α by using Eq. 4.10 and adopted it to extract the morphological information from r_{evol} , here we would examine its potential ability on detecting or predicting the occurrence of NSVT or more precisely, we would see

if the ABS evolution, “thought” as an initiating factor to precipitate NSVT when significant spikes were detected, can be *morphologically* categorized into the NSVT and non-NSVT classes simply using the marker α . Choosing $\delta = \frac{1}{5}$ as previously, the numerical results of α were then obtained from the entire database. Consequently, the distributions of α for the types of NSVT, ischemic and normal were found as follows:

$$\alpha \sim 10.20 \pm 6.38 \text{ for NSVT type;}$$

$$\alpha \sim 5.79 \pm 2.62 \text{ for ischemic type ;}$$

$$\alpha \sim 5.83 \pm 0.89 \text{ for normal type.}$$

The above statistical results actually indicated that while the distributions of α for both ischemic and normal episodes showed no significant differences, the α values obtained from NSVT generally distributed in a larger and broader scale, as shown in Fig. 4.17. In fact, these results implied that there might exist a trend of more significant ABS spikes relative to the entire ABS waveform found in several minutes (8–20 minutes for this study) before the onset of NSVT, *i.e.*, the ABS values would abruptly increase over a period several minutes before the occurrence of NSVT. Obviously, these results appeared very promising and supportive for our claim.

In addition, according to the results of α distributions in the above (or in Fig. 4.17), it can be readily inferred that an NSVT episode might, in general, be associated with a larger α value. Getting this, we may speculate that α might be able to further serve as a feature or testing parameter used for an investigation on predictability of the occurrence of NSVT. This can be achieved by a hypothesis testing procedure presented in the following section.

4.4.2 Performance: Receiver Operating Characteristic

Classification is the decision-making procedure in pattern recognition. The classification task is alternatively known as detection in communications engineering or hypothesis testing in statistics. Considering the distributions of α given in Fig. 4.17, the decision rule can be designed as a discriminant function in the α space as follows:

$$\begin{aligned}\alpha &\geq \eta \Rightarrow \text{say NSVT;} \\ \alpha &< \eta \Rightarrow \text{say ischemia or normal,}\end{aligned}\tag{4.11}$$

where η is the threshold. Note that η can be derived according to the *Neyman-Pearson criterion*, known as constraining the error probability for one class to a predetermined value c and then designing a test to minimize the other class error probability under this constraint. Denote the error probability for class NSVT as P_{e1} and that for class ischemia as P_{e2} . Also, denote the probability density or distribution of α when class ischemia is true as $p(\alpha | \text{ischemia})$. To satisfy the constraint we chose η so that $P_{e2} = c$, that is,

$$P_{e2} = \int_{\eta}^{\infty} p(\alpha | \text{ischemia})d\alpha = c.\tag{4.12}$$

Solving Eq. 4.12 for η gives the threshold. The value of η given by Eq. 4.12 will be non-negative because $p(\alpha | \text{ischemic})$ is zero for negative values of η . Similarly, P_{e1} can be measured by the expression

$$P_{e1} = \int_0^{\eta} p(\alpha | \text{NSVT})d\alpha,\tag{4.13}$$

where $p(\alpha | \text{NSVT})$ represents the probability density of α when class NSVT is true. Considering both Eqs. 4.12 and 4.13, we may see that P_{e1} decreases and P_{e2} increases

as η decreases. Therefore, to minimize P_{e1} given by Eq. 4.13 we decrease η until the largest possible $P_{e2} = c' \leq c$ is obtained.

Further, we denote the correct probability for classes NSVT and ischemia as P_{c1} and P_{c2} , respectively. Obviously, we have

$$P_{c1} = 1 - P_{e1} = \int_{\eta}^{\infty} p(\alpha | \text{NSVT})d\alpha, \quad (4.14)$$

and

$$P_{c2} = 1 - P_{e2} = \int_0^{\eta} p(\alpha | \text{ischemia})d\alpha. \quad (4.15)$$

Note that $100 \cdot P_{c1}$ and $100 \cdot P_{c2}$ can be also used to represent percentages of detection accuracy for NSVT and ischemia, respectively. Plotting $100 \cdot P_{c1}$ versus $100 \cdot P_{c2}$, we then obtained a plot as shown in Fig. 4.18 (upper left panel). The result in the upper left panel in Fig. 4.18 is referred to as the *receiver operating characteristic* (ROC). Actually, the ROC curve can completely describe the performance of the test as a function of the parameter of interest η [42]. Since P_{c1} and P_{c2} are functions of η , in this figure we also included the plots of $P_{c1}(\eta)$ versus η (upper right panel) and $P_{c2}(\eta)$ versus η (lower left panel). Once an operating point in ROC curve is given, the corresponding value of threshold η can be simply found from either one of $P_{c1}(\eta)$ and $P_{c2}(\eta)$ plots. The ROC of NSVT versus ischemia is also partly listed in Table 4.2. Considering the results in Table 4.2, it was found that while we constrained the percentage of specified ischemia as $100 \cdot P_{c2} \approx 74\%$, the maximal percentage of specified NSVT we obtained was $100 \cdot P_{c1} \approx 73\%$. In addition, this operating point could achieve the optimal overall detection accuracy ($\approx 76\%$). At this time the corresponding threshold value η was ranged from 6.31 to 6.32. Therefore, setting $\eta=6.31-6.32$ we had that 68 out of 87 NSVT episodes appeared to have expectedly

larger α 's greater than the threshold (*i.e.*, 19 false ischemias), whereas 45 of 61 ischemic had expectedly smaller α 's appearing to be less than the threshold (*i.e.*, 16 false NSVT's).

As for the separation between the NSVT and normal, we re-defined P_{e2} and P_{c2} as the error and correct probabilities, respectively, for class normal simply by replacing $p(\alpha | \text{ischemia})$ with $p(\alpha | \text{normal})$ in Eqs. 4.12 and 4.15. Similarly, we plotted the ROC curve in Fig. 4.19 and also listed part of the ROC results in Table 4.3. Considering the results in Table 4.3, it was found that while we constrained the percentage of specified normal as $100 \cdot P_{c2} = 80\%$, the maximal percentage of specified NSVT we obtained was $100 \cdot P_{c1} \approx 82\%$ and this operating point could achieve the optimal overall detection accuracy ($\approx 82\%$). At this time the corresponding threshold value η was ranged from 5.96 to 5.98. However, the performance presented above was obtained solely from the NSVT and normal without inclusion of the ischemia. Since in this research, our concern was mainly on the classification between the presence and absence of NSVT rather than between the ischemia and normal, we thus considered both the ischemia and normal together being in the non-NSVT category. Therefore, only an optimal threshold range was needed. Comparing $\eta = 5.96 \sim 5.98$ with $\eta = 6.31 \sim 6.32$, we see that while both threshold ranges attained 80% of specified normal, the former only allowed 64% of specified ischemia. Considering the *overall* classification, we here chose η in the interval $[6.31, 6.32]$ because this threshold range would allow the constraint of percentage of specified normal (*i.e.*, 80%) to hold and on the other hand, could achieve a much better percentage of specified ischemia as approximate 74% while about 78% of specified NSVT was attained at the same time. Consequently, according to this selected threshold range (*i.e.*, $\eta = 6.31 \sim 6.32$)

we finally obtained the optimal overall classification results as summarized in the following:

overall accuracy	specified NSVT	specified ischemia	specified normal
76.4706%	78.1609%	73.7705%	80.0000%

The performances presented above appeared a very encouraging and hopeful start for the WT-based HRV analysis to the predictability of NSVT. This might provide some evidence to suggest the ANS influence on the precipitation of NSVT. In Chapter 5, we will further evaluate all the numerical performances and then discuss the matter of possible underlying pathophysiological events that might account for the precipitation of NSVT.

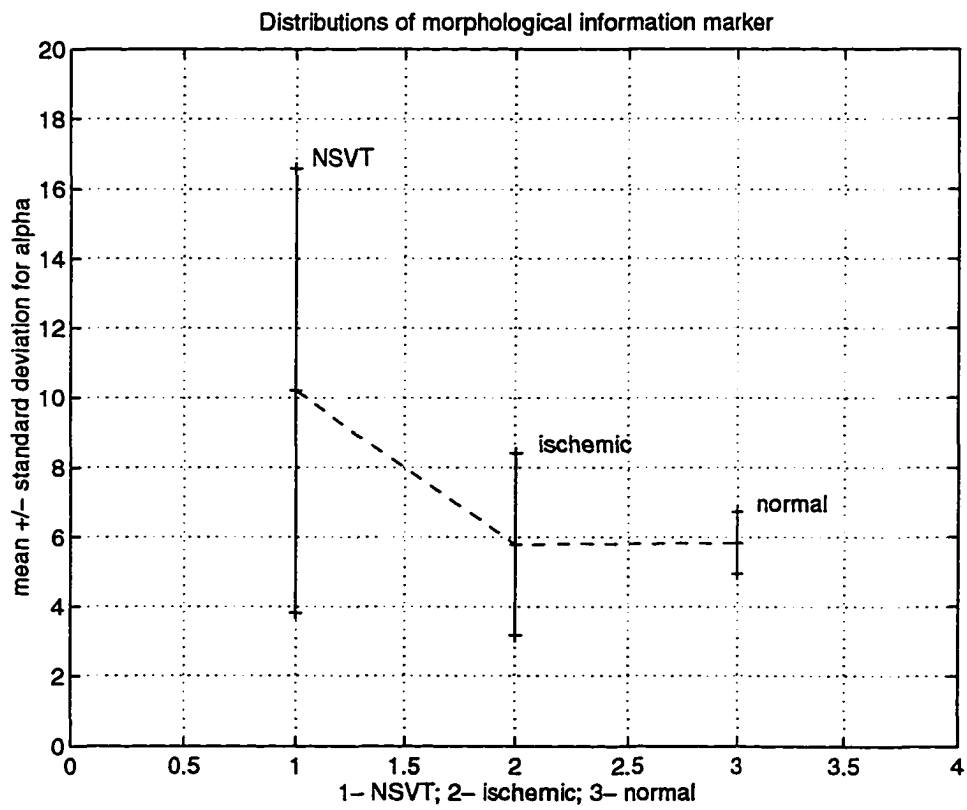


Figure 4.17: Distributions of α obtained from NSVT, ischemic and normal episodes; note that the bars are mean values \pm standard deviations.

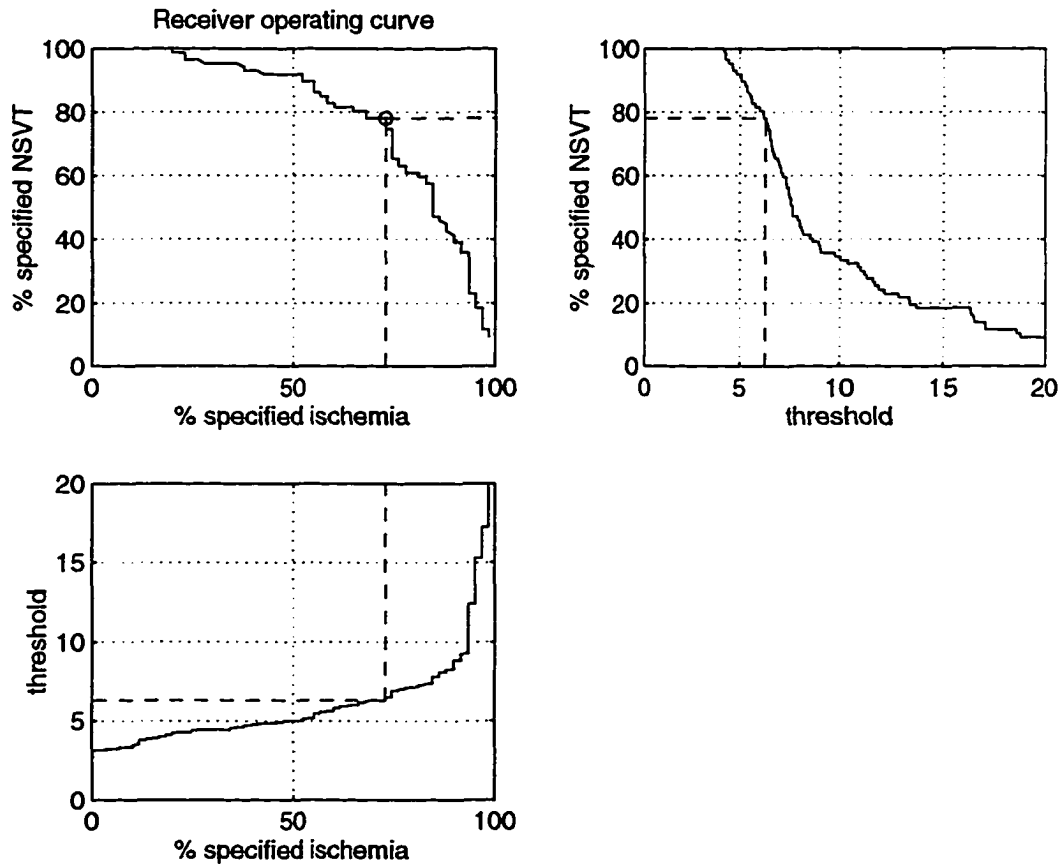


Figure 4.18: Plots of ROC curve for NSVT versus ischemia (upper left panel), percentage of specified NSVT $100 \cdot P_{c1}$ versus threshold η (upper right panel), and percentage of specified ischemia $100 \cdot P_{c2}$ versus threshold η (lower left panel); note that the operating point $100 \cdot (P_{c2}, P_{c1})$ in this ROC curve is (74%, 78%) and the corresponding threshold value is $\eta = 6.31$.

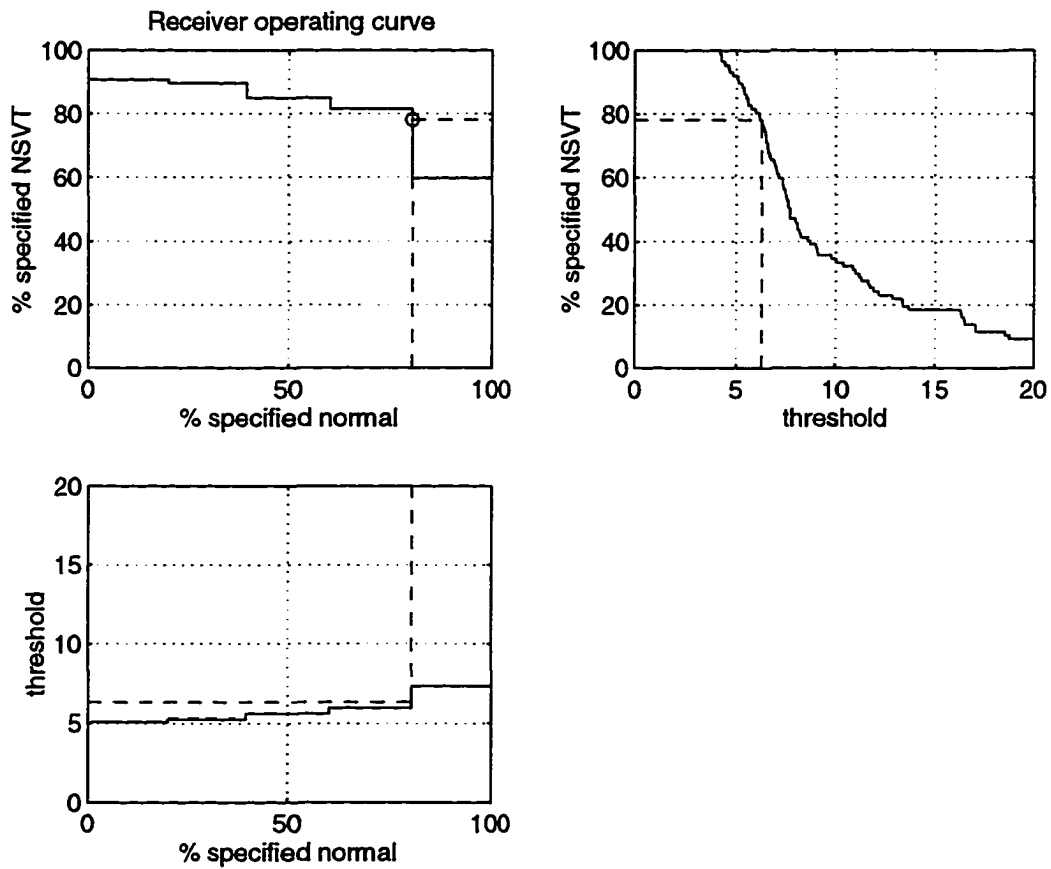


Figure 4.19: Plots of ROC curve for NSVT versus normal (upper left panel), percentage of specified NSVT $100 \cdot P_{c1}$ versus threshold η (upper right panel), and percentage of specified normal $100 \cdot P_{c2}$ versus threshold η (lower left panel); note that the operating point $100 \cdot (P_{c2}, P_{c1})$ in this ROC curve is (80%, 78%) and the corresponding threshold value is $\eta = 6.31$.

η	overall accuracy (%)	$100 \cdot P_{c2}$ (%)	$100 \cdot P_{c1}$ (%)	false NSVT	false ischemia
5.9500	74.3243	63.9344	81.6092	22.0000	16.0000
5.9600	74.3243	63.9344	81.6092	22.0000	16.0000
5.9700	75.0000	65.5738	81.6092	21.0000	16.0000
5.9800	75.0000	65.5738	81.6092	21.0000	16.0000
5.9900	74.3243	65.5738	80.4598	21.0000	17.0000
6.0000	74.3243	65.5738	80.4598	21.0000	17.0000
6.0100	75.0000	67.2131	80.4598	20.0000	17.0000
6.0200	75.0000	67.2131	80.4598	20.0000	17.0000
6.0300	75.0000	67.2131	80.4598	20.0000	17.0000
6.0400	75.0000	67.2131	80.4598	20.0000	17.0000
6.0500	75.0000	67.2131	80.4598	20.0000	17.0000
6.0600	75.0000	67.2131	80.4598	20.0000	17.0000
6.0700	75.0000	67.2131	80.4598	20.0000	17.0000
6.0800	75.0000	67.2131	80.4598	20.0000	17.0000
6.0900	75.0000	67.2131	80.4598	20.0000	17.0000
6.1000	75.0000	67.2131	80.4598	20.0000	17.0000
6.1100	75.0000	67.2131	80.4598	20.0000	17.0000
6.1200	75.0000	67.2131	80.4598	20.0000	17.0000
6.1300	75.0000	67.2131	80.4598	20.0000	17.0000
6.1400	75.0000	67.2131	80.4598	20.0000	17.0000
6.1500	75.0000	67.2131	80.4598	20.0000	17.0000
6.1600	75.0000	67.2131	80.4598	20.0000	17.0000
6.1700	75.0000	67.2131	80.4598	20.0000	17.0000
6.1800	75.6757	68.8525	80.4598	19.0000	17.0000
6.1900	75.0000	68.8525	79.3103	19.0000	18.0000
6.2000	75.0000	68.8525	79.3103	19.0000	18.0000
6.2100	75.0000	68.8525	79.3103	19.0000	18.0000
6.2200	74.3243	68.8525	78.1609	19.0000	19.0000
6.2300	74.3243	68.8525	78.1609	19.0000	19.0000
6.2400	74.3243	68.8525	78.1609	19.0000	19.0000
6.2500	74.3243	68.8525	78.1609	19.0000	19.0000
6.2600	74.3243	68.8525	78.1609	19.0000	19.0000
6.2700	74.3243	68.8525	78.1609	19.0000	19.0000
6.2800	74.3243	68.8525	78.1609	19.0000	19.0000
6.2900	75.6757	72.1311	78.1609	17.0000	19.0000
6.3000	75.6757	72.1311	78.1609	17.0000	19.0000
6.3100	76.3514	73.7705	78.1609	16.0000	19.0000
6.3200	76.3514	73.7705	78.1609	16.0000	19.0000
6.3300	75.6757	73.7705	77.0115	16.0000	20.0000
6.3400	75.6757	73.7705	77.0115	16.0000	20.0000
6.3500	75.6757	73.7705	77.0115	16.0000	20.0000

Table 4.2: Part of ROC in NSVT versus ischemia: column 1– threshold η ; column 2– percentage of overall accuracy; column 3– percentage of specified ischemia; column 4– percentage of specified NSVT; column 5– number of false NSVT; column 6– number of false ischemia.

η	overall accuracy (%)	$100 \cdot P_{c2}$ (%)	$100 \cdot P_{c1}$ (%)	false NSVT	false normal
5.9500	80.4348	60.0000	81.6092	2.0000	16.0000
5.9600	81.5217	80.0000	81.6092	1.0000	16.0000
5.9700	81.5217	80.0000	81.6092	1.0000	16.0000
5.9800	81.5217	80.0000	81.6092	1.0000	16.0000
5.9900	80.4348	80.0000	80.4598	1.0000	17.0000
6.0000	80.4348	80.0000	80.4598	1.0000	17.0000
6.0100	80.4348	80.0000	80.4598	1.0000	17.0000
6.0200	80.4348	80.0000	80.4598	1.0000	17.0000
6.0300	80.4348	80.0000	80.4598	1.0000	17.0000
6.0400	80.4348	80.0000	80.4598	1.0000	17.0000
6.0500	80.4348	80.0000	80.4598	1.0000	17.0000
6.0600	80.4348	80.0000	80.4598	1.0000	17.0000
6.0700	80.4348	80.0000	80.4598	1.0000	17.0000
6.0800	80.4348	80.0000	80.4598	1.0000	17.0000
6.0900	80.4348	80.0000	80.4598	1.0000	17.0000
6.1000	80.4348	80.0000	80.4598	1.0000	17.0000
6.1100	80.4348	80.0000	80.4598	1.0000	17.0000
6.1200	80.4348	80.0000	80.4598	1.0000	17.0000
6.1300	80.4348	80.0000	80.4598	1.0000	17.0000
6.1400	80.4348	80.0000	80.4598	1.0000	17.0000
6.1500	80.4348	80.0000	80.4598	1.0000	17.0000
6.1600	80.4348	80.0000	80.4598	1.0000	17.0000
6.1700	80.4348	80.0000	80.4598	1.0000	17.0000
6.1800	80.4348	80.0000	80.4598	1.0000	17.0000
6.1900	79.3478	80.0000	79.3103	1.0000	18.0000
6.2000	79.3478	80.0000	79.3103	1.0000	18.0000
6.2100	79.3478	80.0000	79.3103	1.0000	18.0000
6.2200	78.2609	80.0000	78.1609	1.0000	19.0000
6.2300	78.2609	80.0000	78.1609	1.0000	19.0000
6.2400	78.2609	80.0000	78.1609	1.0000	19.0000
6.2500	78.2609	80.0000	78.1609	1.0000	19.0000
6.2600	78.2609	80.0000	78.1609	1.0000	19.0000
6.2700	78.2609	80.0000	78.1609	1.0000	19.0000
6.2800	78.2609	80.0000	78.1609	1.0000	19.0000
6.2900	78.2609	80.0000	78.1609	1.0000	19.0000
6.3000	78.2609	80.0000	78.1609	1.0000	19.0000
6.3100	78.2609	80.0000	78.1609	1.0000	19.0000
6.3200	78.2609	80.0000	78.1609	1.0000	19.0000
6.3300	77.1739	80.0000	77.0115	1.0000	20.0000
6.3400	77.1739	80.0000	77.0115	1.0000	20.0000
6.3500	77.1739	80.0000	77.0115	1.0000	20.0000

Table 4.3: Part of ROC in NSVT versus normal: column 1- threshold η ; column 2- percentage of overall accuracy; column 3- percentage of specified normal; column 4- percentage of specified NSVT; column 5- number of false NSVT; column 6- number of false normal.

CHAPTER 5

PERFORMANCE EVALUATION AND CLINICAL IMPLICATIONS

In this study, short-term HRV measures reflected by the ABS evolutions over a 8–20 minute period preceding the NSVT and those over a 8–20 minute period for ischemic and normal episodes were examined. As described in Chapter 4 the numerical results suggested that there might exist a trend of abruptly increased ABS values observed in the NSVT rather the ischemic or normal and also, the classification task can be then performed by a morphological information marker α . In general, α values measured from the NSVT episodes appeared to be larger than that measured from the ischemic or normal ones. In this chapter, we further evaluated the performance by investigating the underlying pathophysiological significance and its potential clinical implications revealed by the resultant observations such as α values, time-varying LF and HF powers mentioned in Chapter 4.

5.1 Underlying Pathophysiological Significance

5.1.1 Factors of Sympathetic Predominance in NSVT

It has been known that spectral analysis of HRV is able to partly distinguish sympathetic from vagal activity driven to the heart. While the power of LF components

gives a measure of sympathetic activity with some influence from parasympathetic activity, that of HF components is almost exclusively modulated by parasympathetic activity. Therefore, the LF/HF ratio can be used as an index of the sympathovagal balance (or ABS) of the heart [67, 73, 85]. By employing such an ABS index measured based on WT method, our numerical results have demonstrated that an alternation of HRV (*i.e.*, an increased sympathovagal balance) during the last several (8–20) minutes prior to the onset of NSVT episodes might be more relevant to the pathogenesis of ventricular arrhythmias.

In fact, an increased ABS values suggests a sympathetic predominance that may be resulted from an increased sympathetic or a decreased parasympathetic activity to the heart, or both. To seek for a more effective drug therapy or treatment strategy to suppress this undesired sympathovagal imbalance that might precipitate the NSVT, a question thus arises. That is, which nervous fiber (sympathetic or parasympathetic) plays a more important or predominant role in the modulation of such an abnormal cardiac activity leading to this resultant sympathetic predominance? To answer this question, we employed the LF power as an index of cardiac sympathetic drive and HF power as that of vagal drive to the heart. Then, a classification task was performed simply using the α calculated from LF or from 1/HF waveform *alone* instead of using LF/HF (or ABS) waveform. Thus, a larger α obtained from LF waveform should indicate an unusual increased cardiac sympathetic activity, whereas that obtained from 1/HF waveform would imply a trend of an abruptly reduced cardiac vagal drive.

Now, considering both the LF- and HF-based classification tasks, we may speculate that the one resulting in a higher predictive accuracy for the NSVT, with a fixed constraint of predictive accuracy for the non-NSVT, might suggest a more significant

role played by the nervous fiber to which it corresponds in the modulation of cardiac autonomic activities. For instance, if the LF-based classification result attained a better percentage of identified NSVT than did the HF-based classification when the percentage of identified non-NSVT remained unchanged, then it could be said that the sympathetic activity contributed more to the sympathovagal imbalance than did the vagal tone. Figs. 5.1 and 5.2 show the ROC curves obtained from the classification tasks performed solely by the increased-sympathetic index (LF) and by the decreased-parasympathetic index ($1/HF$), respectively. Observing both figures, we see that while the detection accuracy of non-NSVT (ischemic and normal) was constrained to 62%, the LF component-related (or sympathetic-related) abnormality of autonomic influence on the heart over a 8–20 minute period immediately preceding the onset of NSVT achieved only a bit higher predictive accuracy of NSVT (63%) than did the HF component-related (or vagal-related) one (61%). The classification results above suggested that the increased cardiac sympathetic activity might be non-significantly predominant over a reduced vagal drive to the heart for the precipitation of NSVT. Or we may say that there were no significant differences between the abnormalities due to an increased sympathetic or a decreased vagal activity to cause the occurrence of the NSVT.

In addition to performing the classification separately, we also computed correlation coefficients between ABS evolution r_{evol} and LF power waveform, and between r_{evol} and inverse HF power waveform, respectively, for each NSVT episode. The reason for introducing the correlation coefficient computation was that since our results indicated that the information revealed by the waveform of r_{evol} provided a very useful feature for the prediction of NSVT, an inspection of the associations between r_{evol}

and LF power variations, and between r_{evol} and inverse HF power variations might be helpful to getting a “general idea” of the compositions in the sympathovagal balance status respectively contributed by the increased-sympathetic and decreased-vagal activities. Denote the variables ABS, increased-sympathetic and decreased-vagal as r (with variances σ_r^2), s (with variances σ_s^2) and v^{-1} (with variances $\sigma_{v^{-1}}^2$), respectively. Further denote the correlation coefficient between r and s as ρ_{rs} and that between r and v^{-1} as $\rho_{rv^{-1}}$. We have

$$\rho_{rs} = \frac{E\{(r - E\{r\})(s - E\{s\})\}}{\sqrt{\sigma_r^2 \sigma_s^2}}, \quad (5.1)$$

and

$$\rho_{rv^{-1}} = \frac{E\{(r - E\{r\})(v^{-1} - E\{v^{-1}\})\}}{\sqrt{\sigma_r^2 \sigma_{v^{-1}}^2}}. \quad (5.2)$$

Let $\{r_1, r_2, \dots, r_N\}$, $\{s_1, s_2, \dots, s_N\}$ and $\{v_1^{-1}, v_2^{-1}, \dots, v_N^{-1}\}$ be N measurements on the variables r , s and v^{-1} , respectively, ρ_{rs} and $\rho_{rv^{-1}}$ are thus estimated by *sample correlation coefficients* in forms as

$$\hat{\rho}_{rs} = \frac{\frac{1}{N-1} \sum_{i=1}^N (r_i - \bar{r})(s_i - \bar{s})}{\sqrt{\frac{1}{N-1} \sum_{i=1}^N (r_i - \bar{r})^2} \sqrt{\frac{1}{N-1} \sum_{i=1}^N (s_i - \bar{s})^2}}, \quad (5.3)$$

and

$$\hat{\rho}_{rv^{-1}} = \frac{\frac{1}{N-1} \sum_{i=1}^N (r_i - \bar{r})(v_i^{-1} - \bar{v}^{-1})}{\sqrt{\frac{1}{N-1} \sum_{i=1}^N (r_i - \bar{r})^2} \sqrt{\frac{1}{N-1} \sum_{i=1}^N (v_i^{-1} - \bar{v}^{-1})^2}}. \quad (5.4)$$

The sample correlation coefficient is a standardized version of the sample covariance, where the product of the square roots of the sample variances provides the standardization [55]. The correlation coefficient is ordinarily convenient to interpret the association between two variables because its magnitude is *bounded* from -1 to $+1$. To summarize, a correlation coefficient ρ has the property as follows. ρ measures the

strength of the linear association. If $\rho = 0$, this implies a lack of linear association between the two variables. Otherwise, the sign of ρ indicates the direction of the association: $\rho < 0$ implies a tendency for one value in the pair to be larger than its average when the other is smaller than its average; $\rho > 0$ implies a tendency for one value of the pair to be large when the other is larger and also, for both values to be small together.

Therefore, using Eqs. 5.3 and 5.4 we calculated the sample correlation coefficients $\hat{\rho}_{rs}$ and $\hat{\rho}_{rv^{-1}}$ for each one of the 87 NSVT episodes to examine the associations between r and s , and between r and v^{-1} . After that, we first took the mean values of $\hat{\rho}_{rs}$'s and $\hat{\rho}_{rv^{-1}}$'s, respectively, over these 87 NSVT episodes and then obtained $\overline{\hat{\rho}_{rs}} \approx 0.6140$ and $\overline{\hat{\rho}_{rv^{-1}}} \approx 0.5591$, suggesting that the association between r and s might be generally a little *stronger* than that between r and v^{-1} . That is, the results indicated that the increased-sympathetic components, in average, might contribute more to the ABS waveform that precipitated the NSVT than did the decreased-vagal components.

Further, considering the $\hat{\rho}_{rs}$ and $\hat{\rho}_{rv^{-1}}$ for each NSVT episode individually we also found that there were 51 out of the 87 (about 59%) NSVT episodes showing that $\hat{\rho}_{rs} > \hat{\rho}_{rv^{-1}}$, whereas only 36 out of the 87 (about 41%) NSVT episodes appeared that $\hat{\rho}_{rs} < \hat{\rho}_{rv^{-1}}$. Or, according to the numerical results presented in Chapter 4, for those 68 NSVT episodes that could be correctly classified by larger α values, while 40 out of these 68 (about 59%) NSVT episodes showed that $\hat{\rho}_{rs} > \hat{\rho}_{rv^{-1}}$, only 28 out of the 68 (about 41%) NSVT episodes appeared that $\hat{\rho}_{rs} < \hat{\rho}_{rv^{-1}}$. This can be viewed as during the last several (8–20) minutes when there was an increased LF/HF ratio for the NSVT episodes, approximate 59% in this NSVT population

had a predominantly increased-sympathetic activity, whereas only about 41% was from a stronger decreased-vagal activity. As a result, we might conclude that an increased-sympathetic drive to the heart probably had a propensity of serving as a more important role in sympathetic predominance prior to the occurrence NSVT than did a decreased-vagal drive although the results obtained above indicated that differences between the two modulations were not very significant (59% versus 41%).

It should be noted that the quantities $\hat{\rho}_{rs}$, $\hat{\rho}_{rv}$ do not, in general, convey all there is to know about the association between two variables. Nonlinear associations that are not revealed by these descriptive statistics. Covariance and correlation provide measures of *linear* association, or association along a line. Their values are less informative for other kinds of association. On the other hand, these quantities can be very sensitive to “wild” observations (outliers) and may indicate association when, in fact, little exists. In spite of these shortcomings, correlation coefficient is routinely calculated and analyzed. It provides cogent numerical summary of association when the data do not exhibit obvious nonlinear patterns of association or wild observations are not present.

To sum up, our results revealed that no matter which modulation (*i.e.*, increased-sympathetic or decreased-parasympathetic activity) contributed more to the sympathetic predominance for precipitation of NSVT), the sympathovagal interaction may play the most important role in the modulation of normal cardiac activities and in the pathogenesis of ventricular tachyarrhythmias than sympathetic or parasympathetic alone. Therefore, the LF/HF ratio may be of greater clinical significance than either the LF or HF components of HRV.

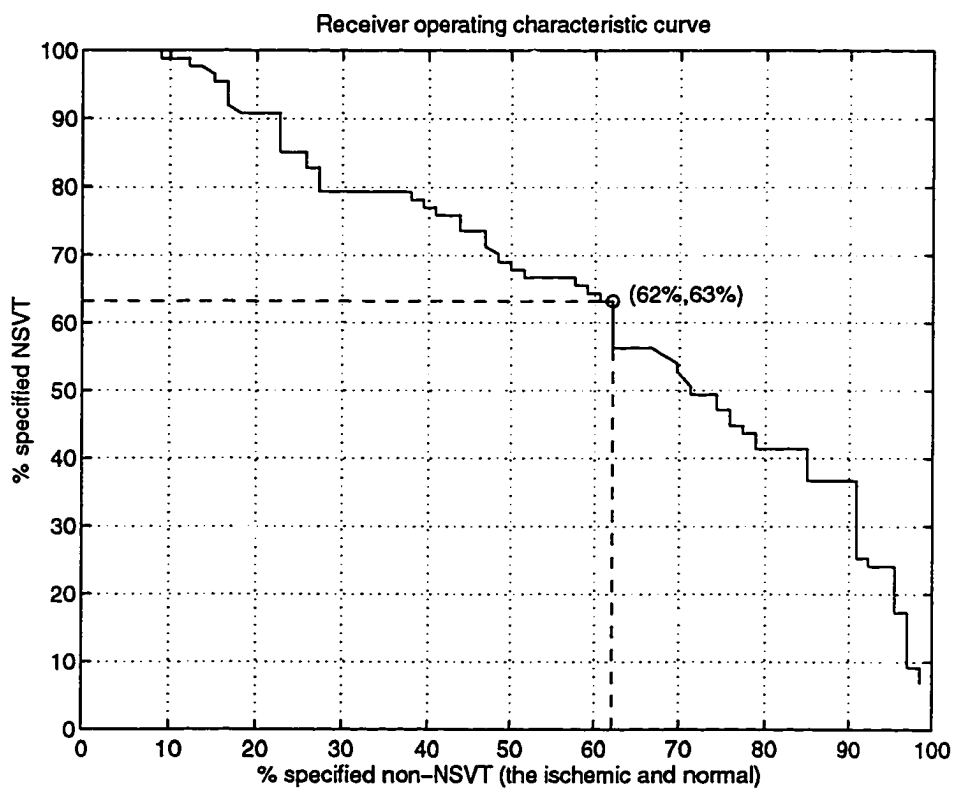


Figure 5.1: The ROC curve of LF-based (*i.e.*, increased-sympathetic based) classification formed by the percentage of identified NSVT versus that of identified non-NSVT (ischemic and normal). Here, the optimal operating point in this ROC curve is (non-NSVT, NSVT) = (62%, 63%).

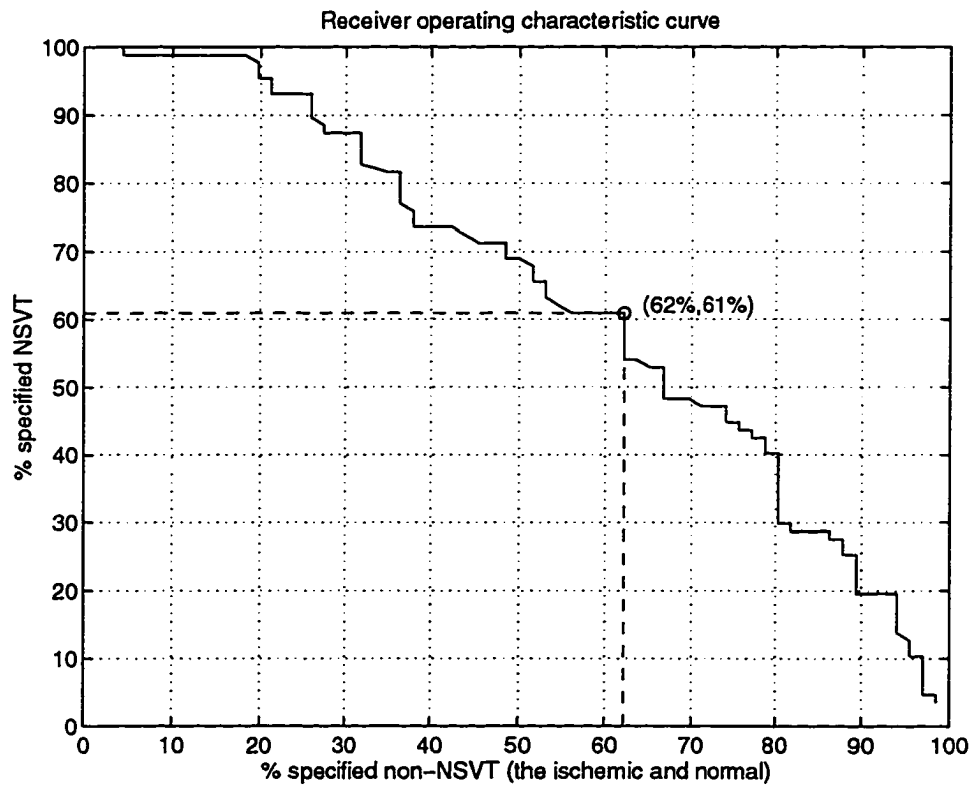


Figure 5.2: The ROC curve of HF-based (*i.e.*, decreased-parasympathetic based) classification formed by the percentage of identified NSVT versus that of identified non-NSVT (ischemic and normal). Here, the optimal operating point in this ROC curve is (non-NSVT, NSVT) = (62%, 61%).

5.1.2 Relation between Clinical Variables and α in NSVT

It was reported that HRV may be significantly related to other clinical variables or risk factors such as *left ventricular ejection fraction* (LVEF) and the angiographic severity of CAD and so on. Several investigations have demonstrated that HRV is most strongly associated with LVEF in patients following acute MI, as well as in patients with *congestive heart failure* (CHF). However, it seems that there is no significant association between HRV and left ventricular function in normal subjects and in patients without reduced cardiac function. Despite the relationship between HRV and the above mentioned clinical variables, the predictive value of depressed HRV is independent of some well established prognostic predictors, including the Holter monitoring features, signal-averaged ECG and LVEF [24, 59, 86]. That is, impaired HRV, late potentials, frequent and repetitive VPB's, and decreased LVEF were identified as significant univariate predictors of arrhythmic events [35].

Note that in some studies comparing risk stratification by signal-averaged ECG and Holter with noninvasive assessment of left ventricular function, LVEF remains an important parameter [64]. In fact, LVEF is one of the best predictors of cardiac mortality in patients with CAD, particularly after an acute MI [50, 82, 93]. Similarly, in patients with CAD and NSVT, the degree of left ventricular dysfunction is among the most powerful predictors outcome [12, 45, 100, 103, 104]. Therefore, left ventricular function should be assessed in all patients with NSVT by employing the parameter LVEF. On the other hand, since the results of this dissertation research suggested that a larger value of morphological feature α measured in the 8–20 minute period preceding the onset of NSVT episodes might precisely predict the occurrence of NSVT, we thus seek for a relationship, if there is any, between α and LVEF to

see if/how LVEF contributes or influences on the precipitation of NSVT. Knowing that modeling refers to the development of mathematical expressions that describe in some sense of the behavior of a variable of interest, a linear regressive modeling analysis was thus introduced in this aspect of application.

patient no.	gender	age	LVEF (%)	$\bar{\alpha}$
1	M	60	30	9.0145
2	M	48	30	9.0772
3	M	58	20	12.2985
4	M	62	20	8.1611
5	M	48	40	10.1277
6	M	61	45	5.8094
7	F	49	18	9.5699
8	M	60	45	6.1135

Table 5.1: Demographic data including the gender, age and LVEF for a subset of the NSVT patients in our database; the subset contained 8 patients since only their demographic data were available. Note that all these NSVT patients had CAD.

Table 5.1 provides a list of demographic data composed of the gender, age, LVEF and averaged value of α , denoted as $\bar{\alpha}$, for a subset of the NSVT patients in our database. In fact, the subset consisted of only 8 patients since they were the ones whose demographic data, especially LVEF measures, were available. Also, all the NSVT patients in our database had CAD. Assume that the observations on the *dependent variable*, α_i , are random observations from populations of random variables with the mean of each population given by $E\{\alpha_i\}$. The deviation of an observation α_i from its population mean $E\{\alpha_i\}$ is taken into account by adding a random error e_i to give the statistical model as

$$\alpha_i = c_0 + c_1 \cdot \text{LVEF}_i + e_i, \quad (5.5)$$

where the subscript i indicates the particular observational unit ($i = 1, 2, \dots, 8$). The $LVEF_i$ are the 8 observations on the *independent variable* and are assumed to be a set of known constants. The random errors, e_i , have *zero mean* and are assumed to have *common* variance σ^2 and to be pairwise independent. Since the only random element in the model is e_i , these assumptions imply that the α_i also have common variance σ^2 and are pairwise independent. The assumptions about e_i are frequently described as “normally, identically and independently distributed,” *i.e.*,

$$e_i \sim N(0, \sigma^2) \quad (5.6)$$

and

$$\alpha_i \sim N(E\{\alpha_i\}, \sigma^2). \quad (5.7)$$

The simple linear model described in Eq. 5.5 has two parameters, c_0 and c_1 , which are to be estimated from the data. Let \hat{c}_0 and \hat{c}_1 be numerical estimates of c_0 and c_1 , respectively, and let

$$\hat{\alpha}_i = \hat{c}_0 + \hat{c}_1 \cdot LVEF_i \quad (5.8)$$

be the *estimated mean* of α_i for each $LVEF_i$, $i = 1, 2, \dots, 8$. The least squares principle chooses \hat{c}_0 and \hat{c}_1 that minimize sum of squares of the residuals, Q :

$$Q = \sum_{i=1}^8 e_i^2 = \sum_{i=1}^8 (\alpha_i - c_0 - c_1 \cdot LVEF_i)^2. \quad (5.9)$$

A minimization on Eq. 5.9 will result in *normal equations* [31, 90] as

$$\frac{\partial Q}{\partial c_0} = -2 \sum_{i=1}^8 (\alpha_i - c_0 - c_1 \cdot LVEF_i) \quad (5.10)$$

and

$$\frac{\partial Q}{\partial c_1} = -2 \sum_{i=1}^8 (\alpha_i - c_0 - c_1 \cdot LVEF_i) \cdot LVEF_i. \quad (5.11)$$

In this study, solving the normal equations in Eqs 5.10 and 5.11 simultaneously for \hat{c}_0 and \hat{c}_1 gives the estimates of c_0 and c_1 as

$$\hat{c}_0 \approx 12.6022 \quad \text{and} \quad \hat{c}_1 \approx -0.1236,$$

respectively. The least squares regression equation characterizing the effects of LVEF on the mean α in this study, assuming the linear model is correct, is

$$\hat{\alpha}_i = 12.6022 - 0.1236 \cdot \text{LVEF}_i. \quad (5.12)$$

Fig. 5.3 shows this linear relation between LVEF and α . The interpretation of $\hat{c}_1 = -0.1236$ is that the mean α is expected to *decrease* by 0.1236 with each 1% increase in LVEF. Note that the observed range of LVEF in the experiment was from 18% to 45% for NSVT patients. Therefore, it would be an unreasonable extrapolation to expect this rate of decrease in α to continue if LVEF levels were to increase. It is safe to use the results of regression only within the range of values of the independent variable LVEF.

Another measure of the contribution of the independent variable in the model is referred to as the *coefficient of determination*, denoted by R^2 [90]. Actually, R^2 ranges from zero to one and it is also identical to the *square* of the correlation coefficient between α_i and LVEF_i if there is only one independent variable. For this study, we have $R^2 \approx 0.4325 \approx 43\%$. That is, only approximate 43% of the variation in the dependent variable α was “explained” by its linear relationship with the independent variable LVEF. On the other hand, recall the Eqs. 5.3– 5.4, we also found that the correlation coefficient between α and LVEF was $\rho \approx -0.6577$. As a result, we see that either the linear regression model-fitting or the correlation coefficient can reflect an *inversely* linear association between the LVEF and the morphological indicator α for

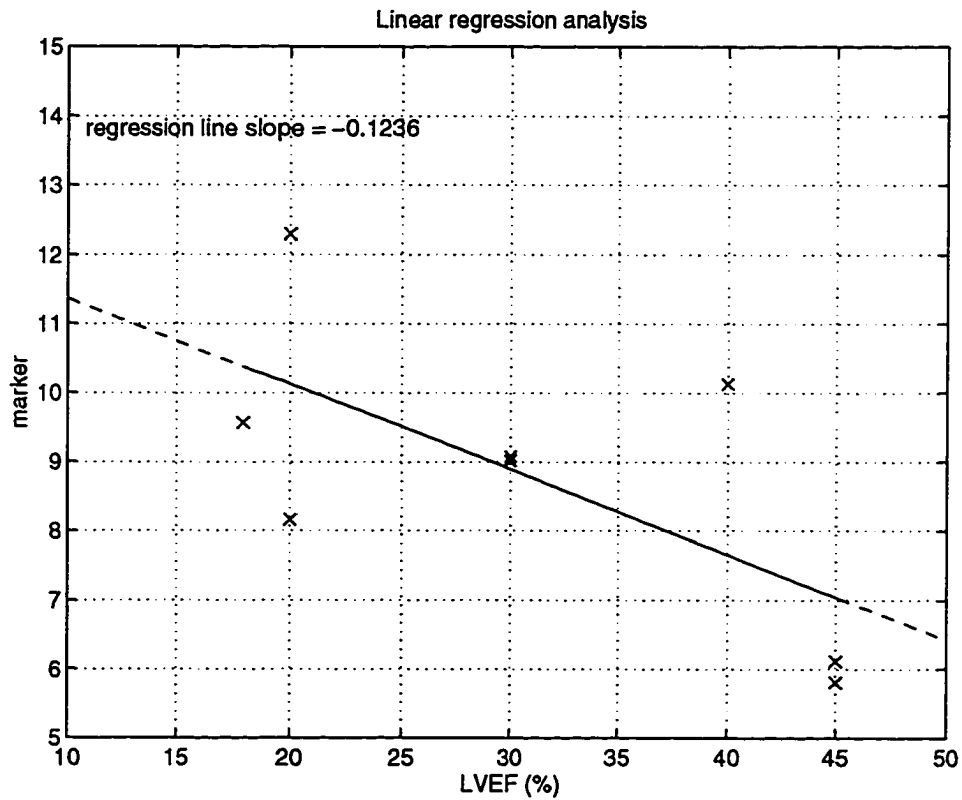


Figure 5.3: A linear regression analysis was performed on the morphological information marker α versus the LVEF for the NSVT patients; the regression line with a negative slope was also included in the scatter plot. Note that the correlation coefficient between the two variables in this application was $\rho \approx -0.66$.

the NSVT, implying that there might exist a relationship between the left ventricular function and presence or precipitation of the NSVT.

According to the regression analysis results above, we see that a reduced LVEF might partly account for the occurrence of NSVT. A pathophysiological explanation of such a relationship between LVEF and NSVT is provided as follows. It has been known, from cardiovascular physiology, that intense stimulations of baroreceptors can result in an increase in efferent cardiac vagal activity and a decrease in sympathetic activity. Since the impaired left ventricular function, measured by a reduced LVEF value, would result in a decreased change in arterial blood pressure, such a blunt change in arterial blood pressure thus could not effectively elicit stimulations to the baroreceptors so that efferent cardiac vagal activity might decrease to and maintain a lower level. Thus, this reduced vagal tone would then elicit an enhancement of sympathetic tone. Consequently, sympathovagal balance state LF/HF might increase by an accelerative rate to an abnormally higher level. This accelerative sympathetic predominance, which would yield a larger α , might increase the probability of electrical instability in cardiac conduction system and therefore, such a conductive abnormality finally precipitated NSVT. An illustration of the potential pathophysiological mechanism between LVEF and NSVT described above is also given in Fig. 5.4.

It should be noted that the independent variable LVEF in the linear regressive model given by Eq. 5.12 only accounted for about 43% of the variation in α . This might imply that, in addition to LVEF there might exist some other clinical parameters, reflecting unknown pathophysiological mechanisms, which could also contribute

to the variation in α or the precipitation of NSVT so that the linear regression equation could be further modified as

$$\alpha_i = c_0 + c_1 \cdot \text{LVEF}_i + c_2 \cdot \text{other clinical parameters} + e_i. \quad (5.13)$$

Therefore, we may speculate that the left ventricular dysfunction, reflected by a reduced LVEF, might not serve as the only factor in the occurrence of NSVT although it did have certain important pathophysiological relationship with the NSVT. This can be also revealed by the fact that almost all ischemic patients have a reduced LVEF but do not always end in NSVT.

5.2 An Examination of Long-Term HRV Behavior

Previous studies have pointed out that a decrease in HRV is an independent long-term statistical predictor of overall and sudden arrhythmic mortality after *myocardial infarction* (MI) [6, 24, 59]. The prevailing hypothesis is that because HRV is dependent on intact neurocardiac autonomic regulation, a decrease in HRV may reflect the autonomic dysfunction associated with cardiac electrical instability. Adrenergic hyperactivity and/or lack of presumably protective parasympathetic autonomic tone are the purported pathophysiological mechanisms of such lethal arrhythmogenesis [85, 99]. Since the NSVT patients included in this study were all ischemia-related CAD, we may speculate that a decrease long-term HRV should be seen in both the ischemic and the ischemia-related NSVT episodes in our database.

The long-term HRV was computed for all the 153 RR signals in our database. It was actually quantified by the ratio of LF to HF power over the entire RR signal. Still, the power or energy calculations were performed using the WT coefficients. We computed the FWT for each RR signal in the uniformly-resampled form. According

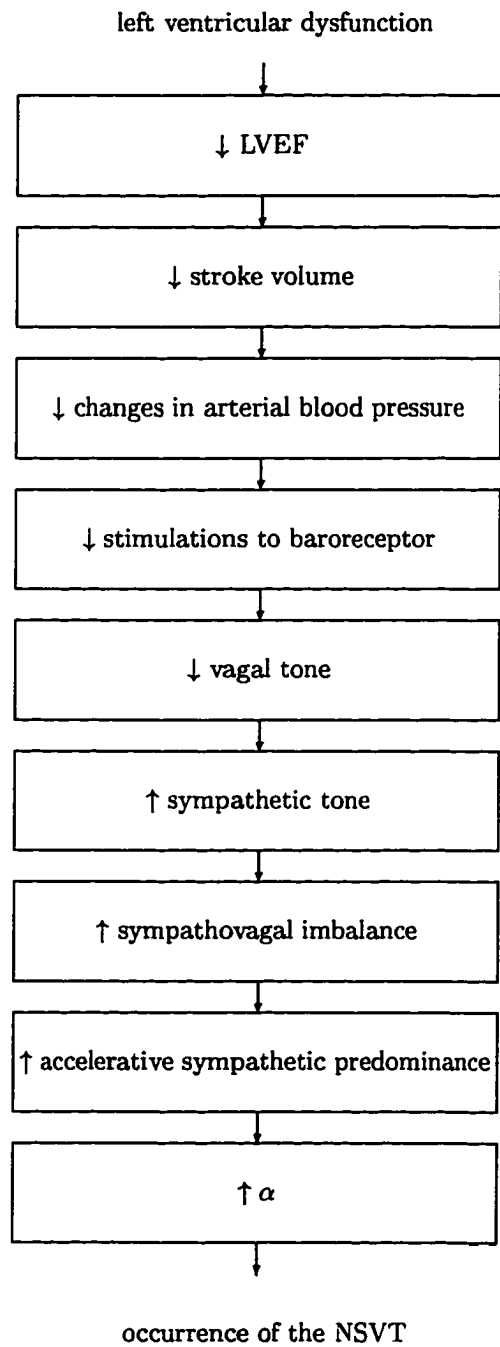


Figure 5.4: An illustration of the potential mechanism between left ventricular dysfunction and occurrence of the NSVT.

to the descriptions in Section 4.3.1, we know that the FWT computation can be only applied to a signal with the length of 2's power, to get the WT coefficients for almost all of the entire signal we here adopted a shift-and-computation procedure, which is very similar to the one described in Section 4.3.2 and depicted in 4.5, that could overcome this length limitation problem so that the WT coefficients of an RR signal might be successfully found.

The mathematical expression for long-term sympathovagal balance quantification is briefly described as follows. First, Let N_j represent the total number of WT coefficients at level 2^j for an RR signal and recall that a composite detail RR signal in real time at level 2^j , denoted $D_j(t)$, is defined by Eq. 3.5. The sympathovagal balance state over the period T_{RR} of the entire RR signal can be then expressed as

$$\begin{aligned}
r_{sv} &= \frac{\frac{1}{T_{RR}} \sum_{j=LF} \|D_j(t)\|^2}{\frac{1}{T_{RR}} \sum_{j=HF} \|D_j(t)\|^2} \\
&= \frac{\frac{1}{T_{RR}} \sum_{j=LF} \sum_{k=0}^{N_j-1} d_j^2(k) \|\psi_{j,k}(t)\|^2}{\frac{1}{T_{RR}} \sum_{j=HF} \sum_{k=0}^{N_j-1} d_j^2(k) \|\psi_{j,k}(t)\|^2} \\
&= \frac{\sum_{j=LF} \sum_{k=0}^{N_j-1} d_j^2(k)}{\sum_{j=HF} \sum_{k=0}^{N_j-1} d_j^2(k)}. \tag{5.14}
\end{aligned}$$

r_{sv} thus provides an insight into autonomic balance status over the entire RR signal. Note that in this study, T_{RR} was generally ranged from 8 to 20 minutes. Choosing 0.03125–0.0625 Hz as LF and 0.125–0.5 Hz as HF, Eq. 5.14 is then changed into the expression as

$$r_{sv} = \frac{\sum_{j=-5} \sum_{k=0}^{N_j-1} d_j^2(k)}{\sum_{j=-2,-3} \sum_{k=0}^{N_j-1} d_j^2(k)}. \tag{5.15}$$

Using Eq. 5.15 we computed the long-term sympathovagal balance state for the RR signal corresponding to each of the 153 episodes in our database. Consequently, we obtained r_{sv} 's for all these episodes. First, the distributions, represented by means and

type	long-term LF/HF r_{sv} (mean \pm standard deviation)
NSVT	2.2253 \pm 2.4670
Ischemic	2.7564 \pm 2.1448
Normal	0.4922 \pm 0.4324

Table 5.2: Distributions of long-term sympathovagal balance r_{sv} for the NSVT, ischemic and normal.

standard deviations, of the populations NSVT, ischemia and normal were calculated. A listing of the numerical results is in Table 5.2. Observing Table 5.2, we see that while the long-term ABS values of the population normal distributed in a smaller scale, those of both the populations ischemia and the ischemia-related NSVT generally spread in a much larger scale. In addition, we also noticed that no clear differences appeared between the long-term LF/HF power ratio distributions of the ischemic and the NSVT. Such an observation, however, did suggest that an increased long-term sympathovagal balance might indicate the propensity to the occurrence of ischemia-related NSVT, consistent to the findings suggested by previous studies [75, 99].

Further, to achieve the optimal threshold-based classification performance, we computed the ROC again. In this application, we lumped the ischemic and the NSVT as a high-risk group. Defining the *specificity* and *sensitivity* as the percentages of the correctly classified normal and high-risk episodes, respectively, we then obtained the optimal classification results as shown in Table 5.3. From Table 5.3 we found that the long-term HRV was able to provide a very accurate risk predictor because while it attained 80% of specificity (*i.e.*, only 1 out of 5 normal episodes was misclassified as false ischemic/NSVT), approximate 82% of sensitivity (*i.e.*, only 27 out of 148 high-risk episodes were misclassified as false normal).

overall accuracy (%)	specificity (%)	sensitivity (%)	false ischemic/NSVT	false normal
81.6993	80.0000	81.7568	1.0000	27.0000

Table 5.3: Optimal classification results given by the threshold for long-term LF/HF ranged from 0.387 to 0.414.

Additionally, it should be noted that the FFT-based long-term LF/HF measure has been “overwhelmingly” adopted by many HRV works. Therefore, we here also provided a simple performance evaluation for the results obtained from FFT spectral analysis in the following. Denoting the FFT-based long-term sympathovagal balance state as $r_{sv}^{(FFT)}$, we have

$$r_{sv}^{(FFT)} \sim 2.0263 \pm 2.3215 \text{ for the NSVT;}$$

$$r_{sv}^{(FFT)} \sim 3.0772 \pm 2.6264 \text{ for the ischemic;}$$

$$r_{sv}^{(FFT)} \sim 0.3989 \pm 0.2638 \text{ for the normal;}$$

$$\text{sensitivity} \approx 77\%; \quad \text{specificity} = 80\%.$$

Obviously, the FFT-based long-term LF/HF measure achieved *similar but a bit worse* classification results than did the WT-based measure for the pattern recognition task above. That is, while 1 out of 5 normal episodes was misclassified as false high-risk, there were 34 out of 148 high-risk episodes misclassified as false normal. Similarly, there were no clear differences between the distributions of $r_{sv}^{(FFT)}$ for the ischemic and the NSVT. We thus concluded that the long-term measures of HRV (either WT- or FFT-based) might only indicate the propensity of ventricular tachyarrhythmias. Unlike the long-term measures, however, according to the analysis results obtained from this dissertation research (mostly described in Chapter 4) we found that the

short-term HRV measure could provide a more detailed information for the precipitation of NSVT. We may speculate, in fact, that the long-term HRV somehow seemed to “swamp out” the subtle features or information revealed by the short-term HRV.

CHAPTER 6

CONCLUSION

6.1 A Summary of this Research Work

Many retrospective studies have now conclusively demonstrated that HRV may be a useful tool to understand physiological regulatory mechanisms. In addition, clinically HRV may serve as a risk predictor for post-infarction mortality, SCD and arrhythmic events, since it may provide a better understanding of the dynamic changes of autonomic balance status, a key for the mechanisms underlying pathological events. In this dissertation, a novel multiresolution power estimation technique based on the WT has been introduced for the assessment of HRV before the onset of NSVT, with the goal of prediction of the occurrence of NSVT. Such a nonstationary signal processing technique can not only optimize the trade-off effects between time and frequency resolutions but also preserve the nonstationarity associated with the signal of interest, far better than traditional STFT methods.

Previous studies have pointed out that a decrease in HRV is an independent long-term statistical predictor of overall and sudden arrhythmic mortality after *myocardial infarction* (MI) [6, 24, 59]. The prevailing hypothesis is that because HRV is dependent on intact neurocardiac autonomic regulation, a decrease in HRV may reflect

the autonomic dysfunction associated with cardiac electrical instability. Adrenergic hyperactivity and/or lack of presumably protective parasympathetic autonomic tone are the purported pathophysiological mechanisms of such lethal arrhythmogenesis [85, 99]. However, while decreased HRV may represent a long-term predictor of adverse outcome, it remained unclear whether or not, in fact, the same holds true with regard to short-term prediction. In other words, the ability of HRV measures to identify a single patient who will in fact suffer ventricular arrhythmia and sudden death has not been demonstrated, and more importantly, none of the HRV measures has consistently been shown to forecast the exact time of sudden death.

Knowing that the WT analysis method worked very well in short-term HRV analysis according to the numerical results obtained from a method validation trial, we investigated the prediction of NSVT by employing WT coefficients to estimate the so-called sympathovagal balance status, reflected by the power ratio LF/HF, first and then assessing this WT-based HRV measure immediately before the onset of NSVT. Demonstrations were conducted on a database consisting of 153 episodes. The numerical results based on the statistical distributions of a morphological information marker α indicated that:

1. there were no significant change in HRV observed for both ischemic and healthy episodes, and
2. NSVT episodes seemed to be associated with abrupt spikes in the autonomic balance evolution in the several minutes before the onset of NSVT.

In conclusion, we acknowledge that both the long-term and short-term HRV measures might have different prediction abilities for the NSVT. The former could serve

as a predictor of the propensity to NSVT although it is unable to precisely predict its occurrence. Fig. 6.1 provides an illustration of this prediction capability. Unlike the long-term measures, the short-term HRV observations seemed to be able to more effectively detect the “exact” occurrence of NSVT several minutes before it happens (8–20 minutes according to our results). This perhaps reflects that the instantaneous autonomic balance information, which could be swamped out in the long-term measure, might be of prognostic value in understanding the onset of NSVT. Similarly, an illustration of the short-term HRV based pattern recognition procedure is given in Fig. 6.2. The performance evaluation of this study did suggest that an altered autonomic activity to the heart may serve as an important factor in the initiation of idiopathic NSVT, regardless of the mechanisms underlying these arrhythmias.

6.2 Potential Limitations

It should be noted that there were frequent VPBs as well as repetitive NSVT episodes during 24-hour recordings in almost all of the patients in this study. Actually, frequent VPBs themselves may result in a significant impact on HRV or sympathovagal balance computation. Therefore, this study was potentially limited by the methodological difficulties in computation of HRV during the presence of VPBs. As described in Chapter 4, in this study an NSVT episode was *excluded* if there was *any* VPB observed within, at most, 512 seconds (≈ 8.53 minutes) immediately before the onset of NSVT. Also, patients with frequent NSVT or VT throughout the whole 24-hour recordings were excluded if there was no clean RR signal (“clean” was defined as an RR recording without any VPBs) that had lasted, at least, 512 seconds without VPBs. Both selection criteria were set in order to avoid the technical

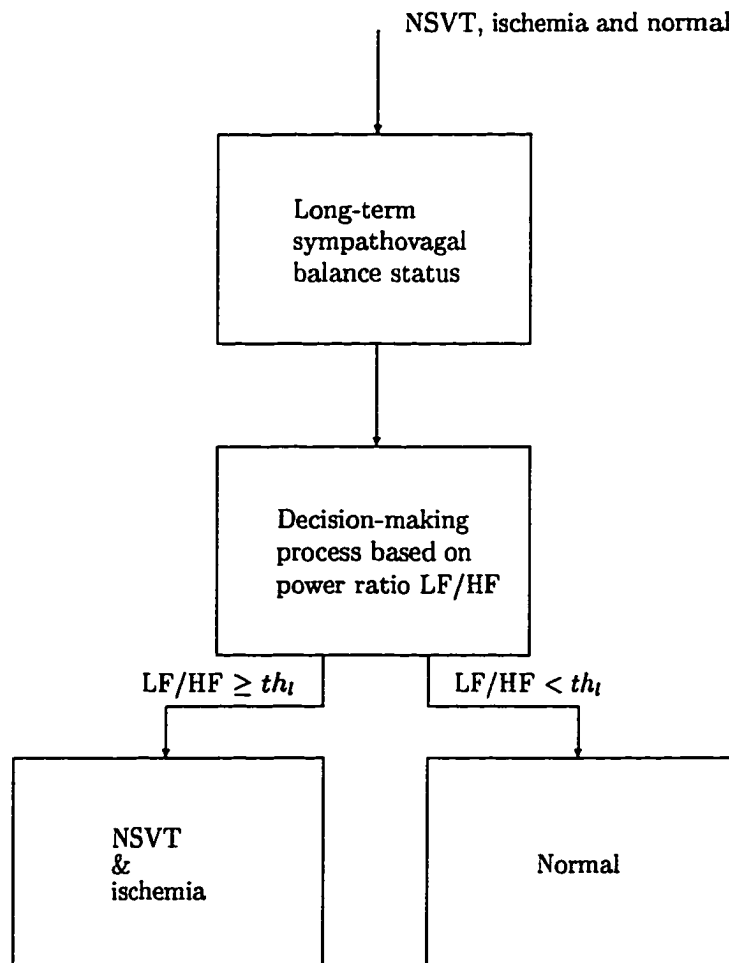


Figure 6.1: The application of long-term HRV assessment for prediction of the propensity to NSVT. Note that th_l represents a pre-determined threshold for long-term sympathovagal balance status.

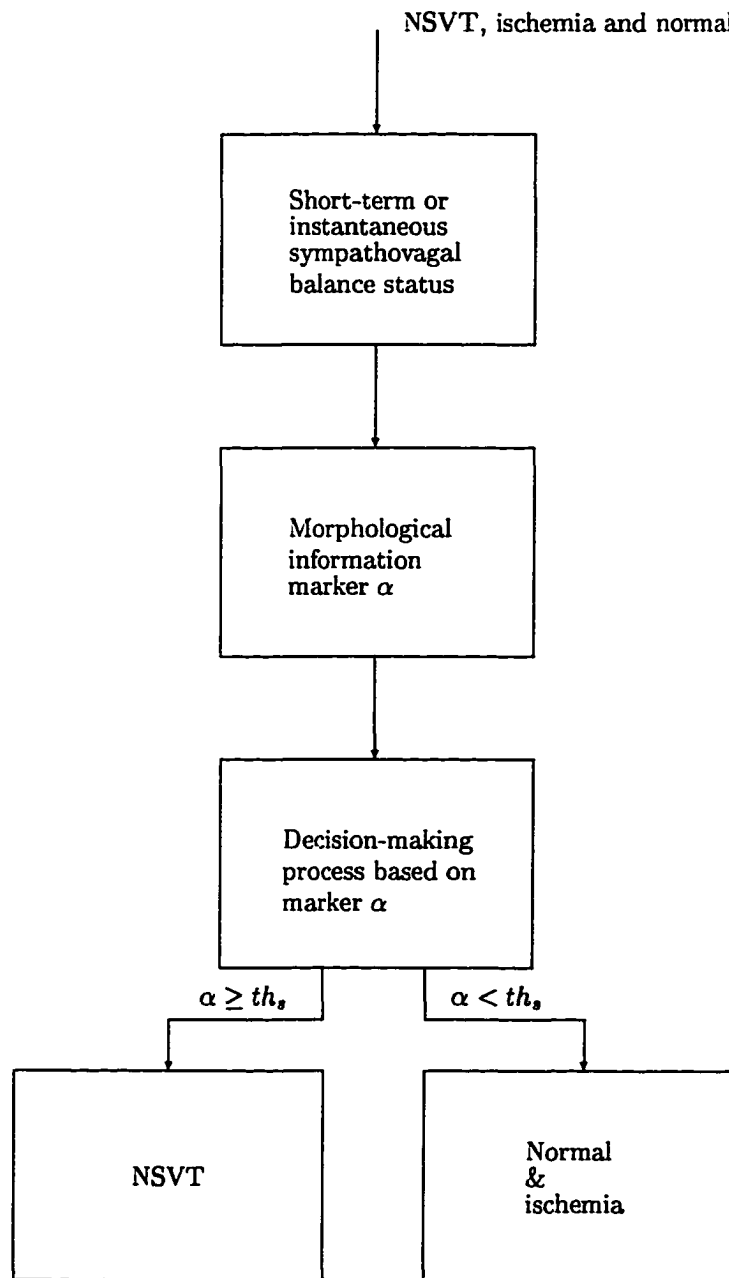


Figure 6.2: The application of the short-term HRV assessment for prediction of the exact occurrence of NSVT. Note that th_s represents a pre-determined threshold for morphological information marker α derived from short-term sympathovagal balance evolution.

difficulties involved in compensating for the impacts of VPBs on HRV values. As a result, the selection criteria allowed only a limited number of RR recordings suitable for analysis. However, this could simultaneously guarantee that a more accurate HRV assessment might be attained because no impact from VPBs was involved in HRV measures revealed by these selected RR recordings.

Although the selection criteria adopted in this study only allowed us to include those RR recordings that had no VPBs to guarantee a better evaluation accuracy, occasionally RR recordings with isolated VPBs, in fact, need not be excluded. In general, abnormal beats, particular those that do not originate in the SA node such as VPBs, are excluded from the calculations of many statistics (*e.g.*, the standard deviation of HR) simply by excluding the intervals in which an abnormal beat participates. For other forms of analysis, however, it is appropriate to *interpolate* through such intervals. That is, those interval samples that have been influenced by the VPBs are removed and replaced with a *linear interpolation* or *median filtering* between the surrounding NN (*i.e.*, normal-to-normal) samples. This is true in improving the estimation qualities such as the power spectrum of HR that can be dominated by VPBs if they are not excluded.

6.3 An Extension for Future Explorations

6.3.1 NSVT Risk Stratification

Note that in addition to serving as a risk factor required to be predicted in advance, NSVT itself is also known as a risk predictor. NSVT was shown to significantly influence both sudden and nonsudden cardiac mortality in several studies [7, 53, 60]. The treatment of such patients, however, remains a major challenge in part because

of the lack of an effective strategy for identifying high-risk patients who would have been benefited the most from treatment. EPS testing has been shown to play the most important role in the risk stratification and management of patients with *sustained monomorphic VT* (SMVT) and cardiac arrest [80, 94]. However, the role of EPS testing in the management of NSVT patients remains controversial. Some studies concluded that EPS is useful in identifying patients with NSVT and organic heart disease who are at high (*i.e.*, inducible SMVT) and low (*i.e.*, no inducible SMVT) risk for future arrhythmic events and also, the EPS-directed therapy improved the outcome [12, 62, 103, 108]. However, in a study by Wilber *et al.* [106] of 100 patients with asymptomatic NSVT, CAD and LVEF < 40%, these investigators concluded that while therapeutic intervention to prevent SCD is unnecessary in patients without inducible SMVT, EPS-directed drug therapy of inducible SMVT patients might have limited efficacy. Their results indicated that only 50% of the inducible SMVT patients were drug responders and the rest 50% nonresponders remained at high risk for subsequent SCD. Fig. 6.3 summarizes their findings. Therefore, the limitation of EPS testing as the only strategy for risk stratification, particularly for high-risk patients, could result in severe consequences.

Since NSVT do not pose the same/uniform risk for the cardiac patients, the prognosis of NSVT varies somehow depending on the type of heart disease. Simple and reliable noninvasive tests are needed for better stratification of high-risk patients. Now that we have figured out, in this dissertation, the approaches to the prediction of NSVT by adopting HRV or autonomic balance status, it is possible to appeal to the further applications of these clinical measures in serving as a prognostically useful information on the risk stratification task for NSVT. That is, collecting the medical

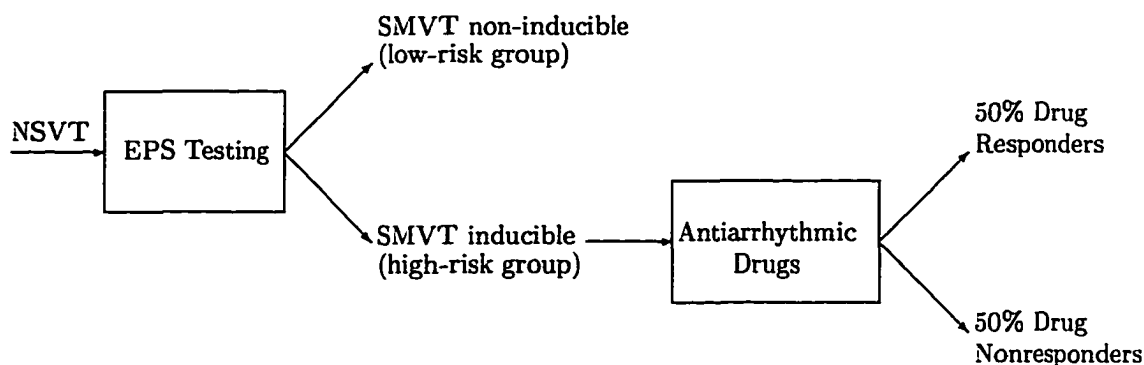


Figure 6.3: The limitation of EPS-guided therapy as the sole strategy for managing the inducible SMVT (high risk) patients. According to the results suggested by Wilber *et al.*, treatment for prevention of SCD is unnecessary in patients without inducible SMVT, whereas only approximate 50% of the inducible SMVT patients were drug responders and nonresponders remained at high risk for subsequent SCD.

records for NSVT patients, we may then seek for an HRV-based risk stratification scheme, towards a devise of more effective treatment strategy and drug therapy. Such a scheme may be developed simply by conducting an outcome analysis. Therefore, we may speculate that, in addition to EPS testing, this HRV-directed testing procedure may be also served as an alternative used to stratify the risk for NSVT patients. Furthermore, the potential HRV-directed testing may be also combined with some clinical parameters such as LVEF, late potentials, complexity of VPBs and other existing tests listed in Table 1.2 in stratifying the risk for NSVT patients. Actually, a more complete and accurate risk stratification and its associated treatment strategy in NSVT may be then attained based on a combination use of these risk predictors. In addition, it is important to note that drug therapy and efficacy should not only focus on suppression of VPBs or NSVT, but also on suppression of the potential NSVT precipitants such as the abnormality in cardiac ANS activity.

6.3.2 NSVT versus Nonischemic Heart Disease

In addition to CAD, NSVT is also very common in patients with *nonischemic heart diseases* (NHD), such as idiopathic dilated cardiomyopathy, hypertrophic cardiomyopathy, hypertensive heart disease and mitral valve prolapse [37, 61, 77, 78, 79, 107]. Since the prognostic value of NSVT is *less* well established in NHD, either the risk stratification or the management is very difficult and even a greater challenge than in the setting of CAD.

In general, the incidence of NSVT is highest (up to 40%) in patients with *nonischemic dilated cardiomyopathy* (NDC) [48, 81, 101]. Unlike patients with CAD, the prognostic significance of NSVT for these patients with respect to SCD and mortality still remains unclear nowadays. Some researchers had adopted the programmed stimulation (*i.e.*, EPS testing) to predict the risk in NDC patients [102]. According to their results, these researchers concluded that normal findings on the EPS testing, such as non-inducible VT, did *not* imply a benign outcome. That is, SCD occurred with equal or even higher frequency in patients without inducible VT. Hence, the EPS testing did not appear to be very useful in this NDC patient population. It is also uncertain whether or not the EPS-guided therapy is beneficial to the same patient population. The complexity or frequency of VPBs, however, may predict a higher risk of sudden death in patients with NDC [79, 91]. Additionally, The severity of left ventricular dysfunction, reflected by parameter LVEF, may be also an important determinant of prognosis in patients with NDC [38].

It should be emphasized here that a much greater effort is still needed to increase our understanding of the significance of NSVT in NHD. So far HRV, in fact, has not been extensively studied in NHD/NDC process, therefore further studies are required

for determining the role of HRV or cardiac ANS activity in the risk stratification of the NHD patients with NSVT. We may seek for a clarification of this issue by assessing the short-term HRV prior to the occurrence of NSVT for this patient population and this would represent a reasonable extension of this dissertation study.

BIBLIOGRAPHY

- [1] M. Akay. Introduction: wavelet transforms in biomedical engineering. *Annals of Biomedical Engineering*, 23:529–530, 1995.
- [2] M. Akay. Wavelets in biomedical engineering. *Annals of Biomedical Engineering*, 23:531–542, 1995.
- [3] S. Akselrod. Spectral analysis of fluctuation in cardiovascular parameters: a quantitative tool for the investigations of autonomic control. *Trends Pharmacological Society*, 9:6–10, 1988.
- [4] S. Akselrod, D. Gordon, F. A. Ubel, and *et al.* Power spectrum analysis of heart rate fluctuations: a quantitative probe of beat-to-beat cardiovascular control. *Science Wash. DC*, 213:220–222, 1981.
- [5] D. Alexopoulos, S. Yusuf, J. A. Johnston, and *et al.* The 24-hour heart rate behavior in long-term survivors of cardiac transplantation. *Am. J. Cardiol.*, 61:880–884, 1988.
- [6] A. Algra, J. G. P. Tijssen, J. R. T. C. Roelandt, and *et al.* Heart rate variability from 24-hour electrocardiography and the 2-year risk for sudden death. *Circulation*, 88:180–185, 1993.
- [7] K. P. Anderson, J. DeCamilla, and A. J. Moss. Clinical significance of ventricular tachycardia (3 beats or longer) detected during ambulatory monitoring after myocardial infarction. *Circulation*, 57:890–897, 1978.
- [8] A. Angelone and N. A. Coulter. Respiratory sinus arrhythmia: a frequency dependent phenomenon. *J. Applied Physiol.*, 19:479–482, 1964.
- [9] M. L. Appel, R. D. Berger, J. P. Saul, and *et al.* Beat-to-beat variability in cardiovascular variables: noise or music? *J. Am. Coll. Cardiol.*, 14:1139–1148, 1989.
- [10] R. M. Berne and M. N. Levy (Editors). *Physiology*. Mosby-Year Book, Inc., St. Louis, MI, 1993.

- [11] G. Breithardt, M. Borggrefe, and A. Podczeck. Electrophysiology and pharmacology of asymptomatic nonsustained ventricular tachycardia. *Clinical Progress in Electrophysiology and Pacing*, 4(2):81–99, 1986.
- [12] A. E. Buxton, F. E. Marchlinski, B. T. Flores, and *et al.* Nonsustained ventricular tachycardia in patients with coronary artery disease: role of electrophysiologic study. *Circulation*, 75:1178–1185, 1987.
- [13] R. E. Challis and R. I. Kitney. Biomedical signal processing (in four parts): part 2– the frequency transforms and their inter-relationships. *Medical & Biological Engineering & Computing*, 29:1–17, January 1991.
- [14] S.-W. Chen and P. M. Clarkson. Identification of cardiac arrhythmias using a damped exponential predominant frequency algorithm. In *IEEE Proceedings of the 17th Annual International Conference of the Engineering in Medicine and Biology Society (EMBS 95)*, pages 181–182, Montreal, Canada, September 1995.
- [15] S.-W. Chen and P. M. Clarkson. Prony residual analysis for the identification of cardiac arrhythmias. In *IEEE Proceedings of the 1995 International Conference on Acoustics, Speech, and Signal Processing (ICASSP 95)*, volume 2, pages 1177–1180, Detroit, MI, May 1995.
- [16] S.-W. Chen and P. M. Clarkson. Detection of cardiac arrhythmias using a damped exponential modeling algorithm. In *IEEE Proceedings of the 1996 International Conference on Acoustics, Speech, and Signal Processing (ICASSP 96)*, volume 3, pages 1776–1779, Atlanta, GA, May 1996.
- [17] S.-W. Chen, P. M. Clarkson, and Q. Fan. A sequential technique for cardiac arrhythmia discrimination. In *Proceedings of International Society for Computerized Electrocardiology (ISCE)*, page tba, Orlando, FL, April 1995.
- [18] S.-W. Chen, P. M. Clarkson, and Q. Fan. A robust sequential detection algorithm for cardiac arrhythmia classification. *IEEE Transactions on Biomedical Engineering*, 43(11):1120–1125, 1996.
- [19] S.-W. Chen, B. D. Jaffe, S. D. Nelson, and *et al.* Prony residual as ventricular tachycardia marker. *Circulation*, 88(4):I644, 1993.
- [20] P. M. Clarkson, S.-W. Chen, and Q. Fan. A robust sequential detection algorithm for cardiac arrhythmia classification. In *IEEE Proceedings of the 1995 International Conference on Acoustics, Speech, and Signal Processing (ICASSP 95)*, volume 2, pages 1181–1184, Detroit, MI, May 1995.

- [21] P. M. Clarkson and H. Stark (Editors). *Signal Processing Methods for Audio, Images and Telecommunications*. Academic Press, San Diego, CA 92101, 1995.
- [22] P. Coumel. Heart rate variability and the onset of tachyarrhythmias. *Giornale Italiano di Cardiologia*, 22(5):647–654, 1992.
- [23] M. J. Cowan, K. Pike, and R. L. Burr. Effects of gender and age on heart rate variability in healthy individuals and in persons after sudden cardiac arrest. *Journal of Electrocardiology*, 27:1–9, supplement 1994.
- [24] T. R. Cripps, M. Malik, T. G. Farrell, and *et al.* Prognostic value of reduced heart rate variability after myocardial infarction: clinical evaluation of a new analysis method. *Br. Heart J.*, 64:14–19, 1991.
- [25] I. Daubechies. Orthonormal bases of compactly supported wavelets. *Commun. in Pure and Applied Math.*, 41:909–996, 1988.
- [26] I. Daubechies. The wavelet transform, time-frequency localization and signal analysis. *IEEE Trans. Inform. Theory*, 36:961–1005, 1990.
- [27] I. Daubechies. Ten lectures on wavelets. In *CBMS-NSF Series in Applied Math.*, SIAM, page no. 61, Philadelphia, 1992.
- [28] I. Daubechies. Orthonormal bases of compactly supported wavelets ii. variations on a theme. *SIAM J. Math. Anal.*, 24:499–519, 1993.
- [29] C. T. M. Davies and J. M. M. Neilson. Sinus arrhythmia in man at rest. *J. Applied Physiol.*, 22:947–955, 1967.
- [30] G. M. DeFerrari and P. J. Schwartz. Autonomic nervous systems and arrhythmias. *Ann. NY Acad. Sci.*, 601:247–262, 1990.
- [31] M. H. DeGroot. *Probability and Statistics*. Addison-Wesley, Reading, MA, 1986.
- [32] D. L. Eckberg. Human sinus arrhythmia as an index of vagal cardiac outflow. *J. Applied Physiol.*, 54:961–966, 1983.
- [33] D. L. Eckberg and P. Sleight. *Human Baroreflexes in Health and Disease*. Oxford University Press, Oxford, England, 1992.
- [34] D. J. Ewing, I. W. Campbell, and B. F. Clarke. Assessment of cardiovascular effects in diabetic autonomic neuropathy and prognostic implications. *Ann. Intern. Med.*, 92:308–311, 1980.

- [35] T. G. Farrell, Y. Bashir, T. Cripps, and *et al.* Risk stratification for arrhythmic events in post-infarction patients based on heart rate variability, ambulatory electrocardiographic variables and the signal-averaged electrocardiogram. *J. Am. Coll. Cardiol.*, 18:687–697, 1991.
- [36] L. Fei, D. J. Statters, K. Hnatkova, and *et al.* Change of autonomic influence on the heart immediately before the onset of spontaneous idiopathic ventricular tachycardia. *American College of Cardiology*, 24(6):1515–1522, 1994.
- [37] G. S. Francis. Development of arrhythmias in the patient with congestive heart failure: pathophysiology, prevalence and prognosis. *Am. J. Cardiol.*, 57(suppl. B):3B–7B, 1986.
- [38] J. K. Gillman, S. Jalal, and G. V. Naccarelli. Predicting and preventing sudden death from cardiac causes. *Circulation*, 90(2):1083–1092, 1994.
- [39] A. Grossman and J. Morlet. Decomposition of Hardy functions into square integrable wavelets of constant shape. *SIAM J. Math. Anal.*, 15:723–736, 1984.
- [40] P. Grossman. Respiratory and cardiac rhythms as windows to central and autonomic biobehavioral regulation: selection of window frames, keeping the panes clean and viewing the neural topography. *Biological Psychology*, 34:131–161, 1992.
- [41] P. Grossman, J. Karemaker, and W. Wieling. Prediction of tonic cardiac control using respiratory sinus arrhythmia: the need for respiratory control. *Psychophysiology*, 28:201–216, 1991.
- [42] H. L. Van Trees. *Detection, Estimation, and Modulation Theory*. John Wiley & Sons, New York, NY, 1968.
- [43] R. Hainsworth. Reflexes from the heart. *Physio. Rev.*, 71:617–658, 1991.
- [44] R. Hainsworth and A. L. Mark. *Cardiovascular Reflex Control in Health and Disease*. Saunders, London, England, 1993.
- [45] S. C. Hammill, J. M. Trusty, D. L. Wood, and *et al.* Influence of ventricular function and presence or absence of coronary artery disease on results of electrophysiologic testing for asymptomatic nonsustained ventricular tachycardia. *Am. J. Cardiol.*, 65:722–728, 1990.
- [46] L. E. Hinkle and H. T. Thaler. Clinical classification of cardiac deaths. *Circulation*, 65:457–464, 1981.
- [47] J. A. Hirsch and B. Bishop. Respiratory sinus arrhythmia in humans: how breathing pattern modulates heart rate. *Am. J. Physiol.*, 241:H620–H629, 1981.

- [48] S. K. Huang, J. V. Messer, and P. Denes. Significance of ventricular tachycardia in idiopathic dilated cardiomyopathy: observation in 35 patients. *The American Journal of Cardiology*, 54:147–152, 1984.
- [49] H. V. Huikuri, J. O. Valkama, K. E. Airaksinen, and *et al.* Frequency domain measures of heart rate variability before the onset of non-sustained and sustained ventricular tachycardia in patients with coronary artery disease. *Circulation*, 87:1220–1228, 1993.
- [50] J. T. Bigger Jr., J. L. Fleiss, R. E. Kleiger, and *et al.* The relationships among ventricular arrhythmias, left ventricular dysfunction and mortality in the 2 years after myocardial infarction. *Circulation*, 69:250–258, 1984.
- [51] J. T. Bigger Jr., J. L. Fleiss, R. C. Steinman, and *et al.* Correlations among time and frequency domain measures of heart period variability two weeks after acute myocardial infarction. *The American Journal of Cardiology*, 69:891–898, April 1992.
- [52] J. T. Bigger Jr., J. L. Fleiss, R. C. Steinman, and *et al.* Frequency domain measures of heart period variability and mortality after myocardial infarction. *Circulation*, 85(1):164–171, 1992.
- [53] J. T. Bigger Jr., F. M. Weld, and L. M. Rolnitzky. Prevalence, characteristics and significance of ventricular tachycardia (3 or more complexes) detected with ambulatory electrocardiographic recording in the late hospital phase of acute myocardial infarction. *Am. J. Cardiol.*, 48:815–823, 1981.
- [54] B. D. Jaffe, S.-W. Chen, S. D. Nelson, and *et al.* Prony frequency analysis of prolonged qrs signal-averaged electrocardiograms. *Circulation Research*, 41(3):659A, 1993.
- [55] R. A. Johnson and D. W. Wichern. *Applied Multivariate Statistical Analysis*. Prentice-Hall, Englewood Cliffs, NJ, 1992.
- [56] D. T. Kaplan and M. Talajic. Dynamics of heart rate. *American Institute of Physics, Chaos*, 1(3):251–256, 1991.
- [57] S. M. Kay. *Modern Spectral Estimation: Theory & Application*. Prentice-Hall, Englewood Cliffs, NJ, 1988.
- [58] R. I. Kitney, S. Byrne, M. E. Edwards, and *et al.* Heart rate variability in the assessment of autonomic diabetic neuropathy. *Automedica*, 4:155–167, 1982.
- [59] R. E. Kleiger, J. P. Miller, J. T. Bigger Jr., and *et al.* Decreased heart rate variability and its association with increased mortality after acute myocardial infarction. *Am. J. Cardiol.*, 59:256–262, 1987.

- [60] R. E. Kleiger, J. P. Miller, S. Thanavaro, and *et al.* Relationship between clinical features of acute myocardial infarction and ventricular runs 2 weeks to 1 year after infarction. *Circulation*, 63:64–70, 1981.
- [61] R. C. Klein. Ventricular arrhythmias in aortic valve disease: analysis of 102 patients. *Am. J. Cardiol.*, 53:1079–1083, 1984.
- [62] R. C. Klein and C. Machell. Use of electrophysiologic testing in patients with nonsustained ventricular tachycardia: prognostic and therapeutic implications. *American College of Cardiology*, 14(1):155–161, 1989.
- [63] M. Kobayashi and T. Musha. $1/f$ fluctuation of heartbeat period. *IEEE Transaction on Biomedical Engineering*, 29(6):456–457, 1982.
- [64] D. L. Kuchar, C. W. Thorburn, and N. L. Sammel. Prediction of serious arrhythmic events after myocardial infarction: signal-averaged electrocardiogram, holter monitoring and radionuclide ventriculography. *J. Am. Coll. Cardiol.*, 9:531–538, 1987.
- [65] M. N. Levy and P. J. Schwartz (Editors). *Vagal Control of the Heart: Experimental Basis and Clinical Implications*. Futura Publishing Company, Inc., Armonk, NY, 1994.
- [66] M. Lishner, S. Akselrod, V. M. Avi, and *et al.* Spectral analysis of heart rate fluctuations. a noninvasive, sensitive method for the early diagnosis of autonomic neuropathy in diabetes mellitus. *J. Auton. Nerv. Syst.*, 19:119–125, 1987.
- [67] F. Lombardi, G. Sandrone, S. Pernpruner, and *et al.* Heart rate variability as an index of sympathovagal interaction after acute myocardial infarction. *The American Journal of Cardiology*, 60:1239–1245, December 1987.
- [68] L. T. Mainardi, A. M. Bianchi, G. Baselli, and *et al.* Pole-tracking algorithms for the extraction of time-variant heart rate variability spectral parameters. *IEEE Transaction on Biomedical Engineering*, 42(3):250–259, 1995.
- [69] M. Malik and A. J. Camm. *Heart Rate Variability*. Futura Publishing Company, Inc., Armonk, NY, 1995.
- [70] S. Mallat. Multifrequency channel decompositions of images and wavelet models. *IEEE Trans. Acoust. Speech Signal Process.*, 37:2091–2110, 1989.
- [71] S. Mallat. Multiresolution approximations and wavelet orthonormal bases of $L^2(\mathbf{R})$. *Trans. Amer. Math. Soc.*, 315:69–87, 1989.

- [72] S. Mallat. A theory for multiresolution signal decomposition: The wavelet representation. *IEEE Trans. Patt. Anal. Mach. Intell.*, 11:674–693, 1989.
- [73] A. Malliani, F. Lombardi, M. Pagani, and *et al.* Power spectral analysis of heart rate variability: a tool to explore neural regulatory mechanisms. *Br. Heart J.*, 71:1–2, 1994.
- [74] A. Malliani, M. Pagani, F. Lombardi, and *et al.* Cardiovascular neural regulation explored in the frequency domain. *Circulation*, 84:482–492, 1991.
- [75] A. Malliani, P. J. Schwartz, and A. Zanchetti. A neural mechanisms in life-threatening arrhythmias. *Am. Heart J.*, 100:705–715, 1980.
- [76] G. Mancia, A. Ferrari, L. Gregorini, and *et al.* Blood pressure and heart rate variabilities in normotensive and hypertensive human beings. *Circ. Res.*, 53:96–104, 1983.
- [77] B. J. Maron, D. D. Savage, J. K. Wolfson, and *et al.* Prognostic significance of 24 hour ambulatory monitoring in patients with hypertrophic cardiomyopathy: a prospective study. *Am. J. Cardiol.*, 48:252–257, 1981.
- [78] J. M. McLenachan and H. J. Dargie. Ventricular arrhythmias in hypertensive left ventricular hypertrophy. *Am. J. Hypertens.*, 3:735–740, 1990.
- [79] T. Meinertz, N. Treese, W. Kasper, and *et al.* Determinants of prognosis in idiopathic dilated cardiomyopathy as determined by programmed stimulation. *The American Journal of Cardiology*, pages 337–341, 1985.
- [80] L. B. Mitchell, H. J. Duff, D. E. Manyari, and *et al.* A randomized clinical trial of the noninvasive and invasive approaches to drug therapy of ventricular tachycardia. *N. Engl. J. Med.*, 317:1681–1687, 1987.
- [81] R. L. Mitra and A. E. Buxton. The clinical significance of nonsustained ventricular tachycardia. *Journal of Cardiovascular Electrophysiology*, 4(4):490–496, 1993.
- [82] A. J. Moss, H. T. Davis, J. Decamilla, and *et al.* Ventricular ectopic beats and their relation to sudden and nonsudden cardiac death after myocardial infarction. *Circulation*, 60:998–1003, 1979.
- [83] G. A. Myers, G. J. Martin, N. M. Magid, and *et al.* Power spectral analysis of heart rate variability in sudden cardiac death: comparison to other methods. *IEEE Transactions on Biomedical Engineering*, 33(12):1149–1165, 1986.
- [84] A. V. Oppenheim and R. W. Schaffer. *Digital Signal Processing*. Prentice-Hall, Eaglewood Cliffs, NJ, 1989.

- [85] M. Pagani, F. Lombardi, S. Guzzetti, and *et al.* Power spectral analysis of heart rate and arterial pressure variabilities as a marker of sympatho-vagal interaction in man and conscious dog. *Circulation Research*, 59:178–193, 1986.
- [86] R. Pedretti, M. D. Etro, A. Laporta, and *et al.* Prediction of late arrhythmic events after acute myocardial infarction from combined use of noninvasive prognostic variables and inducibility of sustained monomorphic ventricular tachycardia. *Am. J. Cardiol.*, 71:1131–1141, 1993.
- [87] P. B. Persson and H. R. Kirchheim. *Baroreceptor Reflexes*. Springer-Verlag, Berlin, Germany, 1991.
- [88] L. A. Pires and S. K. S. Huang. Nonsustained ventricular tachycardia: identification and management of high-risk patients. *American Heart Journal*, 126:189–200, July 1993.
- [89] M. Raczowska, D. L. Eckberg, and T. J. Ebert. Muscarinic cholinergic receptors modulate vagal cardiac response in man. *Journal of the Autonomic Nervous System*, 7:271–278, 1983.
- [90] J. O. Rawlings. *Applied Regression Analysis: A Research Tool*. Wadsworth & Brooks/Cole, Pacific Grove, CA, 1988.
- [91] F. Romeo, F. Pelliccia, F. Cianfrocca, and *et al.* Predictors of sudden death in idiopathic dilated cardiomyopathy. *The American Journal of Cardiology*, 63:138–140, 1989.
- [92] O. Rompelman, A. J. R. M. Coenen, and R. I. Kitney. Measurement of heart-rate variability: part 1– comparative study of heart-rate variability analysis methods. *Medical & Biological Engineering & Computing*, pages 233–239, May 1977.
- [93] W. Ruberman, E. Weinblatt, J. D. Goldberg, and *et al.* Ventricular premature beats and mortality after myocardial infarction. *N. Engl. J. Med.*, 297:750–757, 1977.
- [94] J. N. Ruskin, J. P. DiMarco, and H. Garan. Out-of-hospital cardiac arrest: electrophysiologic observations and selection of long-term antiarrhythmic therapy. *N. Engl. J. Med.*, 303:607–613, 1980.
- [95] K. E. F. Sands, M. L. Appel, L. S. Lilly, and *et al.* Power spectrum analysis of heart rate variability in human cardiac transplant recipients. *Circulation*, 79:76–82, 1989.
- [96] J. P. Saul. Beat-to-beat variations of heart rate reflect modulation of cardiac autonomic outflow. *NIPS*, 5:32–37, February 1990.

- [97] J. P. Saul. Heart rate variability during congestive heart failure: observations and implications. *Blood Pressure and Heart Rate Variability*, pages 266–275, 1992.
- [98] J. P. Saul, Y. Arai, R. D. Berger, and *et al.* Assessment of autonomic regulation in chronic congestive heart failure by heart rate spectral analysis. *Am. J. Cardiol.*, 61:1292–1299, 1988.
- [99] P. J. Schwartz, M. T. La Rovere, and E. Vanoli. Autonomic nervous system and sudden cardiac death. experimental basis and clinical observations for post-myocardial infarction risk stratification. *Circulation*, 85:77–91, 1992.
- [100] A. M. Sulpizi, T. D. Frierling, and P. R. Kowey. Value of electrophysiologic testing in patients with nonsustained ventricular tachycardia. *Am. J. Cardiol.*, 59:841–845, 1987.
- [101] A. Suyama, T. Anan, H. Araki, and *et al.* Prevalence of ventricular tachycardia in patients with different underlying heart disease: a study by holter ecg monitoring. *American Heart Journal*, 112:44–51, 1986.
- [102] G. Turitto, R. K. Ahuja, E. B. Caref, and *et al.* Risk stratification for arrhythmic events in patients with nonischemic dilated cardiomyopathy and nonsustained ventricular tachycardia: role of programmed ventricular stimulation and the signal-averaged electrocardiogram. *American College of Cardiology*, 24(6):1523–1528, 1994.
- [103] G. Turitto, J. M. Fontaine, S. Ursell, and *et al.* Risk stratification and management of patients with organic heart disease and nonsustained ventricular tachycardia: role of programmed stimulation, left ventricular ejection fraction and signal-averaged electrocardiogram. *Am. J. Med.*, 88(suppl. N):35N–41N, 1990.
- [104] E. P. Veltri, E. V. Platia, L. S. Griffith, and *et al.* Programmed electrical stimulation and long-term follow-up in asymptomatic nonsustained ventricular tachycardia. *Am. J. Cardiol.*, 56:309–314, 1985.
- [105] T. Vybiral, D. H. Glaeser, A. L. Goldberger, and *et al.* Conventional heart rate variability analysis of ambulatory electrocardiographic recordings fails to predict imminent ventricular fibrillation. *J. Am. Coll. Cardiol.*, 22:557–565, 1993.
- [106] D. J. Wilber, B. Olshansky, J. F. Moran, and *et al.* Electrophysiological testing and nonsustained ventricular tachycardia: use and limitations in patients with coronary artery disease and impaired ventricular function. *Circulation*, 82(2):350–358, 1990.

- [107] R. A. Winkle, M. G. Lopes, J. W. Fitzgerald, and *et al.* Arrhythmias in patients with mitral valve prolapse. *Circulation*, 52:73-81, 1975.
- [108] T. A. Zheutlin, H. Roth, W. Chua, and *et al.* Programmed electrical stimulation to determine the need for antiarrhythmic therapy in patients with complex ventricular ectopy. *Am. Heart. J.*, 111:860-867, 1986.
- [109] I. H. Zucker and J. P. Gilmore. *Control of the Circulation*. CRC Press, Boca Raton, Fla., 1991.